

# Shadows at the Galactic Center and at M87\* as a tool to test gravity theories

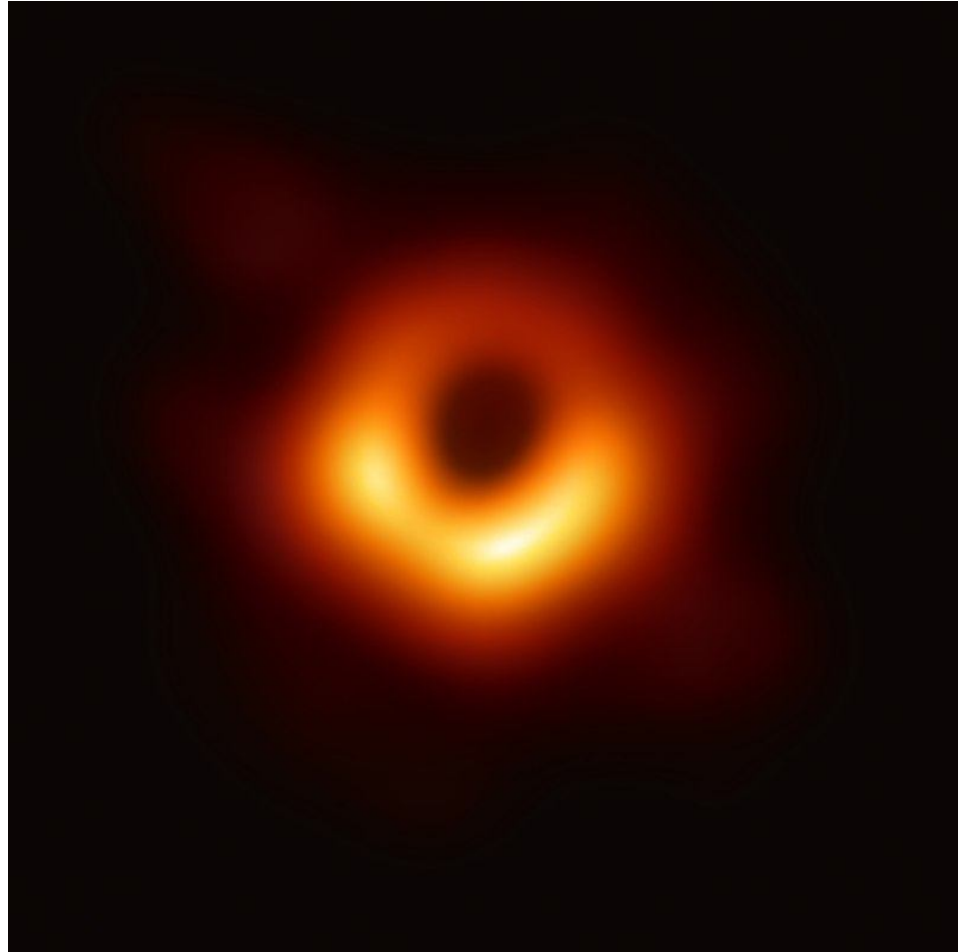
**А.Ф. Захаров (Alexander F. Zakharov)**

**E-mail: zakharov@itep.ru**

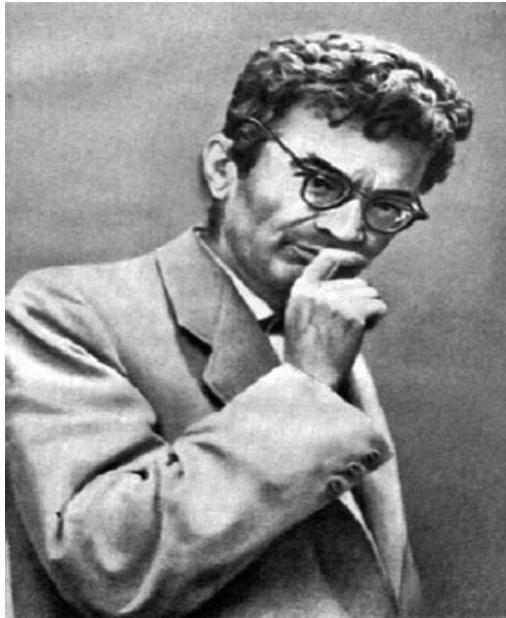
*Institute of Theoretical and Experimental Physics,  
B. Cheremushkinskaya, 25, 117218 Moscow*

*Bogoliubov Laboratory of Theoretical Physics  
Joint Institute for Nuclear Research, Dubna, Russia*

08.06.2021 Quarks online Workshops-2021  
Quantum Gravity and Cosmology  
(dedicated to A.D. Sakharov's centennial)



This conference is devoted to A.D. Sakharov's scientific heritage. When people discuss thermonuclear fusion they often remind Sakharov – Tamm idea (the tokamak idea) for controlled thermonuclear fusion reactor. I think it is very nice practice to remember the names of giants when we stand on their shoulders (if we use and rephrase a famous Newton's sentence). Now there are many public discussions about a benefits from fundamental research. Synchrotron radiation give us a nice example since such a radiation actively uses for technological applications and it is a source of radiation near supermassive BH's. Therefore, this phenomenon is extremely important for both fundamental science and technology.



I. Pomeranchuk, The maximum energy that primary cosmic ray electrons can have on the Earth's surface due to radiation in the Earth's magnetic field, *J. Phys. USSR*, 2, 356 (1940)

D. Ivanenko and I. Pomeranchuk, On the Maximal Energy Attainable in a Betatron, *Phys. Rev.* 65, 343 (1944)

L.A. Artsimovich and I. Pomeranchuk, The maximum energy that primary cosmic ray electrons can have on the Earth's surface due to radiation in the Earth's magnetic field, *J. Phys. USSR*, 2, 267 (1945)

Elder, F. R., Gurewitsch, A. M., Langmuir, R. V., & Pollock, H. C. Radiation from Electrons in a Synchrotron. *Physical Review*, 71(11), 829 (1947)

In 1950 D. Ivanenko, A. A. Sokolov and I. Pomeranchuk were awarded the State (Stalin) prize of the second grade for works on synchrotron radiation, presented in book "Classical Field Theory"

Synchrotron radiation plays a key role in many astrophysical objects (including BH's)



## Early VLBI in the USSR

L.L. Matveenko\*

Space Research Institute RAN, Profsojuznaja 84/32, 117997 Moscow, Russia

Received 2007 Mar 21, accepted 2007 Mar 21

Published online 2007 May 15

**Key words** history and philosophy of astronomy – instrumentation: detectors – techniques: interferometric – techniques: high angular resolution – telescopes

This article gives story of interferometer with independent elements (Very Long Baseline Interferometer) in Russia. At the end of February 1962 the author discussed with G.Ya. Gus'kov, DSN Station, Evpatorija a new type of radio interferometer and proposed an experiment between two DSN stations. In September 1962 he reported the new method and proposed a VLBI experiment at seminar of Radio Astronomical Laboratory, Pushino, and then at a seminar of Astronomical Institute GAISH which recommended to take out a Patent. In December GAISH sent documents to the Patent Bureau. In summer 1963 the author discussed with B. Lovell in Evpatorija the VLBI method of and we signed memorandum an Ev-JB experiment at  $\lambda = 32$  cm. In December 1963 the Patent Bureau permitted publication, and the paper was sent to Radiofizika. Really VLBI in the USSR began with the proposal of M. Cohen and K. Kellermann, February 1968, to do an experiment between 22-m antenna Pushino and 43-m Green Bank.

© 2007 WILEY-VCH Verlag GmbH & Co. KGaA, Weinheim

### 1 Introduction

Progress of technologies in the middle of the last century gave us atomic frequency standards, low-noise receivers, broad-band tape recorders, computers, and large antennas making possible modern radio astronomy. It was the epoch of great astronomical discoveries – synchrotron emission of radio sources, radio recombination lines, maser emission, quasars, pulsars, and planets. This was also the beginning of a new cosmic era, with direct studies of planets by space probes. For management of space flight it was necessary to have measurements with very high angular accuracy. For studies of the structure of compact radio sources it was necessary to have instrument with very high angular resolution too. Radio wavelengths are many thousands times larger than optical ones, so the size of radio telescopes would have to be very big. Radio astronomers proposed interferometer method, where angular resolution is determined by distance between antennas. Nobel laureate M. Ryle applied interferometer methods for studies of the structure of radio sources. The baseline size has technical limitations. The proposed method of “independent” interferometer removed the problems. The angular resolution of VLBI is thousands of times higher than that of optical telescopes and studies of the star-forming regions and AGN objects became possible. VLBI opened a new page of astronomy. If the Galileo's telescope opened the solar system, then VLBI opened all the surrounding cosmos. Radio astronomers of different countries and continents were joined and created a global VLBI network. This paper describes how this has happened.

\* Corresponding author: matveen@iki.rssi.ru

### 2 Deep Space Network, Evpatorija

The history of VLBI is closely connected with space exploration. At the end of the 1950s first space vehicles (Lunniks) were launched. Radio astronomers of the Lebedev Institute constructed a radio interferometer near Simeiz in Crimea and measured trajectories of the space probes and point at which the package hit the Moon (Vitkevich et al. 1961). The results of measurements were highly praised by chief rocket designer S.P. Korolev. This technique enabled the detection of trajectories of the plasma flows leaving the Sun. The velocities of movements were higher than the escape velocity of the Sun and after several days the high-energy particles reached Earth causing a noise storm. Soon after the launch of the Lunniks the construction of the deep-space tracking station was started near Evpatorija, Crimea. The main instrument was an interferometer with 500-m baseline formed by two ADU-1000 antennas. Each of these antennas was composed of eight 16-m parabolic dishes, mounted on a naval gun turret (Fig. 1). The antennas were equipped with low-noise parametric preamplifiers at  $\lambda = 32$  cm and masers at  $\lambda = 8$  cm (Matveenko et al. 1965). The Lebedev Institute collaborated in the construction of the interferometer. The angular accuracy was to be 0.1 arcsec, a very high accuracy for that time. Bright compact reference radio sources were needed to calibrate the radio interferometer. We invited G. Khromov and G. Sholomitskii, aspirants of I.S. Shklovskii at GAISH, to select the reference radio sources.

ika, Armenia, with a mixer receiver but the accuracy was insufficient. We measured parameters of the real system with parametric preamplifier, parameters of which were very critical for antenna adjusting. We knew from our measurements near Simeiz that during spring and autumn humidity is high and water vapor condenses in the cables. The same was expected to happen in antenna waveguides, increasing absorption. During the disconnecting of waveguides we discussed coordinate data, obtained by the method of the long baseline Doppler measurements. The frequencies of received signals were decreased by mixing with signals of atomic frequency standards (ammonia type) at each antenna, and written on a magnetic tape recorder, with a bandwidth of 100 kHz. Then the differential Doppler frequency of the signals was determined by computer. But the same principle could be applied to an interferometer to measure the differential phase of the signals. The coherence of intermediate frequency signals could be checked by pilot signals written on the tape from the same atomic standard. In this case the elements of the interferometer need not be physically connected and distances between antennas were not limited. The Earth size does not impose a limit, since an antenna can be placed in orbit. This interferometer had no problems with compensation of relative time delay. The tapes containing signals could be read later. We had only one problem – the narrow bandwidth of the tape recorder, which limited the sensitivity of the measurements. But big progress in recorder technology very soon overcome this problem. The Guskov Institute was actively developing a broadband tape recorder with rotating heads and the Basov laboratory developed hydrogen frequency standards. Gus'kov proposed for the beginning to use the DSN stations Evpatorija (ADU-1000) and Simferopol', Crimea (32 m antenna), which had the necessary equipment.

In autumn 1962 I had been in Pushino at a seminar of the Radio Astronomy Laboratory (Head V.V. Vitkevich) and reported about the proposal of the new type of radio interferometer with independent elements and suggested an experiment Evpatorija-Simferopol'; it was not supported. The opinion was: "It is impossible, because it is never possible"!? V.V. Vitkevich excused that the Laboratory cannot support publishing the paper or carrying out an experiment. I had only one possibility – my GAISH colleagues. After a few days the GAISH seminar, Director D.Ja. Martinov, recommended to take out a patent. This solution was a little strange for me – experimental methods should be accessible to all. In December 1962 GAISH sent to the Patent Bureau the VLBI proposal of L.I. Matveenko, N.S. Kardashev, and G.B. Sholomitskii.

In summer 1963 B. Lovell (Director of Jodrell Bank Radio Observatory) was a guest of M.V. Keldysh and visited the Evpatorija DSN station. The DSN director asked me to meet Prof. B. Lovell and explain the technical and scientific directions of DSN, including antennas, transmitter, atomic standards, low-noise receivers, and radio astronomical studies. To obtain more interest we invited I.S. Shklovskii and to

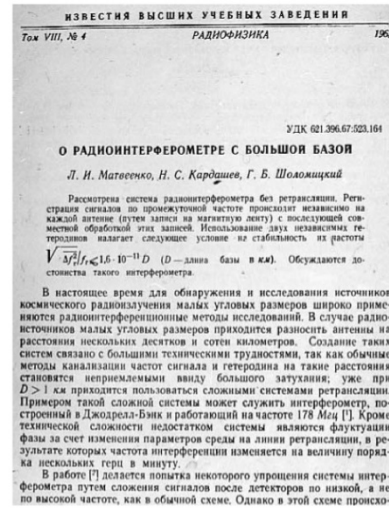


Fig. 4 The first VLBI publication in Radiofizika Vol. 4, p. 651, 1965.

translate we asked G.S. Khromov. They had been in Crimea Observatory for a summer school. I.S. Shklovskii proposed that I report about the VLBI method. However, I had to wait for the opinion of the Patent Bureau. B. Lovell agreed with the VLBI idea, but doubted the necessity of the very large resolution. Cas A or Tau A are the strongest radio sources because they have big angular size, but their brightness temperature is not very high  $T_b \sim 10^7$  K. The radio emission of stars is weak because they have much smaller brightness temperature. I.S. Shklovskii remarked: "Maybe we do not know compact objects because we have no instruments to measure them". B. Lovell and I prepared a Memorandum concerning interferometer between Evpatorija and Jodrell Bank at  $\lambda = 32$  cm. Jodrell Bank had equipment for collaboration on the Moon program. B. Lovell proposed to discuss details at Jodrell Bank and inform DSN and FIAN, but we did not receive an answer.

In the December 1963 the Patent Bureau agreed with the publication of the VLBI method and the paper was sent to the journal Radiofizika. After a long discussion with the referee, the dependence of interference fringes on the stability of the local oscillator was included and the paper published in 1965 (Fig. 4).

## 5 Proposal of M.H. Cohen and K.I. Kellermann

The first VLBI experiment was carried out in 1967 by two independent teams in the USA and in Canada. After finish-



- The BlackHoleCam team (supported by the European Research Council): “When forced to summarize the general theory of relativity in one sentence: Time and space and gravitation have no separate existence from matter.” Albert Einstein
- The Event Horizon Telescope (supported by NSF): “Seeing the unseeable.” Sheperd S. Doeleman
-

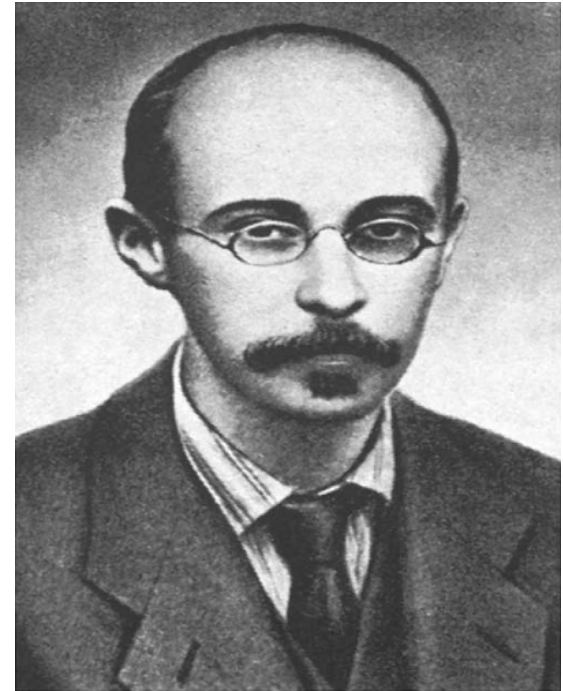
# Outline of my talk

- Introduction
- Shadows for Kerr as a tool to evaluate BH characteristics
- Shadows around Reissner-Nordstrom BHs
- The first image of shadow at M87\*
- Dependence of shadow size on charge
- Conclusions

# References

- AFZ, F. De Paolis, G. Ingrosso, and A. A. Nucita, *New Astronomy* 10 (2005) 479.
- AFZ, F. De Paolis, G. Ingrosso, and A. A. Nucita, *Astronomy & Astrophys.* 442, 795 (2005).
- AFZ, F. De Paolis, G. Ingrosso, and A. A. Nucita, *New Astronomy Reviews*, **56**, 64 (2012).
- AFZ, *Physical Reviews D* **90**, 062007 (2014).

# D. Hilbert, V. Frederiks, A. Friedmann



G. Gamov (Friedmann's student), V.A. Fock  
(Frederiks's & Friedmann's student)



## The Jablonna conference on gravitation: a continuing source of inspiration

Marek Demianski

Received: 21 January 2014 / Accepted: 11 March 2014 / Published online: 23 May 2014  
© The Author(s) 2014. This article is published with open access at Springerlink.com

First of all I would like to welcome all of you at the main campus of the University of Warsaw—my University. Especially warmly I would like to welcome the youngest participants who for the first time participate in a big international conference. I do understand how you feel, I do understand your anxiety. Fifty one years ago I was able to observe the International Jablonna Conference on General Relativity and Gravitation, that later was classified as the GRG-3 conference. In June of 1962, I got my Master of Science degree in physics. My thesis advisor, Professor Leopold Infeld, was the Chairman of the Local Organizing Committee of the Jablonna conference. Professor Infeld asked me to help with such simple tasks as cleaning the blackboard, make sure that chalk was always available, but also—and this was really important—every morning to collect participants who were staying in hotels in Warsaw into a special coach and bring them in time to Jablonna, and in the evening bring them back to Warsaw. So that is how I ended up listening to all lectures and discussions and more. Now looking back from the perspective of half a century I think that the Jablonna Conference was the most important scientific conference that I attended so far.

The opening session of the Jablonna conference was held at the Staszica Palace in Warsaw, a short walk from where we are now. It is an easy recognizable building, in front of it is the famous monument of Copernicus (Fig. 1). The first talk was delivered by Professor J. L. Synge on “Relativistic interpretation and modification of Newtonian models”. On Fig. 2 is Professor J. Synge delivering his talk and, in the first row (from the left) Professors L. Infeld, V. Fock, J. Anderson, T. Newman, R. Penrose and B. Hoffman, and on the far right Dr. Róża Michalska-Trautman. After the first talk,

---

This article belongs to the Topical Collection: The First Century of General Relativity: GR20/Amaldi10.

M. Demianski (✉)  
Institute of Theoretical Physics, Hoza 69, 00-681 Warsaw, Poland  
e-mail: marek.demianski@fuw.edu.pl



**Fig. 1** The Staszica Palace in Warsaw

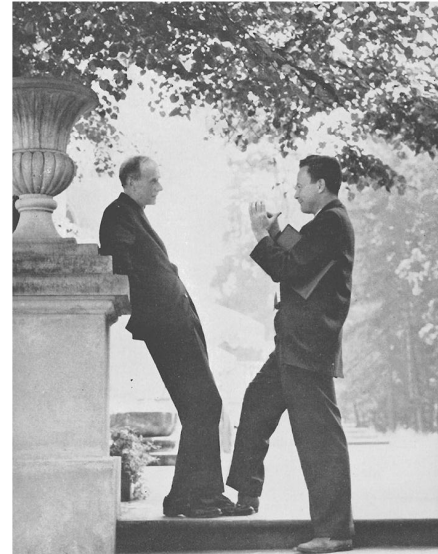


**Fig. 2** Professor J. Synge delivering the opening lecture

followed by a short discussion, the session was adjourned and all participants were transferred to Jablonna.

Jablonna is a small town about 20 km from Warsaw. In XVIII century a famous Polish aristocratic family of Poniatowski built there a summer palace and two adjacent buildings with several rooms for their guests and servants. The Palace was surrounded

**Fig. 6** Paul Dirac and Richard Feynman at Jablonna



the 2nd World War such a large group of physicists from the West and the East were able to meet. There were continuous discussions, usually in small groups between scientists coming from the West and the East. Also Germans from the DDR and the Bundes Republik were able to meet for the first time since the construction of the Berlin wall. It was a conference attended by many outstanding scientists. All leading physicists working at that time on general relativity and gravitation were present in Jablonna, including P. A. M. Dirac, R. Feynman, J. A. Wheeler, P. G. Bergmann, H. Bondi, S. Chandrasekhar, B. DeWitt, V. Ginzburg, D. Ivanenko, A. Lichnerowicz, C. Moller, L. Rosenfeld and J. Weber among others. One can say that Jablonna was a nesting place of Nobel Prize winners—Paul Dirac, Richard Feynman, Subrahmanyan Chandrasekhar, Vitali Ginzburg and also Peter Higgs were there. The main topics of discussions in Jablonna concentrated on general properties of gravitational radiation, quantization of gravity and exact solutions of the Einstein field equations. Only one talk given by Vitali Ginzburg was devoted to observational tests of general relativity (Figs. 6, 7, 8).

The most memorable lecture, in a dynamic showman style, was delivered by Richard Feynman. He presented his program of quantizing general relativity modeled on his very successful approach to quantum electrodynamics. Of course, he used Feynman diagrams. I am sure that Abhay Ashtekar will tell you more about it. After the conference I have listened to Feynman's talk many times trying to transcribe it from tapes. Fortunately John Stachel stayed in Warsaw for several months after the conference

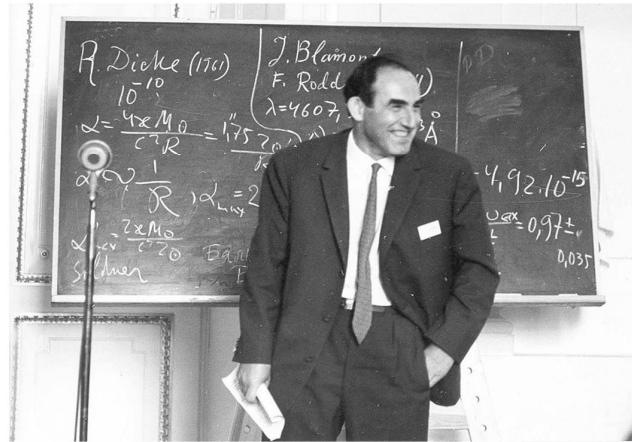


**Fig. 7** Vitali Ginzburg delivering his lecture at the Jablonna conference

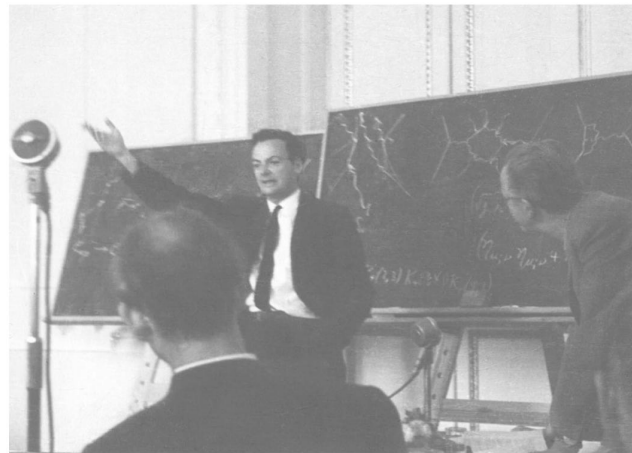


**Fig. 8** Richard Feynman delivering his lecture at the Jablonna conference

“Incidentally, to give you some idea of the difference in order to calculate this diagram Fig. 4b the Young-Mills case took me about a day; to calculate the diagram in the case of gravitation I tried again and again and was never able to do it; and it was finally put on a computing machine—I don’t mean the arithmetic, I mean the algebra of all the terms coming in, just the algebra; I did the integrals myself later, but the algebra of the thing was done on a machine by John Matthews so I couldn’t done it by hand. In fact, I think it’s historically interesting that it’s the first problem in algebra that I know of that was done on a machine that has not been done by hand.” Just for

- Home**
- News**
- Features**
- Columns & blogs**
- Archive
- Specials**
- In focus**
- X chromosome
- Future computing
- Stem cells
- Bird flu
- Mars
- GM crops

**Stories by subject**

**NEWS CHANNELS**

- My news**
- Biotechnology**
- Careers**
- Drug discovery**
- Earth and environment**
- Medical Research**
- Physical Sciences**

- [Feedback](#)
- [About this site](#)
- [About us](#)
- [For librarians](#)

**TOP STORIES**

- [Air pollution influences crop disease](#)  
04 April 2005
- [Hunters win hike in polar bear quota](#)  
04 April 2005
- [Genetic patch treats 'bubble-boy' disease](#)  
03 April 2005
- [Transgenic cows have](#)

## NEWS

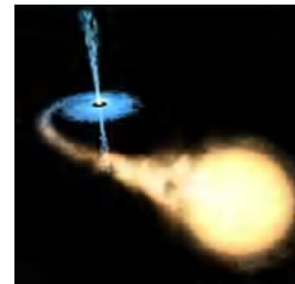
Published online: 31 March 2005; | doi:10.1038/news050328-8

### Black holes 'do not exist'

[Philip Ball](#)

#### These mysterious objects are dark-energy stars, physicist claims.

Black holes are staples of science fiction and many think astronomers have observed them indirectly. But according to a physicist at the Lawrence Livermore National Laboratory in California, these awesome breaches in space-time do not and indeed cannot exist.



Black holes, such as the one pictured in this artist's impression, may in fact be pockets of 'dark energy'.

© ESA/NASA

Over the past few years, observations of the motions of galaxies have shown that some 70% the Universe seems to be composed of a strange 'dark energy' that is driving the Universe's accelerating expansion.

George Chapline thinks that the collapse of the massive stars, which was long believed to generate black holes, actually leads to the formation of stars that contain dark energy. "It's a near certainty that black holes don't exist," he claims.

Black holes are one of the most celebrated predictions of Einstein's general theory of relativity, which explains gravity as the warping of space-time caused by massive objects. The theory suggests that

# Black Holes or Gray Stars? That's the Question: Pseudo-Complex General Relativity

Peter O. Hess, W. Greiner, T. Schöenbach and G. Caspar

**Abstract** After a short review on attempts to extend General Relativity, pseudo-complex variables are introduced. We restate the main properties of these variables. The variational principle has to be modified in order to obtain a new theory. An additional contribution appears, whose origin is a repulsive, dark energy. The general formalism is presented. As examples, the Schwarzschild and the Kerr solutions are discussed. It is shown that a collapsing mass increasingly accumulates dark energy until the collapse is stopped. Rather than a black hole, a gray star is formed. We discuss a possible experimental verification, investigating the orbital frequency of a particle in a circular orbit.

## 1 Introduction

General Relativity (GR) is a well accepted theory which has been verified by many experimental measurements. One prediction of this theory is the existence of *black holes*, which are formed once a very large mass suffers a gravitational collapse. Astronomical observations seem to confirm this prediction, finding large mass concentrations in the center of most galaxies. These masses vary from several million solar masses to up to several billion solar masses. However, a black hole implies the appearance of an event horizon, below which an external observer cannot penetrate, thus, excluding a part of space from observation. A black hole also implies a singularity at its center. Both consequences from GR may be, from a philosophical point of view, unacceptable and one would like to find a possibility to avoid them. A black hole is an extreme object and one would not be surprised that GR has to be modified

---

Peter O. Hess (✉)  
Instituto de Ciencias Nucleares, UNAM, C.U., A.P. 70-543, 04510 México D.F., Mexico  
e-mail: hess@nucleares.unam.mx

W. Greiner, G. Caspar and T. Schöenbach  
FIAS, J. W.-Goethe University, Ruth-Moufang-Str. 1, 60438 Frankfurt am Main, Germany

ON A STATIONARY SYSTEM WITH SPHERICAL SYMMETRY  
CONSISTING OF MANY GRAVITATING MASSES

BY ALBERT EINSTEIN  
(Received May 10, 1939)

If one considers Schwarzschild's solution of the static gravitational field of spherical symmetry

$$(1) \quad ds^2 = -\left(1 + \frac{\mu}{2r}\right)^4 (dx_1^2 + dx_2^2 + dx_3^2) + \left(\frac{1 - \frac{\mu}{2r}}{1 + \frac{\mu}{2r}}\right)^2 dt^2$$

it is noted that

$$g_{44} = \left(\frac{1 - \frac{\mu}{2r}}{1 + \frac{\mu}{2r}}\right)^2$$

vanishes for  $r = \mu/2$ . This means that a clock kept at this place would go at the rate zero. Further it is easy to show that both light rays and material particles take an infinitely long time (measured in "coördinate time") in order to reach the point  $r = \mu/2$  when originating from a point  $r > \mu/2$ . In this sense the sphere  $r = \mu/2$  constitutes a place where the field is singular. ( $\mu$  represents the gravitating mass.)

There arises the question whether it is possible to build up a field containing such singularities with the help of actual gravitating masses, or whether such regions with vanishing  $g_{44}$  do not exist in cases which have physical reality. Schwarzschild himself investigated the gravitational field which is produced by an incompressible liquid. He found that in this case, too, there appears a region with vanishing  $g_{44}$  if only, with given density of the liquid, the radius of the field-producing sphere is chosen large enough.

This argument, however, is not convincing; the concept of an incompressible liquid is not compatible with relativity theory as elastic waves would have to travel with infinite velocity. It would be necessary, therefore, to introduce a compressible liquid whose equation of state excludes the possibility of sound signals with a speed in excess of the velocity of light. But the treatment of any such problem would be quite involved; besides, the choice of such an equation of state would be arbitrary within wide limits, and one could not be sure that thereby no assumptions have been made which contain physical impossibilities.

One is thus led to ask whether matter cannot be introduced in such a way that questionable assumptions are excluded from the very beginning. In fact this can be done by choosing, as the field-producing mass, a great number of

The following table gives  $\mu$  and  $2r_0$  for  $M = 1$  as functions of  $\sigma_0$  (approximately):

$\sigma_0$	$\mu$	$2r_0$
0.	1.	$\infty$
.05	.988	19.76
.1	.948	9.48
.15	.97	6.56
.2	1.13	5.65
.23	1.32	5.63
.25	1.82	7.40
.26	2.63	10.1
.268	$\infty$	$\infty$

When the cluster is contracted from an infinite diameter its mass decreases at the most about 5%. This minimal mass will be reached when the diameter  $2r_0$  is about 9. The diameter can be further reduced down to about 5.6, but only by adding enormous amounts of energy. It is not possible to compress the cluster any more while preserving the chosen mass distribution. A further addition of energy enlarges the diameter again. In this way the energy content, i.e. the gravitating mass of the cluster, can be increased arbitrarily without destroying the cluster. To each possible diameter there belong two clusters (when the number of particles is given) which differ with respect to the particle velocity.

Of course, these paradoxical results are not represented by anything in physical nature. Only that branch belonging to smaller  $\sigma_0$  values contains the cases bearing some resemblance to real stars, and this branch only for diameter values between  $\infty$  and  $9M$ .

The case of the cluster of the shell type, discussed earlier in this paper, behaves quite similarly to this one, despite the different mass distribution. The shell type cluster, however, does not contain a case with infinite  $\mu$ , given a finite  $M$ .

The essential result of this investigation is a clear understanding as to why the "Schwarzschild singularities" do not exist in physical reality. Although the theory given here treats only clusters whose particles move along circular paths it does not seem to be subject to reasonable doubt that more general cases will have analogous results. The "Schwarzschild singularity" does not appear for the reason that matter cannot be concentrated arbitrarily. And this is due to the fact that otherwise the constituting particles would reach the velocity of light.

This investigation arose out of discussions the author conducted with Professor H. P. Robertson and with Drs. V. Bargmann and P. Bergmann on the mathematical and physical significance of the Schwarzschild singularity. The problem quite naturally leads to the question, answered by this paper in the negative, as to whether physical models are capable of exhibiting such a singularity.

# Coevolution (Or Not) of Supermassive Black Holes and Host Galaxies

John Kormendy<sup>1</sup> and Luis C. Ho<sup>2</sup>

<sup>1</sup>Department of Astronomy, University of Texas at Austin,  
2515 Speedway C1400, Austin, TX 78712-1205; email: kormendy@astro.as.utexas.edu

<sup>2</sup>The Observatories of the Carnegie Institution for Science,  
813 Santa Barbara Street, Pasadena, CA 91101; email: lho@obs.carnegiescience.edu

## Abstract

Supermassive black holes (BHs) have been found in 87 galaxies by dynamical modeling of spatially resolved kinematics. The *Hubble Space Telescope* revolutionized BH research by advancing the subject from its proof-of-concept phase into quantitative studies of BH demographics. Most influential was the discovery of a tight correlation between BH mass  $M_{\bullet}$  and the velocity dispersion  $\sigma$  of the bulge component of the host galaxy. Together with similar correlations with bulge luminosity and mass, this led to the widespread belief that BHs and bulges coevolve by regulating each other's growth. Conclusions based on one set of correlations from  $M_{\bullet} \sim 10^{9.5} M_{\odot}$  in brightest cluster ellipticals to  $M_{\bullet} \sim 10^6 M_{\odot}$  in the smallest galaxies dominated BH work for more than a decade.

New results are now replacing this simple story with a richer and more plausible picture in which BHs correlate differently with different galaxy components. A reasonable aim is to use this progress to refine our understanding of BH - galaxy coevolution. BHs with masses of  $10^5 - 10^6 M_{\odot}$  are found in many bulgeless galaxies. Therefore, classical (elliptical-galaxy-like) bulges are not necessary for BH formation. On the other hand, while they live in galaxy disks, BHs do not correlate with galaxy disks. Also, any  $M_{\bullet}$  correlations with the properties of disk-grown pseudobulges and dark matter halos are weak enough to imply no close coevolution.

The above and other correlations of host galaxy parameters with each other and with  $M_{\bullet}$  suggest that there are four regimes of BH feedback. (1) Local, secular, episodic, and stochastic feeding of small BHs in largely bulgeless galaxies involves too little energy to result in coevolution. (2) Global feeding in major, wet galaxy mergers rapidly grows giant BHs in short-duration, quasar-like events whose energy feedback does affect galaxy evolution. The resulting hosts are classical bulges and coreless-rotating-disky ellipticals. (3) After these AGN phases and at the highest galaxy masses, maintenance-mode BH feedback into X-ray-emitting gas has the primarily negative effect of helping to keep baryons locked up in hot gas and thereby keeping galaxy formation from going to completion. This happens in giant, core-nonrotating-boxy ellipticals. Their properties, including their tight correlations between  $M_{\bullet}$  and core parameters, support the conclusion that core ellipticals form by dissipationless major mergers. They inherit coevolution effects from smaller progenitor galaxies. Also, (4) independent of any feedback physics, in BH growth modes (2) and (3), the averaging that results from successive mergers plays a major role in decreasing the scatter in  $M_{\bullet}$  correlations from the large values observed in bulgeless and pseudobulge galaxies to the small values observed in giant elliptical galaxies.

**Table 1** Mass measurements of supermassive black holes in our Galaxy, M31, and M32

Galaxy	$D$ (Mpc)	$\sigma_e$ (km s <sup>-1</sup> )	$M_\bullet$ ( $M_{\text{low}}, M_{\text{high}}$ ) ( $M_\odot$ )	$r_{\text{infl}}$ (arcsec)	$\sigma_*$ (arcsec)	$r_{\text{infl}}/\sigma_*$	Reference
(1)	(2)	(3)	(4)	(5)	(6)	(7)	(8)
Galaxy			4.41(3.98–4.84) e6		0.0146	2868.	Meyer et al. 2012
Galaxy			4.2 (3.9 – 4.6 ) e6		0.0139	3013.	Yelda et al. 2011
Galaxy	0.00828	105	4.30(3.94–4.66) e6	41.9	0.0146	2868.	Genzel, Eisenhauer & Gillessen 2010
Galaxy	0.00828	105	4.30(3.94–4.66) e6	41.9	0.0146	2868.	Gillessen et al. 2009a
Galaxy			4.09(3.74–4.43) e6		0.0148	2829.	Gillessen et al. 2009b
Galaxy			4.25(3.44–4.79) e6		0.0139	3013.	Ghez et al. 2008
Galaxy			3.80(3.60–4.00) e6		0.0056	7478.	Ghez et al. 2005
Galaxy			3.7 (3.3 – 4.1 ) e6		0.0075	5583.	Ghez et al. 2003
Galaxy			3.8 (2.3 – 5.4 ) e6		0.0155	2702.	Schödel et al. 2002
Galaxy			2.1 (1.3 – 2.8 ) e6		0.113	371.	Chakrabarty & Saha 2001
Galaxy			3.1 (2.6 – 3.6 ) e6		0.26	161.	Genzel et al. 2000
Galaxy			2.7 (2.5 – 2.9 ) e6		0.39	107.	Ghez et al. 1998
Galaxy			2.70(2.31–3.09) e6		0.39	107.	Genzel et al. 1997
Galaxy			2.55(2.12–2.95) e6		0.39	107.	Eckart & Genzel 1997
Galaxy			2.8 (2.5 – 3.1 ) e6		2.4	17.4	Genzel et al. 1996
Galaxy			2.0 (0.9 – 2.9 ) e6		4.9	8.5	Haller et al. 1996
Galaxy			2.9 (2.0 – 3.9 ) e6		3.4	12.3	Krabbe et al. 1995
Galaxy			2. e6		5	8.4	Evans & de Zeeuw 1994
Galaxy			3. e6		5	8.4	Kent 1992
Galaxy			5.4 (3.9 – 6.8 ) e6		15	2.8	Sellgren et al. 1990
M31	0.774	169	1.4 (1.1–2.3) e8	5.75	0.053	109.	Bender et al. 2005
M31			1.0 e8		0.297	19.4	Peiris & Tremaine 2003
M31			6.1 (3.6–8.7) e7		0.052	111.	Bacon et al. 2001
M31			3.3 (1.5–4.5) e7		0.297	19.4	Kormendy & Bender 1999
M31			6.0 (5.8–6.2) e7		0.297	19.4	Magorrian et al. 1998
M31			9.5 (7 – 10) e7		0.42	13.7	Emsellem & Combes 1997
M31			7.5 e7		0.56	10.3	Tremaine 1995
M31			8.0 e7		0.42	13.7	Bacon et al. 1994
M31			5 (4.5–5.6) e7		0.59	9.7	Richstone, Bower & Dressler 1990
M31			3.8 (1.1– 11) e7		0.56	10.3	Kormendy 1988a
M31			5.6 (3.4–7.8) e7		0.59	9.7	Dressler & Richstone 1988
M32	0.805	77	2.45(1.4–3.5) e6	0.46	0.052	8.76	van den Bosch & de Zeeuw 2010
M32			2.9 (2.7–3.1) e6		0.052	8.76	Verolme et al. 2002
M32			3.5 (2.3–4.6) e6		0.052	8.76	Joseph et al. 2001
M32			2.4 (2.2–2.6) e6		0.23	1.98	Magorrian et al. 1998
M32			3.9 (3.1–4.7) e6		0.050	9.11	van der Marel et al. 1998a
M32			3.9 (3.3–4.5) e6		0.050	9.11	van der Marel et al. 1997a, 1997b
M32			3.2 (2.6–3.7) e6		0.23	1.98	Bender, Kormendy & Dehnen 1996
M32			2.1 (1.8–2.3) e6		0.34	1.34	Dehnen 1995
M32			2.1 e6		0.34	1.34	Qian et al. 1995
M32			2.1 (1.7–2.4) e6		0.34	1.34	van der Marel et al. 1994a
M32			2.2 (0.8–3.5) e6		0.59	0.77	Richstone, Bower & Dressler 1990
M32			9.3 e6		0.59	0.77	Dressler & Richstone 1988
M32			7.5 (3.5–11.5) e6		0.76	0.60	Tonry 1987
M32			5.8 e6		1.49	0.31	Tonry 1984

Lines based on HST spectroscopy are in red. Column 2 is the assumed distance. Column 3 is the stellar velocity dispersion inside the “effective radius” that encompasses half of the light of the bulge. Column 4 is the measured BH mass with the one-sigma range that includes 68% of the probability in parentheses. Only the top four  $M_\bullet$  values for the Galaxy include distance uncertainties in the error bars. Column 5 is the radius of the sphere of influence of the BH; the line that lists  $r_{\text{infl}}$  contains the adopted  $M_\bullet$ . Column 6 is the effective resolution of the spectroscopy, estimated as in Kormendy (2004). It is a radius that measures the blurring effects of the telescope point-spread function or “PSF,” the slit width or aperture size, and the pixel size. The contribution of the telescope is estimated by the dispersion  $\sigma_{\text{tel}}$  of a Gaussian fitted to the core of the average radial brightness profile of the PSF. In particular, the HST PSF has  $\sigma_{\text{tel}} \approx 0.036$  from a single-Gaussian fit to the PSF model in van der Marel, de Zeeuw & Riv (1997a)

## Image of a Spherical Black Hole with Thin Accretion Disk

J.-P. Luminet

Groupe d'Astrophysique Relativiste, Observatoire de Paris, Section d'Astrophysique, F-92190-Meudon, France

Received July 13, 1978

**Summary.** Black hole accretion disks are currently a topic of widespread interest in astrophysics and are supposed to play an important role in a number of high-energy situations. The present paper contains an investigation of the optical appearance of a spherical black hole surrounded by thin accretion disk. Isoradial curves corresponding to photons emitted at constant radius from the hole as seen by a distant observer in arbitrary direction have been plotted, as well as spectral shifts arising from gravitational and Doppler shifts. By the results of Page and Thorne (1974) the relative intrinsic intensity of radiation emitted by the disk at a given radius is a known function of the radius only, so that it is possible to calculate the exact distribution of observed bolometric flux. Direct and secondary images are plotted and the strong asymmetry in the flux distribution due to the rotation of the disk is exhibited. Finally a simulated photograph is constructed, valid for black holes of any mass accreting matter at any moderate rate.

**Key words:** black holes – accretion disks – geometrical optics

### 1. Introduction

The aim of the present paper is to provide a reply to the question that many people ask themselves about the optical appearance of a black hole.

In order to be visible a black hole has of course to be illuminated, like any ordinary body. One of the simplest possibilities would be for the black hole to be illuminated by a distant localized source which in practise might be a companion star in a loosely bound binary system. A more interesting and observationally important possibility is that in which the light source is provided by an emitting accretion disk around the black hole, such as may occur in a tight binary system with overflow from the primary, and perhaps also on a much larger scale in a dense galactic nucleus. The general problem of the optical appearance of black holes is related to the analysis of trajectories in the gravitational field of black holes. For a spherical, static, electrical field-free black hole (whose external space-time geometry is described by the Schwarzschild metric) this problem is already well known (Hagihara, 1931; Darwin, 1959; for a summary, see Misner et al., 1973 [MTW]). In Sect. 2 we give only a brief outline of it with basic equations, trying to point out the major features which will appear later. All our calculations are done in the geometrical optics approximation (for a study of wave-aspects, see Sanchez, 1977). In Sect. 3 we calculate the apparent shape of circular rings orbiting a non-rotating black hole and the results are depicted in Figs. 5–6. In Sect. 4 we recall the standard analysis by Novikov and Thorne

(1973) of the problem of energy release by a thin accretion disk in a general astrophysical context, focusing attention more particularly on the analytic solution for the surface distribution of energy release that was derived by Page and Thorne (1974) in the limiting case of a sufficiently low accretion rate. In terms of this idealized (but in appropriate circumstances, realistic) model, we calculate the distribution of bolometric flux as seen by distant observers at various angles above the plane of the disk (Figs. 9–11).

### 2. Image of a Bare Black Hole

Before analyzing the general problem of a spherical black hole surrounded by an emitting accretion disk, it is instructive to investigate a more simple case in which all the dynamics are already contained, namely the problem of the return of light from a bare black hole illuminated by a light beam projected by a distant source. It is conceptually interesting to calculate the precise apparent pattern of the reflected light, since some of the main characteristic features of the general geometrical optics problem are illustrated thereby.

The Schwarzschild metric for a static pure vacuum black hole may be written as:

$$ds^2 = -\left(1 - \frac{2M}{r}\right) dt^2 + \left(1 - \frac{2M}{r}\right)^{-1} dr^2 + r^2(d\theta^2 + \sin^2\theta d\phi^2) \quad (1)$$

where  $r$ ,  $\theta$ , and  $\phi$  are spherical coordinates and the unit system is chosen such that  $G=c=1$ .  $M$  is the relativistic mass of the hole (which has the dimensions of length). In this standard coordinate system the horizon forming the surface of the hole is located at the Schwarzschild radius  $r_s = 2M$ .

One can take advantage of the spherical symmetry to choose the "equatorial" plane  $\theta = \pi/2$  so as to contain any particular photon trajectory under consideration. The trajectories will then satisfy the differential equation:

$$\left\{ \frac{1}{r^2} \left( \frac{dr}{d\phi} \right)^2 + \frac{1}{r^2} \left( 1 - \frac{2M}{r} \right) \right\} = 1/b^2. \quad (2)$$

The second term in the left member can be interpreted as an effective potential  $V(r)$ , in analogy with the non-relativistic mechanics. The motion does not depend on the photon energy  $E$  and on its angular momentum  $L$  separately, but only on the ratio  $L/E = b$ , which is the impact parameter at infinity.

Let the observer be in a direction fixed by the polar angle  $\phi_0$  in the Schwarzschild metric, at a radius  $r_0 \gg M$ . The rays emitted by a distant source of light and deflected by the black hole intersect the observer's detector (for example a photographic plate) at a

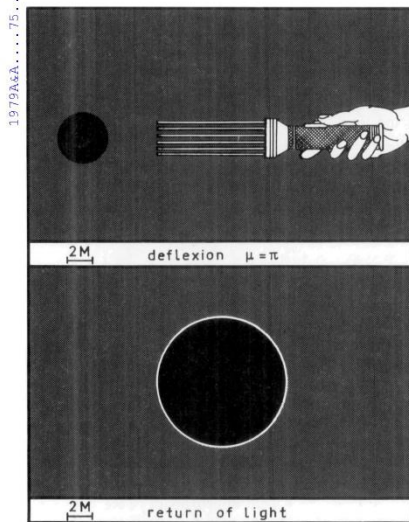


Fig. 2. Return of light deflected by 180° from a bare black hole

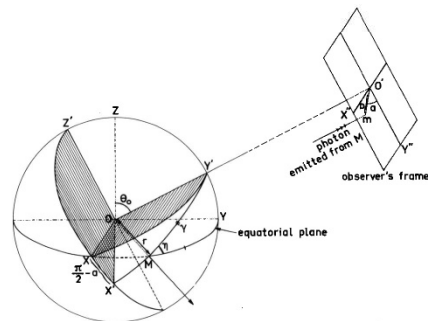


Fig. 3. The coordinate system (see text)

on a  $\Theta$ -direction. It follows from the above discussion that rays that reach the observer will give a picture consisting of a black disk of radius  $b_c = 5.19695 M$  surrounded by "ghost" rings of different radius and brightness. The exterior ring corresponds to the rays that have not described any circuit; as  $b$  approaches its critical value  $b_c$ , the rays describe more and more circuits, until in the limit  $b_\infty = b_c$  (infinite circuits) the rays are captured.

The external ring is the brightest one; as we see from (8), the brightness decreases exponentially from the external ring to the internal ones.

One can ask for what values of  $\Theta = \pi - \mu$  the rings are most visible. It is obvious that, if the observer is placed at an angle  $\Theta$

from the direction of incidence close to  $\pi$ , he will not see rings of brightness since almost all the observed photons at small deviations come from large impact parameter, for which circuiting does not take place. In fact, it is clear that the most favourable condition is  $\theta = 0$ , i. e. the rays are deflected by  $\mu = \pi$ . Figure (2) gives the corresponding image; the radius of the external ring is  $b_1 = 5.341 M$ ; this is already near the rim of the black disk of radius  $5.197 M$ . The following rings fall at distances even closer, equal respectively to  $0.00028 M$ ,  $0.00000056 M$ ,  $0.000000012 M$ , etc.

To conclude this section, the only ring practically distinguishable would be the external one. This is not only a matter of brightness, but also a matter of resolution.

### 3. Image of a Clothed Black Hole

Let us now assume that the source of radiation is an emitting accretion disk orbiting around the black hole; the astrophysical properties of such an object will be briefly discussed in the next section. Let the thickness of the disk be negligible with respect to  $M$ , so that it is considered as lying in the equatorial plane of the Schwarzschild black hole. The coordinate system is chosen as in Fig. 3. The observer lies in the fixed direction  $\theta_0$ ,  $\phi_0 = 0$  (plane  $YOZ$ ) at a distance  $r_0 \gg M$ . We consider the disk as an assembly of idealized particles emitting isotropically. Starting from an emitting particle with Schwarzschild coordinates  $(r, \phi)$ , a typical trajectory whose asymptotic direction is the observer's direction  $OO'$  lies in the plane  $OX''Y'$  and reaches the photographic plate (which is the plane  $O'X''Y''$ ) at a point  $m$ , determined by its polar coordinates  $(b, \alpha)$ .

Assuming that the observer is practically at infinity and at rest in the gravitational field of the black hole, then the polar distance from  $m$  to  $O'$  is precisely the impact parameter of the trajectory, and the polar angle  $\alpha$  with the "vertical" direction  $O'Y''$  is the complement of the dihedral angle between planes  $OXY'$  and  $OX''Y'$ . For a given coordinate  $r$ , varying  $\phi$  from  $0$  to  $\pi$  (the figure being symmetric with respect to  $O'Y''$ -axis), we get the apparent shape  $b(r) = b(r, \alpha)$  on the photographic plate of the circular ring orbiting the black hole at distance  $r$ .

As seen in the previous section, rays emitted from a given point  $M$  can circle around the black hole before escaping to infinity, giving an infinite series of images on the photographic plate; the same arguments indicate that only the secondary image (which corresponds to rays that have circuted once) has to be taken into account, images of higher order being almost exactly superposed at the critical value  $b_c$ . Thus, for a given emitter  $M$ , the observer will detect generally two images, a *direct (or primary) image* at polar coordinates  $(b^{(0)}, \alpha)$  and a *ghost (or secondary) image* at  $(b^{(0)}, \alpha + \pi)$ .

Relationships between the different angles involved by the problem follow directly from the resolution of spherical triangles  $XYM'$  and  $XM'X''$  (Fig. 3). We get:

$$\cos \alpha = \cot \phi \cos \theta_0 / \sin \gamma = \cos \phi \cos \theta_0 (1 - \sin^2 \theta_0 \cos^2 \phi)^{-1/2} \quad (9)$$

so that  $\alpha$  is a monotonic increasing function of  $\phi$ .

We need also the relation

$$\cos \gamma = \cos \alpha (\cos^2 \alpha + \cot^2 \theta_0)^{-1/2}. \quad (10)$$

Calculation of curves  $b^{(0)}(\alpha)$ ,  $b^{(0)}(\alpha)$  at fixed  $r$  is performed with a computer. Nevertheless, prior to any precise drawing, we can foresee some characteristic features of the shape of our object by simply considering particular orbits in the plane  $\{\phi = 0\}$  for strong inclination ( $\theta_0 = 80^\circ$ ; Fig. 4). Already we can point out that one of

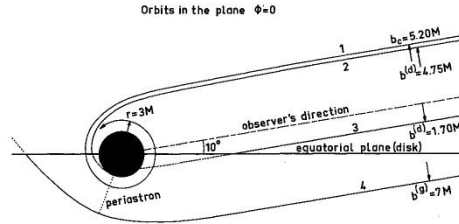


Fig. 4. Illustrative orbits in the plane  $\{\phi=0\}$ . Trajectory 1 has the critical impact parameter and circles infinitely around the black hole; trajectories 2 and 3 give direct images, trajectory 4 gives a secondary image

the main differences from the problem of the previous section is that not all orbits have necessarily a periastron, or equivalently an impact parameter greater than the critical value  $b_c$ . For example, the trajectory 2 is emitted outside the horizon, at a distance  $2.60 M$ , and reaches the observer with an impact parameter  $b^{(a)} = 4.75 M$ , lesser than  $b_c = 5.20 M$  (in fact, this trajectory is only theoretically possible, but physically no photon will be emitted so near the horizon, see next section). More significant is the trajectory 3, which is emitted at  $r = 9.80 M$  from the center of the hole but gives a direct image at only  $b^{(a)} = 1.70 M$ . Clearly this is a pure projection effect, already encountered in a newtonian context when one observes Saturn's rings near the equatorial plane. Furthermore, the very small values of  $b^{(a)}$  for trajectories emitted at relatively large  $r$  but small  $\phi$  imply that the orbits are almost purely radial (indeed trajectory 3 is very close to a straight line); thus, we expect the part of accretion disk between the hole and the observer to give direct images with the aspects of newtonian ellipses which project onto the lower part of the black spot. Figure 4 shows another characteristic feature of the shape: the secondary image is not everywhere in direct juxtaposition to the black spot of radius  $b_c$ . In fact, trajectory 4 illustrates how, in order to reach the of radius  $b_c$ . In fact, trajectory 4 illustrates how, in order to reach the observer at strong inclination, a photon emitted behind the hole necessarily suffers a weak deviation, and hence has an orbit with large periastron and impact parameter; so, we can presume that the secondary image is really dropped forward the observer's direction (i. e. at relatively small values of  $\phi$ ), while on the opposite side it remains crushed around the black spot (at values of  $\phi$  near  $\pi$ ).

Now, to get more insight into the mathematics, it is interesting to write down explicitly some algebraic formulas for orbits having a periastron distance  $P$ . For the direct image, Eq. (3) leads to:

$$\gamma = \frac{1}{\sqrt{2M}} \int_0^{1/r} (G(x))^{-1/2} dx = 2(P/Q)^{1/2} \{F(\zeta_r, k) - F(\zeta_\infty, k)\} \quad (11)$$

where

$$k^2 = \frac{Q-P+6M}{2Q}, \quad \sin^2 \zeta_\infty = \frac{Q-P+2M}{Q-P+6M}, \quad \sin^2 \zeta_r = \frac{Q-P+2M+4MP/r}{Q-P+6M} \quad (12)$$

We deduce:

$$\frac{1}{r} = -\frac{Q-P+2M}{4MP} + \frac{Q-P+6M}{4MP} \sin^2 \left\{ \frac{\gamma}{2} \sqrt{P/Q} + F(\zeta_\infty, k) \right\} \quad (13)$$

Given  $P$ , from (10) and (13) we get a relation  $r = r(\alpha, P)$ , and from (5) we obtain  $b^{(a)} = b^{(a)}(r, \alpha)$  for a given angle  $\theta_0$ .

We can thus draw the *isoradial* curves (corresponding to trajectories emitted at constant coordinate  $r$  from the hole)  $b^{(a)} = b^{(a)}(\alpha)$  in polar coordinates.

In the newtonian limit,  $b = P$  and  $\sin \sim \sin$ , so that (13) reduces to  $b^{(a)} = r \sin \gamma = r(1 + \text{tg}^2 \theta_0 \cos^2 \alpha)^{-1/2}$ , which is obviously the equation of an ellipse of semi-major axis  $r$  along  $O'X''$  and eccentricity  $\sin \theta_0$ .

More generally, for the  $(1+n)$ th order image, Eq. (11) must be replaced by  $2n\pi - \gamma = 2(P/Q)^{1/2} \{2K(k) - F(\zeta_\infty, k) - F(\zeta_r, k)\}$  for orbits whose periastron is located between the point of emission and the infinity (that is the case for  $r$  slightly greater than  $3M$ ). Of course, here, if the disk is optically thick, a photon whose trajectory intersects the disk would be reabsorbed and will not reach infinity. As we shall discuss later, the realistic physical situation is mostly optically thick.

Without taking account of absorption, redshift or physical emissive properties of the disk near the horizon, we have drawn in Figs. 5-6 the direct images of circular rings orbiting at  $r = 2M$ ,  $r = 6M$ ,  $r = 10M$ ,  $r = 20M$ ,  $r = 30M$  and the secondary images for  $r = 6M$ ,  $r = 10M$ ,  $r = 30M$  and  $r = \infty$ , for two values of the inclination angle  $\theta_0$ .

The qualitative features foreseen above become clearly apparent, specially in Fig. 6; if we superpose newtonian ellipses for corresponding values of  $r$ , the curves fit perfectly up to fairly large values of  $\alpha$ , of the order of  $70^\circ$ , the deformation becoming drastic only for the part of the ring behind the hole.

In practise, it is clear that, taking account of realistic physical properties of the accretion disk, what we would in fact observe through a telescope would be dramatically different from the mushroom of Fig. 6! The purpose of the following section is to study the actual distribution of flux that would really be observed.

#### 4. Realistic Appearance of a Black Hole Accretion Disk

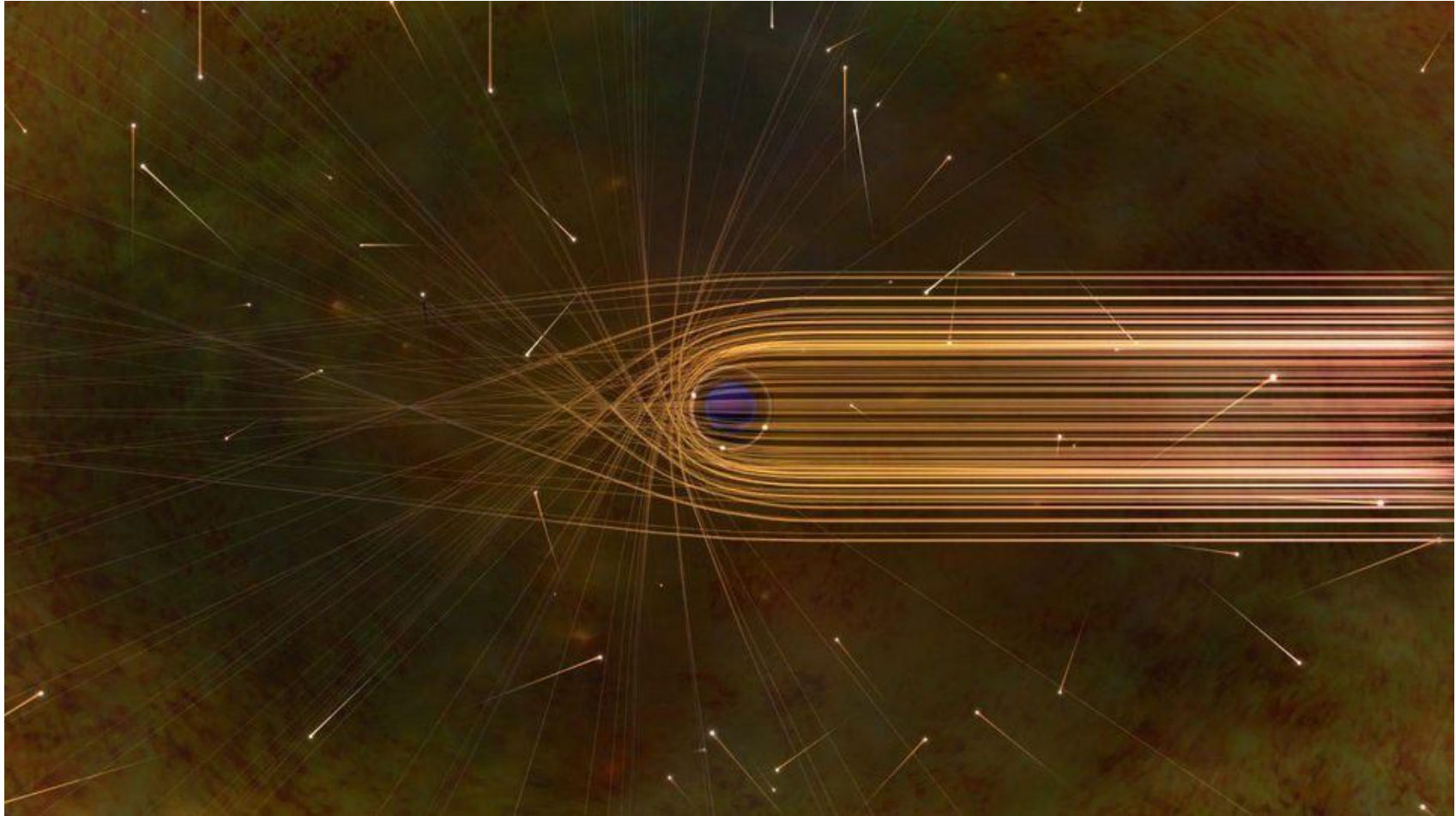
Until now we have considered the geometrical optics about a theoretical object consisting of a black hole surrounded by a thin accretion disk. It is appropriate at this stage to ask oneself what could be the relevance of such an object in astrophysics.

From an observational point of view, this problem is of importance: since a stationary black hole does not radiate either electromagnetic or gravitational waves, it could be detected only indirectly through its gravitational influence on the ambient medium.

Moreover, with recent discoveries of intense discrete X-ray sources with rapid variability, a considerable interest has focused upon gaz accretion onto compact objects such as neutron stars and black holes, and it is now currently admitted that accretion is probably the main process involved in a larger number of high-energy astrophysical situations, ranging from novae to quasars and other kinds of active galactic nuclei (see for instance Eardley and Press, 1975; Lightman et al., 1975).

Models of black holes with accreting medium are generally considered in the context of black holes in orbit about "normal" stars (binary systems) or supermassive black holes ( $M \gtrsim 10^7 M_\odot$ ) which might reside at the centers of some active galactic nuclei (Lynden-Bell, 1969; Hills, 1975).

In both situations, the accreting matter is likely to have high specific angular momentum, so that the accretion would be far from spherical, but only axisymmetric with the matter flattened in the form of a more or less thin disk.





When Radioastron mission was under preparation N. S. Kardashev requested to analyse fundamental physics effects which could be observed with these facilities.



## Measuring the black hole parameters in the galactic center with RADIOASTRON

A.F. Zakharov<sup>a,b,c,\*</sup>, A.A. Nucita<sup>d</sup>, F. DePaolis<sup>d</sup>, G. Ingresso<sup>d</sup>

<sup>a</sup> *Institute of Theoretical and Experimental Physics, 25, B. Chermushinskaya st., Moscow 117259, Russia*

<sup>b</sup> *Space Research Centre of Lebedev Physics Institute, Moscow, Russia*

<sup>c</sup> *Joint Institute for Nuclear Research, Dubna, Russia*

<sup>d</sup> *Dipartimento di Fisica, Università di Lecce and INFN, Sezione di Lecce, Italy*

Received 19 January 2005; accepted 21 February 2005

Available online 23 March 2005

Communicated by F. Melchiorri

### Abstract

Recently, Holz and Wheeler (2002) [ApJ 578, 330] considered a very attracting possibility to detect retro-MACHOs, i.e., retro-images of the Sun by a Schwarzschild black hole. In this paper, we discuss glories (mirages) formed near rapidly rotating Kerr black hole horizons and propose a procedure to measure masses and rotation parameters analyzing these forms of mirages. In some sense that is a manifestation of gravitational lens effect in the strong gravitational field near black hole horizon and a generalization of the retro-gravitational lens phenomenon. We analyze the case of a Kerr black hole rotating at arbitrary speed for some selected positions of a distant observer with respect to the equatorial plane of a Kerr black hole. Some time ago Falcke, Melia, Agol (2000) [ApJ 528, L13S] suggested to search shadows at the Galactic Center. In this paper, we present the boundaries for shadows. We also propose to use future radio interferometer RADIOASTRON facilities to measure shapes of mirages (glories) and to evaluate the black hole spin as a function of the position angle of a distant observer.

© 2005 Elsevier B.V. All rights reserved.

PACS: 97.60.L; 04.70; 95.30.S; 04.20; 98.62.S

Keywords: Black hole physics; Gravitational lenses; Microlensing

### 1. Introduction

Recently Holz and Wheeler (2002) have suggested that a Schwarzschild black hole may form retro-images (called retro-MACHOs) if it is illuminated by the Sun. We analyze a rapidly rotating

\* Corresponding author. Tel.: +7 095 1299759; fax: +7 095 8839601.

E-mail address: [zakharov@itep.ru](mailto:zakharov@itep.ru) (A.F. Zakharov).



ELSEVIER



## New Astronomy Top Cited Article 2005-2010

Awarded to:

*Zakharov, A.F., Nucita, A.A., Depaolis, F., Ingrosso, G.*

For the paper entitled:

“Measuring the black hole parameters in the galactic center with  
RADIOASTRON”

This paper was published in:

New Astronomy, Volume 10, Issue 6, 2005

---

*David Clark*

*Senior Vice President, Physical Sciences I  
Amsterdam, The Netherlands*

---



INTERNATIONAL SERIES OF  
MONOGRAPHS ON PHYSICS 69

The  
Mathematical Theory  
of Black Holes

S. Chandrasekhar

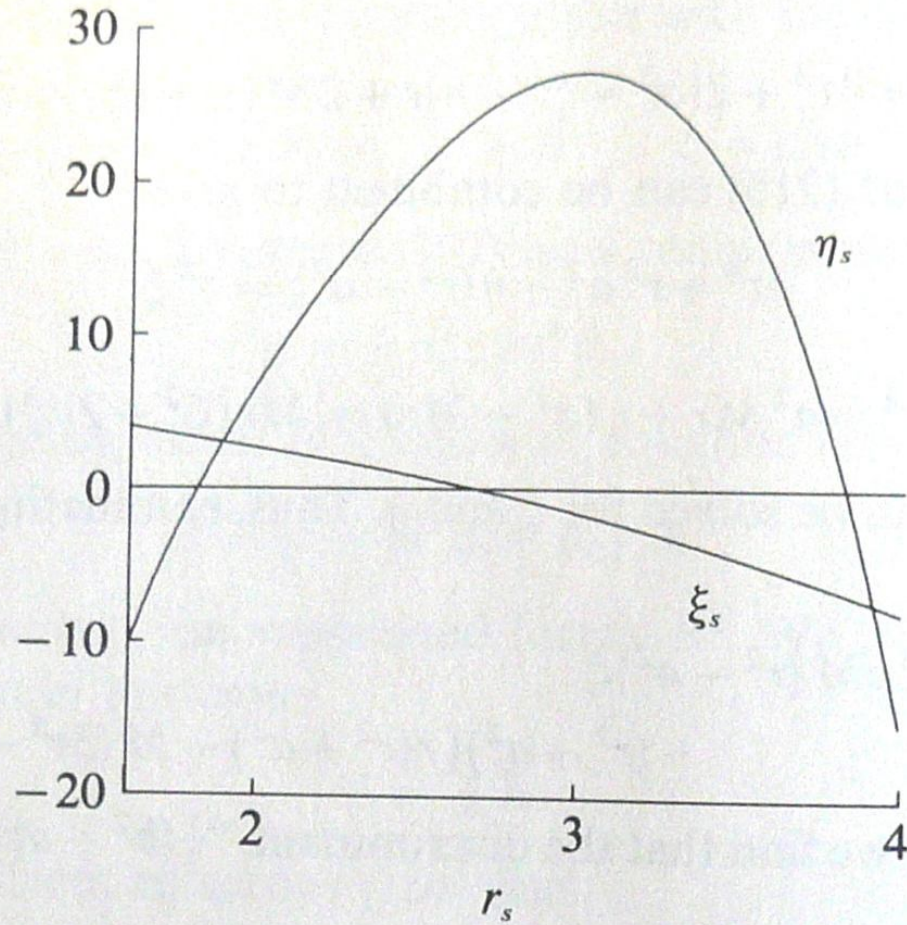


FIG. 34. The locus  $(\xi_s, \eta_s)$  determining the constants of the motion for three-dimensional orbits of constant radius described around a Kerr black-hole with  $a = 0.8$ . The unit of length along the abscissa is  $M$ .

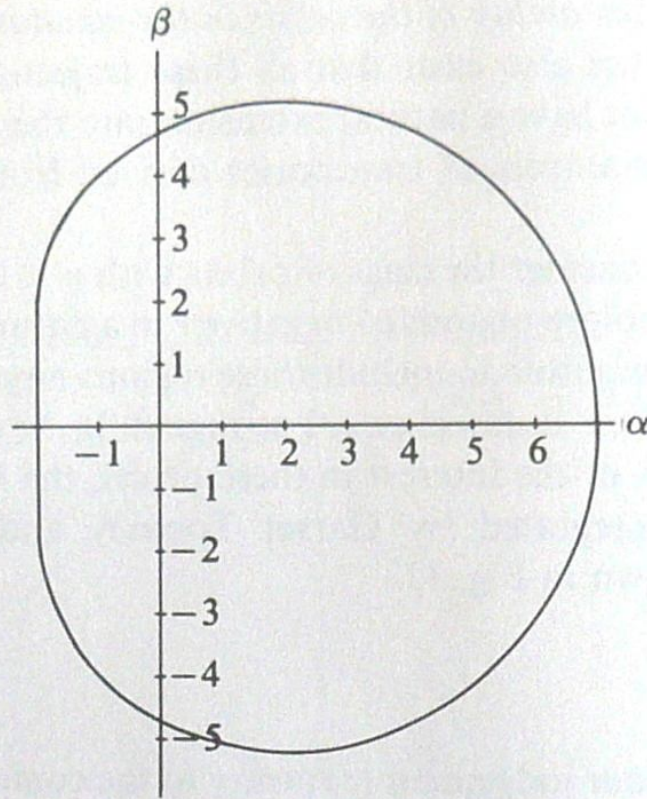


FIG. 38. The apparent shape of an extreme ( $a = M$ ) Kerr black-hole as seen by a distant observer in the equatorial plane, if the black hole is in front of a source of illumination with an angular size larger than that of the black hole. The unit of length along the coordinate axes  $\alpha$  and  $\beta$  (defined in equation (241)) is  $M$ .

black hole from infinity, the apparent shape will be determined by

$$(\alpha, \beta) = [\xi, \sqrt{\eta(\xi)}]. \quad (242)$$

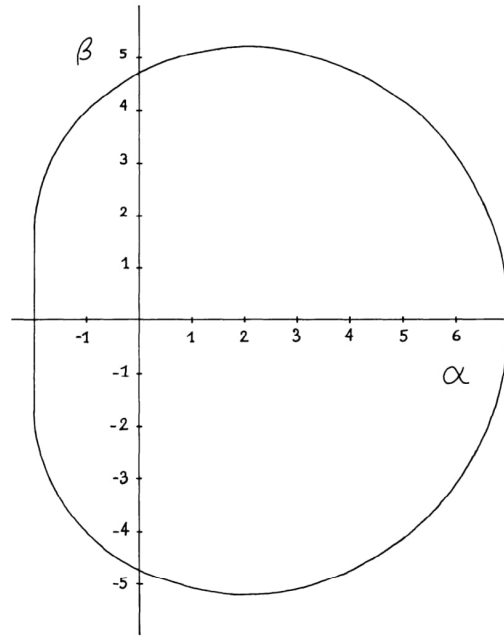


Figure 6. The apparent shape of an extreme ( $a = m$ ) Kerr black hole as seen by a distant observer in the equatorial plane, if the black hole is in front of a source of illumination with an angular size larger than that of the black hole.

is largest there and because of the gravitational focusing effects associated with the bending of the rays toward the equatorial plane. Note that the radiation comes out along the flat portion of the apparent boundary of the extreme black hole as plotted in Figure 6.

#### D. Geometrical Optics

A detailed calculation of the brightness distribution coming from a source near a Kerr black hole requires more of geometrical optics than the calculation of photon trajectories. I will now review some techniques which are useful in making astrophysical calculations in connection with black holes.

The fundamental principle can be expressed as the conservation of photon density in phase space along each photon trajectory. A phase space element  $d^3x d^3p$ , the product of a proper spatial volume element and a physical momentum-space volume element in a local observer's frame of reference, is a Lorentz invariant, so the particular choice of local observer is arbitrary. The density  $N(x^\alpha, p^{(\beta)})$  is defined

## Types of unbound geodesics in the Kerr metric

A. F. Zakharov

*Institute of Theoretical and Experimental Physics, Academy of Sciences of the USSR, Moscow*  
(Submitted 4 December 1985)  
Zh. Eksp. Teor. Fiz. **91**, 3-6 (July 1986)

Sets of constants of motion of a particle that correspond to different types of  $r$ -motion are considered. The topology of these sets is determined and a number of constants characterizing these sets are found.

### INTRODUCTION

An important problem in the study of unbound motion of particles in the Kerr metric is the description of the set of constants of motion for which a particle traveling from infinity goes below the horizon of a black hole. We shall give a qualitative description of this set and also of the set of constants of motion for which the particle asymptotically approaches a sphere placed around the black hole, and the sets of constants of motion for which the particle departs to infinity. The solution of this problem is important in connection with the accretion of noninteracting particles on a rotating black hole.

It is well-known that Kepler orbits are characterized by two constants ( $E$  and  $L$ ), since we can identify orbits that can transform into one another by rotations through the Euler angles. Hence, orbits in the Schwarzschild metric are also characterized by two constants. It turns out that a change in the radial coordinate in the Kerr metric is determined by only three constants in the case of moving particles (because the particle mass characterizes the connection between the affine parameter and the proper time of the particle, and the affine parameter can be chosen to be the proper time of the particle), and two constants in the case of the motion of photons (because of the photon energy characterizes the set of different affine parameters in the equation for the change in the  $r$  coordinate.)

### 1. BASIC NOTATION

The equation of motion for the radial variable in the Kerr metric is<sup>1</sup>

$$\begin{aligned} \rho^4 (dr/d\tau)^2 &= R(r), & (1) \\ R(r) &= r^4 + (a^2 - \xi^2 - \eta) r^2 + 2M[\eta + (\xi - a)^2] r - a^2 \eta \quad (\text{Photons}), \\ R(r) &= r^4 + (a^2 - \xi^2 - \eta) r^2 \\ &\quad + 2M[\eta + (\xi - a)^2] r - a^2 \eta - r^2 \Delta/E \quad (\text{Particles}), \end{aligned}$$

where

$$\rho^2 = r^2 + a^2 \cos^2 \theta, \quad \Delta = r^2 - 2Mr + a^2, \quad a = S/M. \quad (2)$$

The constants  $S$  and  $M$  refer to the black hole, namely,  $S$  is the angular momentum and  $M$  the mass of the black hole. The constants  $E$ ,  $\xi$ , and  $\eta$  refer to the particle, namely,  $E$  is its energy at infinity,  $\xi = L_z/E$  ( $L_z$  is the angular momentum of the particle about the axis of rotation of the black hole), and  $\eta = Q/E^2$  ( $Q$  is given by

$$Q = p_\theta^2 + \cos^2 \theta [a^2 (\mu^2 - E^2) + \sin^2 \theta L_z^2],$$

and  $\mu$  is the mass of the particle). It is readily verified that

the radial motion of the particle depends on the following constants:

$$\hat{a} = a/M, \quad \hat{E} = E/\mu, \quad \hat{\xi} = \xi/M, \quad \hat{\eta} = \eta/M^2.$$

The radial motion of photons does not depend on the constant  $\hat{E}$ . Instead of the coordinate  $r$ , we now introduce  $\hat{r} = r/M$ . (The symbol  $\Lambda$  will be omitted henceforth.) Thus, the character of motion in the  $r$ -coordinate for given value of  $a$  is determined by the three constants  $E$ ,  $\xi$ ,  $\eta$  in the case of a moving particle, and by the two constants  $\hat{\xi}$  and  $\hat{\eta}$  in the case of photons.

Depending on the multiplicities of the roots of the polynomial  $R(r)$  (for  $r \gg r_g$ ), we can have three types of motion in the  $r$ -coordinate,<sup>2</sup> namely:

(1) the polynomial  $R(r)$  has no roots (for  $r \gg r_g$ ). The particle then falls into the black hole;

(2) the polynomial  $R(r)$  has roots and  $r_{\max} > r_g$  ( $r_{\max}$  is the maximum root); for  $(\partial R / \partial r)(r_{\max}) \neq 0$  we then have,  $(\partial R / \partial r)(r_{\max}) > 0$ , and the particle departs to infinity after approaching the black hole;

(3) the polynomial  $R(r)$  has a root and  $R(r_{\max}) = (\partial R / \partial r)(r_{\max}) = 0$ ; the particle now takes an infinite proper time to approach the sphere of radius  $r_{\max}$ .

### 2. DESCRIPTION OF THE SET OF CONSTANTS CORRESPONDING TO DIFFERENT TYPES OF MOTION

We shall now examine the sets of constants of motion  $E$ ,  $\xi$ , and  $\eta$  corresponding to different types of particles motion for a given black-hole rotation parameter  $a = \text{const}$ . Let us cut the space  $E, \xi, \eta$  with the plane  $E = \text{const} > 1$  and describe in this slice the set of constants corresponding to different types of motion. It then turns out that the boundary of the set of constants corresponding to the second type of motion for  $\eta > 0$  is the set of constants for which the motion belongs to the third type. We shall look upon this set as the graph of the function  $\eta = \eta(\xi)$ . We note that the set of these constants as functions  $\xi(r)$  and  $\eta(r)$  was examined by Chandrasekhar<sup>1</sup>. Let us describe some of the properties of the function  $\eta(\xi)$ . If the motion of the particle is of the third type, we have

$$R(r) = 0, \quad (\partial R / \partial r)(r) = 0 \quad (3)$$

for  $\eta > 0, r \gg r_g$ .

Thus, to obtain the function  $\eta(\xi)$ , we must eliminate  $r$  from (3). Assuming that (3) provides an implicit specification of  $r(\xi)$  and  $\eta(\xi)$ , we find that

$$d\eta/d\xi(-\Delta) = 2\xi r^2 - 4(\xi - a)r, \quad (4)$$

$$d\eta/d\xi(-2r+2) + (d/d\xi)(\partial^2 R / \partial r^2) = 4\xi r - 4(\xi - a)$$

for  $r > r_s, \eta > 0$ . We note that, for  $\Delta > 0$  and  $\partial^2 R / \partial r^2 \neq 0$ , the implicit function theorem shows that  $r(\xi)$  and  $\eta(\xi)$  are single-valued functions. Analysis similar to that given in Ref. 3 then shows that, when  $a \neq 1$  or  $\xi \neq 2$ , we have  $\partial^2 R / \partial r^2 > 0$ . When  $a = 1$  and  $\xi = 2$ , we find from (3) that  $\Delta = 0$ . When  $a = 1$ , it is readily verified that the set corresponding to the third type of motion includes the straight segments  $[\xi = 2, 0 < \eta < (3E^4 - 4E^2 + 1)/(E^2(E^2 - 1))]$  (Ref. 4) (for photons,  $\xi = 2, 0 < \eta < 3$ , by analogy with Refs. 5 and 6). It can also be shown that the function  $\eta(\xi)$  has one maximum and  $r(\xi)$  is a monotonically decreasing function.<sup>4</sup> Thus, the set of constants corresponding to the first type of motion is bounded by the curve  $\eta(\xi)$  for  $\eta > 0$ , as shown in Figs. 1 and 2. It is also readily shown that, when  $\eta < 0$  and when  $\eta$  and  $\xi$  are such that the motion of the particle is possible, i.e.,

$$-[a(E^2 - 1)^{1/2}E - |\xi|]^2 \leq \eta < 0, \quad |\xi| \leq a(E^2 - 1)^{1/2}E,$$

the particle is also captured<sup>2</sup> (this set is illustrated in Fig. 2).

### 3. UNBOUND MOTION OF PHOTONS

Chandrasekhar<sup>1</sup> has shown that the condition for capture of a particle in the equatorial plane is the inequality

$$6 \cos [\arccos(-a)/3 + 2\pi/3]$$

$$-a \leq \xi \leq 6 \cos [\arccos(-a)/3] - a. \quad (5)$$

Thus, the functions of  $r(\xi)$  and  $\eta(\xi)$  are defined only for values satisfying the inequalities (5). We also note that the function  $\eta(\xi)$  is a maximum for  $\xi = -2a, r(-2a) = 3(\eta(-2a) = 27)$ . This can be veri-

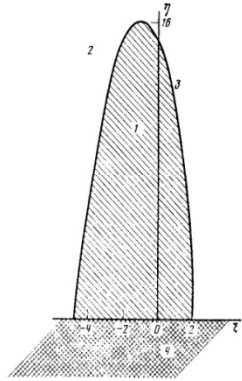


FIG. 1. Different types of particle motion for  $E = 1$  and  $a = 1$ . Region 1—particle trapped, region 2—scattering; curve 3 corresponds to the third type of motion. Region 4 corresponds to values of the constants for which particle motion is impossible.

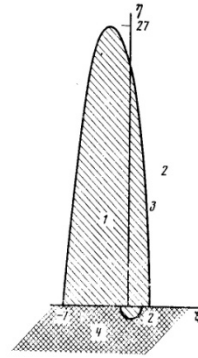


FIG. 2. Same as Fig. 1 for a massless particle and  $a = 1$ .

fied by direct evaluation of (3) and (4). Figure 2 shows a plot of the function  $\eta(\xi)$  for  $a = 1$ .

### 4. MOTION OF PARTICLE OF ARBITRARY ENERGY

Consider a moving particle of arbitrary energy at infinity ( $E > 1$ ). It can be verified that, if

$$\eta_{\max} = \frac{-(\alpha^2 - 18\alpha - 27) + (\alpha^4 + 28\alpha^2 + 270\alpha + 972\alpha + 729)^{1/2}}{2E^2\alpha}, \quad (6)$$

$$r_{\max} = (8\alpha^2/27 + \eta_{\max}E^2\alpha(\alpha/3 + 1))^{1/2} - 2\alpha/3,$$

$$\xi_{\max} = 2a/(r_{\max} - 2),$$

where  $\alpha = (E^2 - 1)^{-1}$ , these values ensure that  $R(r)$  and  $\partial R / \partial r$  vanish, i.e., they satisfy (3). We also note that, for values chosen in accordance with (6), the right-hand side of the first equation in (4) vanishes, i.e., these values correspond to the maximum of  $\eta(\xi)$ . The values  $\eta_{\max}$  and  $r_{\max}$  turn out to be equal to the corresponding values of these quantities for  $a = 0$  (Schwarzschild metric).<sup>7</sup>

### 5. ONE CASE OF UNBOUND PARTICLE MOTION

Consider a case of unbound particle motion for  $E = 1$ . If the motion takes place in the equatorial plane,  $\eta = 0$  (Ref. 8) and

$$R(r) = 2r^2 - \xi^2 r^2 + 2(a - \xi)^2 r. \quad (7)$$

The motion then belongs to the third type if  $\xi^4 = 16(a - \xi)^2$ , and  $r = \xi^2/4$ . It follows that there are only two values that correspond to the third type of motion in the equatorial plane, namely,  $\xi = -2 - 2(1 + a)^{1/2}$  and  $\xi = 2 + 2(1 - a)^{1/2}$ . Thus, the domain of definition of  $\eta(\xi)$  is the segment  $[-2(1 + (1 + a)^{1/2}), 2(1 + (1 - a)^{1/2})]$ . The domain of variation of the function  $r(\xi)$  is the segment  $[(1 + (1 - a)^{1/2})^2, (1 + (1 + a)^{1/2})^2]$ . This follows from the fact that  $r(\xi)$  is a monotonically decreasing function of  $\xi$ . When  $a = 0$ , we find that  $\eta(\xi) = 16 - \xi^2$ . When  $E \rightarrow 1$ , we

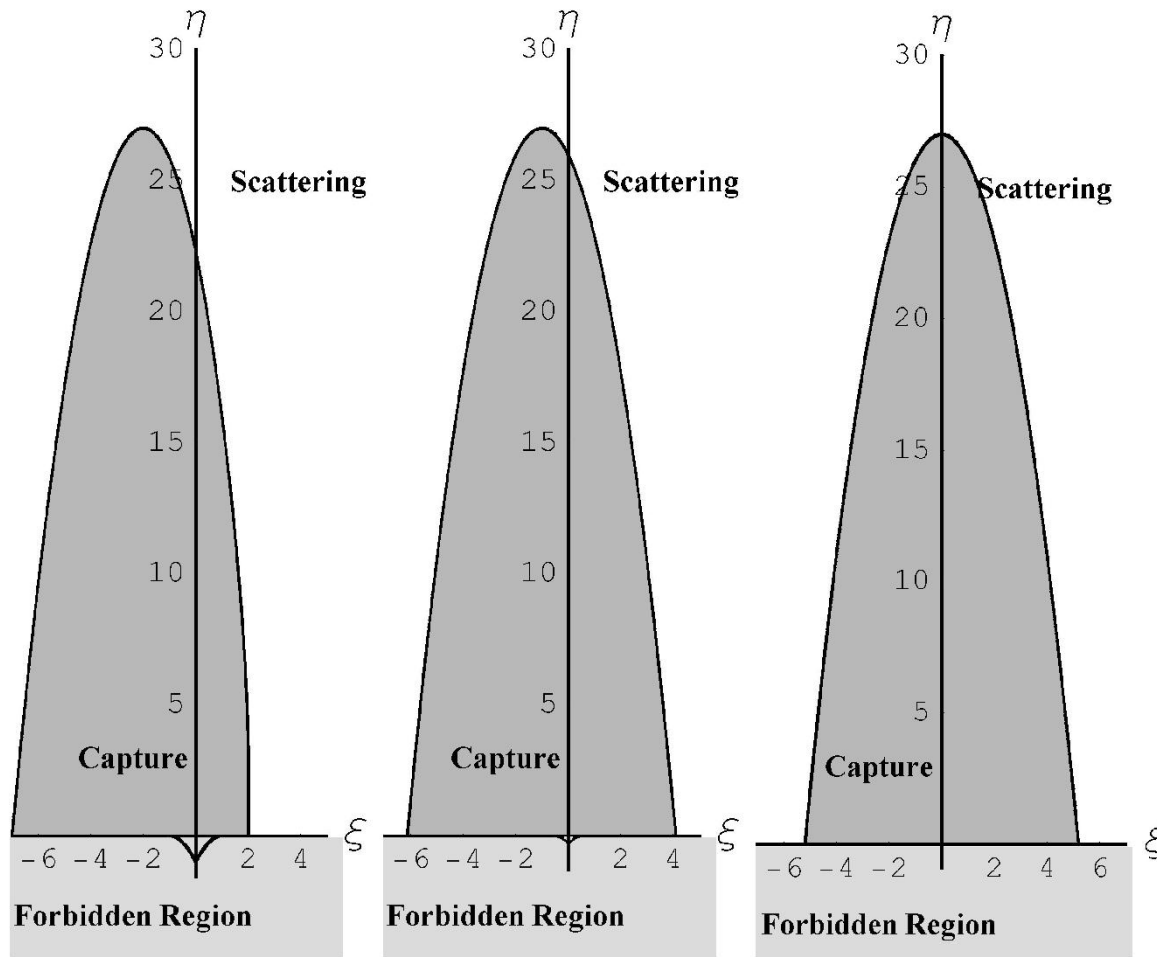


**Fig. 1.** Different types for photon trajectories and spin parameters ( $a = 1., a = 0.5, a = 0.$ ). Critical curves separate capture and scatter regions. Here we show also the forbidden region corresponding to constants of motion  $\eta < 0$  and  $(\xi, \eta) \in M$  as it was discussed in the text.

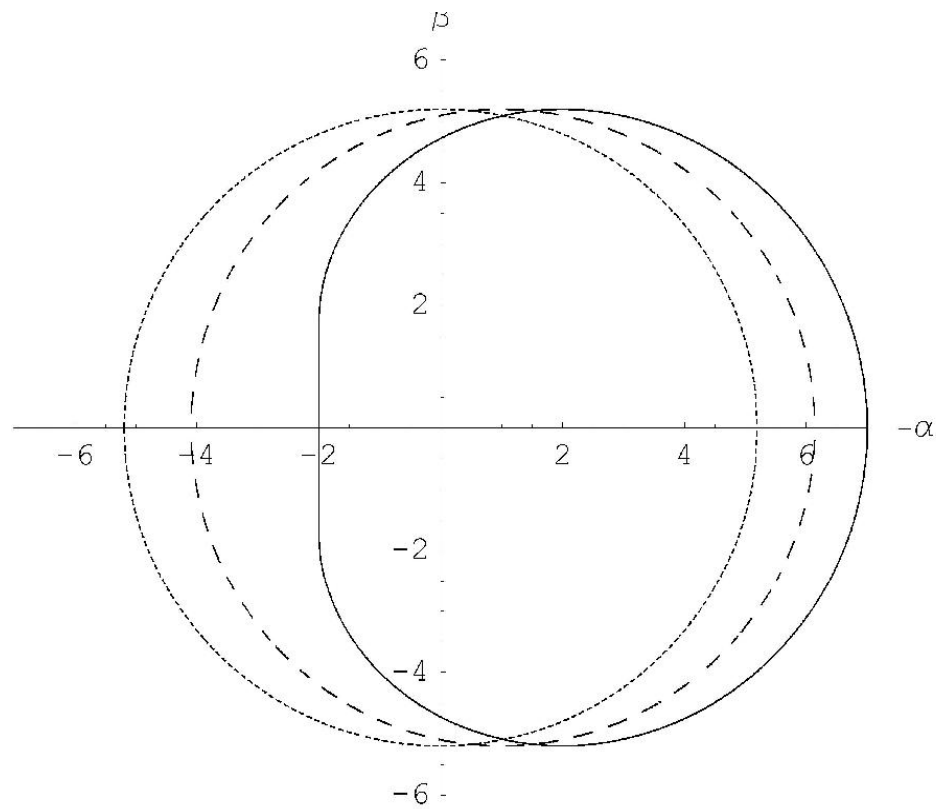


**Fig. 2.** Mirages around black hole for equatorial position of distant observer and different spin parameters. The solid line, the dashed line and the dotted line correspond to  $a = 1$ ,  $a = 0.5$ ,  $a = 0$  correspondingly

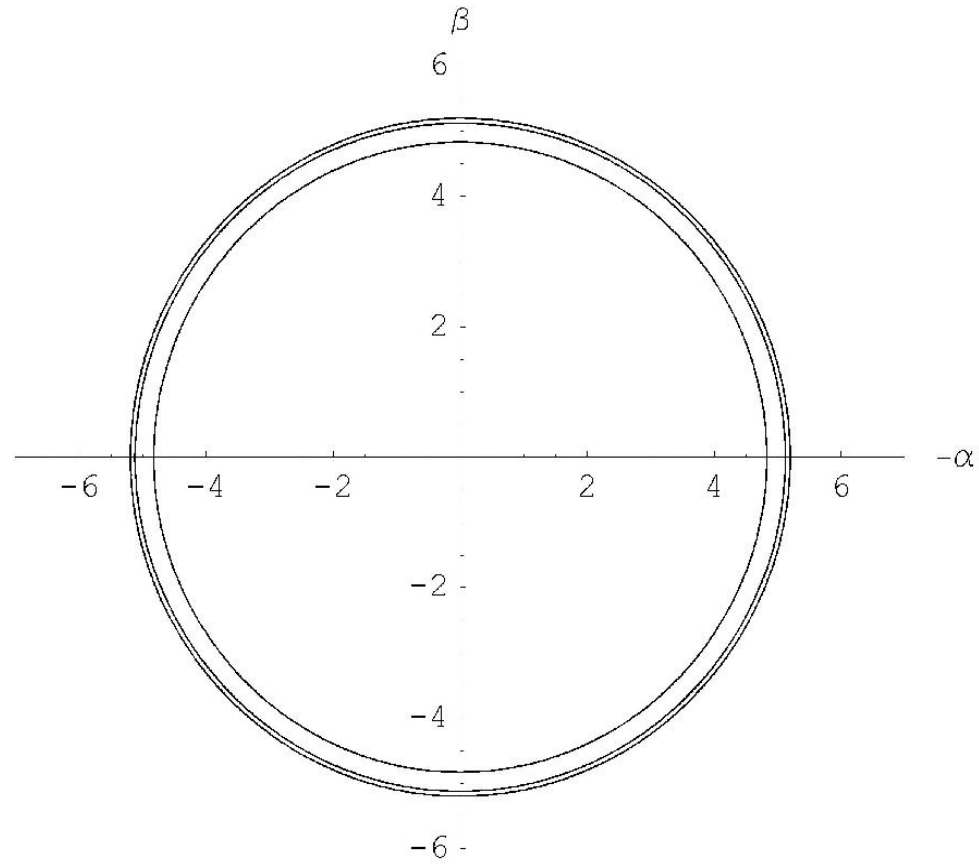


**Fig. 3.** Mirages around a black hole for the polar axis position of distant observer and different spin parameters ( $a = 0, a = 0.5, a = 1$ ). Smaller radii correspond to greater spin parameters.

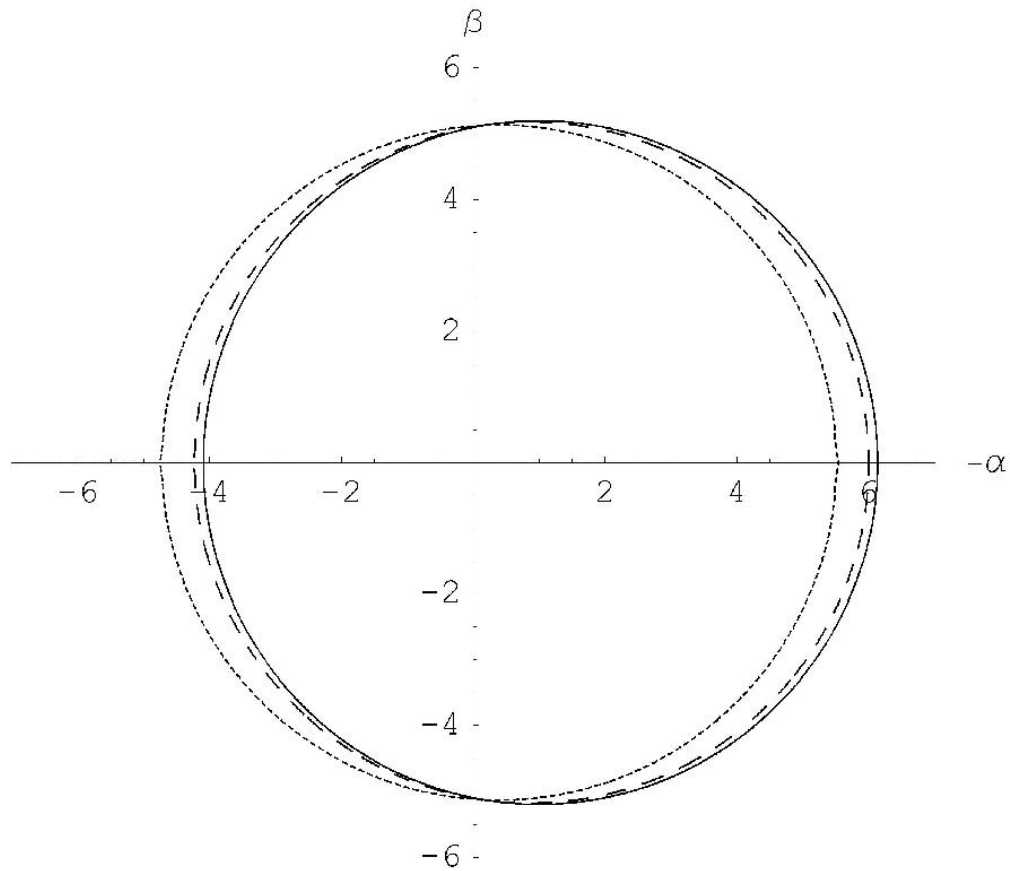


**Fig. 4.** Mirages around black hole for different angular positions of a distant observer and the spin  $a = 0.5$ . Solid, dashed and dotted lines correspond to  $\theta_0 = \pi/2, \pi/3$  and  $\pi/8$ , respectively.

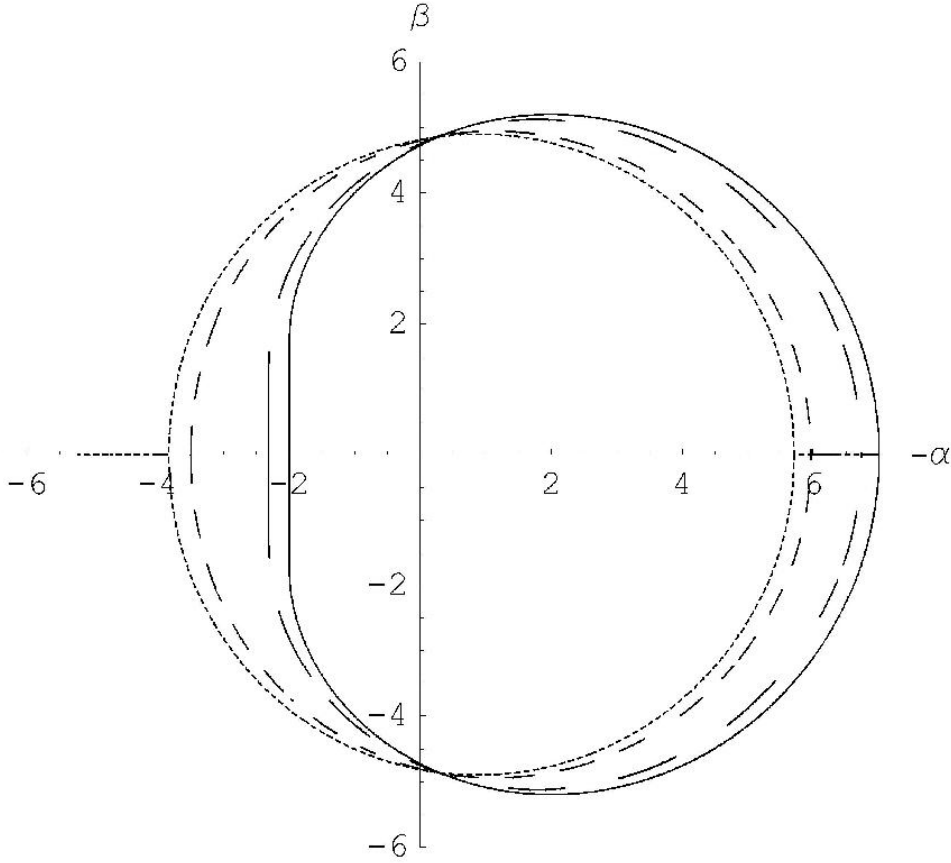


**Fig. 5.** Mirages around black hole for different angular positions of a distant observer and the spin  $a = 1$ . Solid, long dashed, short dashed and dotted lines correspond to  $\theta_0 = \pi/2, \pi/3, \pi/6$  and  $\pi/8$ , respectively.

may not be sufficient to being detectable by RADIOASTRON. However, numerical simulations by Falcke et al. (2000, 2001) give hope that the luminosity could be not too small at least for arcs of images formed by co-rotating photons ( $\alpha > 0$ ). Second, turbulent plasma could give essential broadening of observed images (Bower et al., 2004), the longest interferometer baseline  $b_{\max} \sim 350000$  km (or for higher orbit  $b_{\max} \sim 3.2 \times 10^6$  km) and for this case we have similar to Bower et al. (2004) length scale in the scattering medium is  $l = (D_{\text{scattering}}/D_{\text{GC}}) \times b_{\max} \sim 4.4 \times 10^3$  km (or  $l = 4.4 \times 10^4$  km for the higher orbit). Thus, the scale could be less or more than the predicted and measured values of the inner scale, which are in the range  $10^2$ – $10^{5.5}$  km (Wilkinson et al., 1994; Desai and Fey, 2001; Bower et al., 2004), thus the broadening the images could be essential but it is not very easy to calculate it in details for such parameters.

Recent observations of simultaneous X-ray and radio flares at 3 mm, 7 mm, 1.3 cm and 2 cm with the few-hundred second rise/fall timescales gave indirect evidences that X-ray and radio radiation from the close vicinity of Sgr A\* was detected because of that is the most natural interpretation of these flares (Baganoff et al., 2001). However, another interpretations of these flares could not be ruled out and in this case an optical depth for radio waves at 1.3 cm wavelength toward Sgr A\* may be not very small.

Few years ago a possibility to get images of nearby black holes in X-ray band was discussed by White (2000), Cash et al. (2000), moreover Cash et al. (2000) presented a laboratory demonstration of the X-ray interferometer. If the project will be realized, one could get X-ray images of black holes with  $0.1 \times 10^{-6}$  arcsec resolution, thus using this tool one could detect X-ray images around the Galactic Centre and around the black hole in M87 Galaxy.

One could mention also that if the emitting region has a degenerate position with respect to the line of sight (for example, the inclination angle of an accretion disk is  $\gtrsim 85^\circ$ ) strong bending effects found by Matt et al. (1993) and analyzed later by Zakharov and Repin (2003a) do

In spite of the difficulties of measuring the shapes of images near black holes is so attractive challenge to look at the “faces” of black holes because namely the mirages outline the “faces” and correspond to fully general relativistic description of a region near black hole horizon without any assumption about a specific model for astrophysical processes around black holes (of course we assume that there are sources illuminating black hole surroundings). No doubt that the rapid growth of observational facilities will give a chance to measure the mirage shapes using not only RADIOASTRON facilities but using also other instruments and spectral bands (for example, X-ray interferometer MAXIM (White, 2000; Cash et al., 2000) or sub-mm VLBI array (Miyoshi, 2004)). Astro Space Centre of Lebedev Physics Institute proposed except the RADIOASTRON mission and developed also space based interferometers (Millimetron and Sub-millimetron) for future observations in mm and sub-mm bands. These instruments could be used for the determination of shadow shapes.

## References

- Aschenbach, B., Grosso, N., Porquet, D., Predehl, P., 2004. *A&A* 417, 71.
- Baganoff, F.K., et al., 2001. *Nature* 413, 45.
- Beloborodov, A., 2002. *ApJ* 566, L85.
- Bower, F.C., Falcke, H., Sault, R.J., Backer, D.C., 2002. *ApJ* 571, 843.
- Bower, F.C., Wright, M.C.H., Falcke, H., Backer, D.C., 2003. *ApJ* 588, 331.
- Bower, F.C., Falcke, H., Herrstein, R.M., et al., 2004. *Scienceexpress*, Available from: <www.scienceexpress.org/1April2004/>.
- Bozza, V., 2002. *PRD* 66, 103001.
- Bozza, V., 2003. *PRD* 67, 103006.
- Bozza, V., Mancini, L., 2004a. *GRG* 36, 435.
- Bozza, V., Mancini, L., 2004b. Available from: <astro-ph/0404526>.
- Carter, B., 1968. *Phys. Rev.* 174, 1559.
- Cash, W., Shipley, A., Osterman, S., Joy, M., 2000. *Nature* 407, 160.
- Ciufolini, I., Ricci, F., 2002. *CQG* 19, 3863.
- Ciufolini, I., Ricci, F., 2003. *gr-qc/0301030*.
- Chandrasekhar, S., 1983. *Mathematical Theory of Black Holes*. Clarendon Press, Oxford.
- De Paolis, F., Gerialico, A., Inghrosso, G., Nucita, A.A., 2003.

AFZ et al., NA (2005): “No doubt that the rapid growth of observational facilities will give a chance to measure the mirage shapes... using... sub-mm VLBI array (Miyoshi, 2004).”

## Direct measurements of black hole charge with future astrometrical missions (*Research Note*)

A. F. Zakharov<sup>1,2,3,4</sup>, F. De Paolis<sup>5</sup>, G. Ingrosso<sup>5</sup>, and A. A. Nucita<sup>5</sup>

<sup>1</sup> National Astronomical Observatories of Chinese Academy of Sciences, 20A Datun Road, Chaoyang District, Beijing 100012, PR China

<sup>2</sup> Institute of Theoretical and Experimental Physics, 25 B. Cherenushkinskaya st., Moscow 117259, Russia  
e-mail: zakharov@itep.ru

<sup>3</sup> Astro Space Centre of Lebedev Physics Institute, 84/32, Profsoyuznaya st., Moscow 117810, Russia

<sup>4</sup> Joint Institute for Nuclear Research, Dubna, Russia

<sup>5</sup> Department of Physics, University of Lecce and INFN, Section of Lecce, via Arnesano, 73100 Lecce, Italy

Received 13 May 2005 / Accepted 26 July 2005

### ABSTRACT

Recently, Zakharov et al. (2005a, *New Astron.*, 10, 479) considered the possibility of evaluating the spin parameter and the inclination angle for Kerr black holes in nearby galactic centers by using future advanced astrometrical instruments. A similar approach which uses the characteristic properties of gravitational retro-lensing images can be followed to measure the charge of a Reissner-Nordström black hole. Indeed, in spite of the fact that their formation might be problematic, charged black holes are objects of intensive investigations. From a theoretical point of view, it is well-known that a black hole is described by only three parameters, namely, its mass  $M$ , angular momentum  $J$ , and charge  $Q$ . Therefore, it would be important to have a method for measuring all these parameters, preferably by independent model of any. In this paper, we propose a procedure to measure the black hole charge by using the size of the retro-lensing images that can be revealed by future astrometrical missions. A discussion of the Kerr-Newmann black hole case is also offered.

**Key words.** black hole physics – astrometry – gravitation – gravitational lensing – galaxies: nuclei

### 1. Introduction

“Black holes have no hair” means that a black hole is characterized by only three parameters (“hairs”), its mass  $M$ , angular momentum  $J$ , and charge  $Q$  (see, e.g. Misner et al. 1973; Wald 1984 or Heusler 1998 for a more recent review). Therefore, in principle, charged black holes can be formed, although astrophysical conditions that lead to their formation may look rather problematic: see, for example, Zamir (1993); Ruffini et al. (1999); Ruffini et al. (2000); Lee et al. (2001); Perjes & Vasuth (2003); Ray et al. (2003); Moderski & Rogatko (2004); Vogt & Letelier (2004); Lemos & Weinberg (2004); Sereno (2004); Ghezzi & Letelier (2005). Nevertheless, one can not claim that their existence is forbidden by theoretical or observational arguments.

Charged black holes are also objects of intensive studies, since they are described by Reissner-Nordström geometry which is a static, spherically symmetrical solution of Yang-Mills-Einstein equations with fairly natural requirements on asymptotic behavior of the solutions (Gal'tsov & Ershov 1988; Gal'tsov et al. 1989; Gal'tsov & Ershov 1989; Lee et al. 1991). The Reissner-Nordström metric thus describes a

spherically symmetric black hole with a color charge and (or) a magnetic monopole (see also Heusler 1998).

The formation of retro-lensing images (also known as mirage, shadows, or “faces” in the literature) due to the strong gravitational field effects near black holes has been investigated by several authors (Holz & Wheeler 2002; De Paolis et al. 2003; De Paolis et al. 2004; Zakharov et al. 2005a,b,c). The question that naturally arises is whether these images are observable or not. It has been shown that the retro-lensing image around the black hole at the Galactic Center (Sgr A\*) due to S<sub>2</sub> star is observable in the  $K$ -band (peaked at  $2.2 \mu\text{m}$ ) by the next generation infra-red space-based missions. The effects of retro-lensing image shapes due to black hole spin has also been investigated (De Paolis et al. 2004; Zakharov et al. 2005a,c,e).

In this paper we focus on the possibility of measuring the black hole charge as well, and we present an analytical dependence of mirage size on the black hole charge. Indeed, future space missions like Radioastron in radio band or MAXIM in X-ray band have angular resolution close to the shadow size for massive black holes in the center of our own and nearby galaxies.

$$R(r_{max}) = 0, \quad \frac{\partial R}{\partial r}(r_{max}) = 0, \quad (6)$$

as it was done, for example, by Chandrasekhar (1983) to solve similar problems.

Introducing the notation  $\xi^2 = l$ ,  $Q^2 = q$ , we obtain

$$R(r) = r^4 - lr^2 + 2lr - qr. \quad (7)$$

The discriminant  $\Delta$  of the polynomial  $R(r)$  has the form (as it was shown by Zakharov (1991a,b, 1994a)):

$$\Delta = 16l^3[l^2(1 - q) + l(-8q^2 + 36q - 27) - 16q^3]. \quad (8)$$

The polynomial  $R(r)$  thus has a multiple root if and only if

$$l^3[l^2(1 - q) + l(-8q^2 + 36q - 27) - 16q^3] = 0. \quad (9)$$

Excluding the case  $l = 0$ , which corresponds to a multiple root at  $r = 0$ , we find that the polynomial  $R(r)$  has a multiple root for  $r \geq r_+$  if and only if

$$l^2(1 - q) + l(-8q^2 + 36q - 27) - 16q^3 = 0. \quad (10)$$

If  $q = 0$ , we obtain the well-known result for a Schwarzschild black hole (Misner, Thorne and Wheeler 1973; Wald 1984; Lightman et al. 1975),  $l = 27$ , or  $L_{cr} = 3\sqrt{3}$ . If  $q = 1$ , then  $l = 16$ , or  $L_{cr} = 4$ , which also corresponds to numerical results given by Young (1976).

The photon capture cross section for an extreme charged black hole turns out to be considerably smaller than the capture cross section of a Schwarzschild black hole. The critical value of the impact parameter, characterizing the capture cross section for a Reissner - Nordström black hole, is determined by the equation (Zakharov 1991a,b, 1994a)

$$l = \frac{(8q^2 - 36q + 27) + \sqrt{(8q^2 - 36q + 27)^2 + 64q^3(1 - q)}}{2(1 - q)}. \quad (11)$$

# A.F. Zakharov & F. De Paolis, A.A. Nucita, G.Ingrosso, **Astron. & Astrophys.**, **442, 795 (2005)**

As it was explained by Zakharov et al. (2005a,b) this leads to the formation of shadows described by the critical value of  $L_{cr}$  or, in other words, in the spherically symmetric case, shadows are circles with radii  $L_{cr}$ . Therefore, measuring the shadow size, one could evaluate the black hole charge in black hole mass units  $M$ .

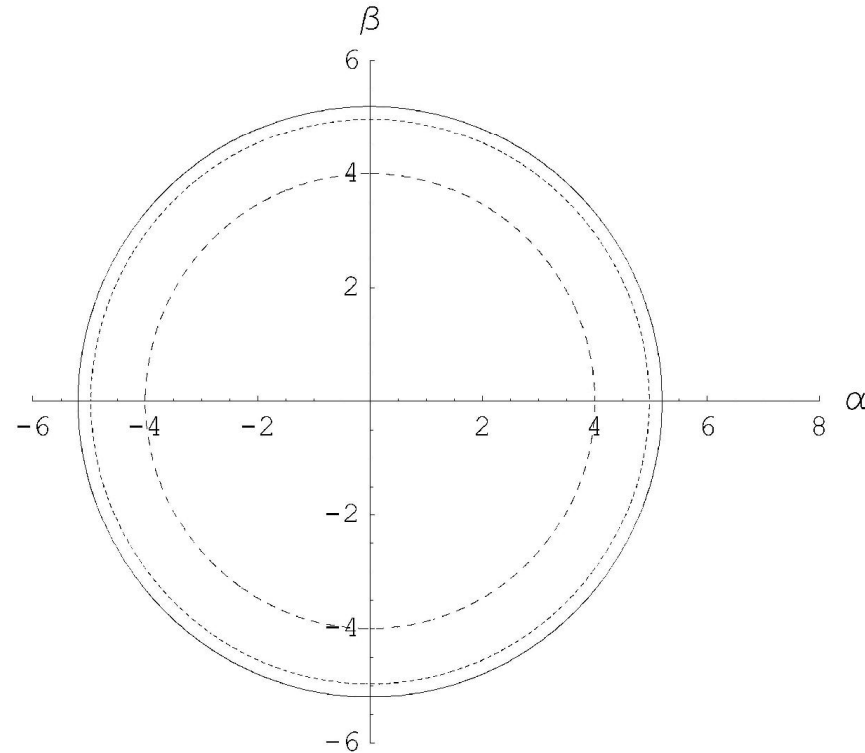


**Fig. 1.** Shadow (mirage) sizes are shown for selected charges of black holes  $Q = 0$  (solid line),  $Q = 0.5$  (short dashed line) and  $Q = 1$  (long dashed line).

Jourdain: “For more than forty years I have been speaking prose while knowing nothing of it,” (from “*Bourgeois Gentleman* or *The Middle-Class Aristocrat* “, J. B. Moliere)

We: “For many years we had speaking about BH’s in Randall --- Sundrum model or in (beyond) Horndesky theory while knowing nothing of the theories...”

## Constraints on a charge in the Reissner-Nordström metric for the black hole at the Galactic Center

Alexander F. Zakharov\*

North Carolina Central University, Durham, North Carolina 27707, USA; Institute of Theoretical and Experimental Physics, Moscow 117218, Russia; Joint Institute for Nuclear Research, Dubna 141980, Russia; Institute for Computer Aided Design of RAS, 123056 Moscow, Russia; and National Research Nuclear University (NRNU MEPhI), 115409 Moscow, Russia  
(Received 5 March 2013; published 9 September 2014)

Using an algebraic condition of vanishing discriminant for multiple roots of fourth-degree polynomials, we derive an analytical expression of a shadow size as a function of a charge in the Reissner-Nordström (RN) metric [1,2]. We consider shadows for negative tidal charges and charges corresponding to naked singularities  $q = Q^2/M^2 > 1$ , where  $Q$  and  $M$  are black hole charge and mass, respectively, with the derived expression. An introduction of a negative tidal charge  $q$  can describe black hole solutions in theories with extra dimensions, so following the approach we consider an opportunity to extend the RN metric to negative  $Q^2$ , while for the standard RN metric  $Q^2$  is always non-negative. We found that for  $q > 9/8$ , black hole shadows disappear. Significant tidal charges  $q = -6.4$  (suggested by Bin-Nun [3–5]) are not consistent with observations of a minimal spot size at the Galactic Center observed in mm-band; moreover, these observations demonstrate that a Reissner-Nordström black hole with a significant charge  $q \approx 1$  provides a better fit of recent observational data for the black hole at the Galactic Center in comparison with the Schwarzschild black hole.

DOI: 10.1103/PhysRevD.90.062007

PACS numbers: 04.80.Cc, 04.20.-q, 04.50.Gh, 04.70.Bw

### I. INTRODUCTION

Soon after the discovery of general relativity (GR), the first solutions corresponding to spherical symmetric black holes were found [1,2,6]; however, initially people were rather sceptical about possible astronomical applications of the solutions corresponding to black holes [7] (see also, for instance, one of the first textbooks on GR [8]). Even after an introduction to the black hole concept by Wheeler [9] (he used the term in his public lecture in 1967 [10]), we did not know too many examples where we really need GR models with strong gravitational fields that arise near black hole horizons to explain observational data. The cases where we need strong field approximation are very important since they give an opportunity to check GR predictions in a strong field limit; therefore, one could significantly constrain alternative theories of gravity.

One of the most important options to test gravity in the strong field approximation is analysis of relativistic line shape as it was shown in [11], with assumptions that a line emission is originated at a circular ring area of a flat accretion disk. Later on, such signatures of the Fe  $K\alpha$  line have been found in the active galaxy MCG-6-30-15 [12]. Analyzing the spectral line shape, the authors concluded the emission region is so close to the black hole horizon that one has to use Kerr metric approximation [13] to fit observational data [12]. Results of simulations of iron  $K\alpha$  line formation are given in [14,15] (where we used our

approach [16]); see also [17] for a more recent review of the subject.

Now there are two basic observational techniques to investigate a gravitational potential at the Galactic Center, namely, (a) monitoring the orbits of bright stars near the Galactic Center to reconstruct a gravitational potential [18] (see also a discussion about an opportunity to evaluate black hole dark matter parameters in [19] and an opportunity to constrain some class of an alternative theory of gravity [20]) and (b) measuring in mm band, with VLBI technique, the size and shape of shadows around the black hole, giving an alternative possibility to evaluate black hole parameters. The formation of retro-lensing images (also known as mirages, shadows, or “faces” in the literature) due to the strong gravitational field effects nearby black holes has been investigated by several authors [21–24].

Theories with extra dimensions admit astrophysical objects (supermassive black holes in particular) which are rather different from standard ones. Tests have been proposed when it would be possible to discover signatures of extra dimensions in supermassive black holes since the gravitational field may be different from the standard one in the GR approach. So, gravitational lensing features are different for alternative gravity theories with extra dimensions and general relativity.

Recently, Bin-Nun [3–5] discussed the possibility that the black hole at the Galactic Center is described by the tidal Reissner-Nordström metric which may be admitted by the Randall-Sundrum II braneworld scenario [25]. Bin-Nun suggested an opportunity of evaluating the black hole

\*zakharov@itep.ru

$$\text{Dis}(s_1, s_2, s_3, s_4) = \begin{vmatrix} 1 & 1 & 1 & 1 \\ X_1 & X_2 & X_3 & X_4 \\ X_1^2 & X_2^2 & X_3^2 & X_4^2 \\ X_1^3 & X_2^3 & X_3^3 & X_4^3 \end{vmatrix} = \begin{vmatrix} 4 & p_1 & p_2 & p_3 \\ p_1 & p_2 & p_3 & p_4 \\ p_2 & p_3 & p_4 & p_5 \\ p_3 & p_4 & p_5 & p_6 \end{vmatrix}. \quad (20)$$

Expressing the polynomials  $p_k$  ( $1 \leq k \leq 6$ ) in terms of the polynomials  $s_k$  ( $1 \leq k \leq 4$ ) and using Newton's equations

$$\text{Dis}(s_1, s_2, s_3, s_4) = \begin{vmatrix} 4 & 0 & 2l & -6l \\ 0 & 2l & -6l & 2l(l+2q) \\ 2l & -6l & 2l(l+2q) & -10l^2 \\ -6l & 2l(l+2q) & -10l^2 & 2l^2(l+6+3q) \end{vmatrix} = 16l^3[l^2(1-q) + l(-8q^2 + 36q - 27) - 16q^3]. \quad (22)$$

The polynomial  $R(r)$  thus has a multiple root if and only if

$$l^3[l^2(1-q) + l(-8q^2 + 36q - 27) - 16q^3] = 0. \quad (23)$$

Excluding the case  $l = 0$ , which corresponds to a multiple root at  $r = 0$ , we find that the polynomial  $R(r)$  has a multiple root for  $r \geq r_+$  if and only if

$$l^2(1-q) + l(-8q^2 + 36q - 27) - 16q^3 = 0. \quad (24)$$

If  $q = 0$ , we obtain the well-known result for a Schwarzschild black hole [38,39,49],  $l_{\text{cr}} = 27$ , or  $\xi_{\text{cr}} = 3\sqrt{3}$  [where  $l_{\text{cr}}$  is the positive root of Eq. (24)]. If  $q = 1$ , then  $l = 16$ , or  $\xi_{\text{cr}} = 4$ , which also corresponds to numerical results given in paper [50]. The photon capture cross section for an extreme charged black hole turns out to be considerably smaller than the capture cross section of a Schwarzschild black hole. The critical value of the impact parameter, characterizing the capture cross section for a RN black hole, is determined by the equation

$$l_{\text{cr}} = \frac{(8q^2 - 36q + 27) + \sqrt{D_1}}{2(1-q)}, \quad (25)$$

where  $D_1 = (8q^2 - 36q + 27)^2 + 64q^3(1-q) = -512(q - \frac{9}{8})^3$ . It is clear from the last relation that there are circular unstable photon orbits only for  $q \leq \frac{9}{8}$  (see also results in [37] about the same critical value). Substituting Eq. (25) into the expression for the coefficients of the polynomial  $R(r)$  it is easy to calculate the radius of the unstable circular photon orbit (which is the same as the minimum periastron

we calculate the polynomials and discriminant of the family  $X_1, X_2, X_3, X_4$  in roots of the polynomial  $R(r)$ ; we obtain

$$\begin{aligned} p_1 &= s_1 = 0, & p_2 &= -2s_2, & p_3 &= 3s_3, \\ p_4 &= 2s_2^2 - 4s_4, & p_5 &= -5s_3s_2, \\ p_6 &= -2s_2^3 + 3s_3^2 + 6s_4s_2, \end{aligned} \quad (21)$$

where  $s_1 = 0, s_2 = -l, s_3 = -2l, s_4 = -ql$ , corresponding to the polynomial  $R(r)$  in Eq. (8). The discriminant  $\text{Dis}$  of the polynomial  $R(r)$  has the form

distance). The orbit of a photon moving from infinity with the critical impact parameter, determined in accordance with Eq. (25) spirals into circular orbit. To find a radius of photon unstable orbit we will solve Eq. (7) substituting  $l_{\text{cr}}$  in the relation. From trigonometric formula for roots of cubic equation we have

$$r_{\text{crit}} = 2\sqrt{\frac{l_{\text{cr}}}{6}} \cos \frac{\alpha}{3}, \quad (26)$$

where

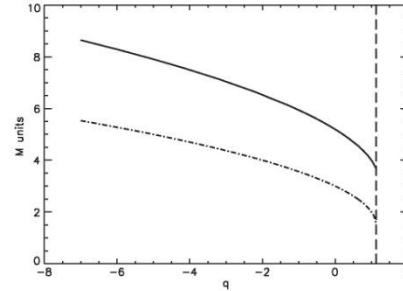


FIG. 1. Shadow (mirage) radius (solid line) and radius of the last circular unstable photon orbit (dot-dashed line) in  $M$  units as a function of  $q$ . The critical value  $q = 9/8$  is shown with dashed vertical line.

Unstable photon orbits but not shadows could exist for naked singularities with  $1 < Q^2 < 9/8$  , while in paper arxiv:1802.08060[astro-ph.HE], the authors presented an example of naked singularities with a shadows.



Contents lists available at SciVerse ScienceDirect

New Astronomy Reviews

journal homepage: [www.elsevier.com/locate/newastrev](http://www.elsevier.com/locate/newastrev)

## Shadows as a tool to evaluate black hole parameters and a dimension of spacetime

Alexander F. Zakharov<sup>a,b,\*</sup>, Francesco De Paolis<sup>c</sup>, Gabriele Ingrosso<sup>c</sup>, Achille A. Nucita<sup>c</sup><sup>a</sup>Institute of Theoretical and Experimental Physics, 25, B. Chermushkinskaya St., Moscow 117259, Russia<sup>b</sup>Bogoliubov Laboratory of Theoretical Physics, Joint Institute for Nuclear Research, Dubna, Russia<sup>c</sup>Dipartimento di Fisica Università di Salento and INFN, Sezione di Lecce, Italy

## ARTICLE INFO

Article history:  
Available online xxxxx

## ABSTRACT

Shadow formation around supermassive black holes were simulated. Due to enormous progress in observational facilities and techniques of data analysis researchers approach to opportunity to measure shapes and sizes of the shadows at least for the closest supermassive black hole at the Galactic Center. Measurements of the shadow sizes around the black holes can help to evaluate parameters of black hole metric. Theories with extra dimensions (Randall–Sundrum II braneworld approach, for instance) admit astrophysical objects (supermassive black holes, in particular) which are rather different from standard ones. Different tests were proposed to discover signatures of extra dimensions in supermassive black holes since the gravitational field may be different from the standard one in the general relativity (GR) approach. In particular, gravitational lensing features are different for alternative gravity theories with extra dimensions and general relativity. Therefore, there is an opportunity to find signatures of extra dimensions in supermassive black holes. We show how measurements of the shadow sizes can put constraints on parameters of black hole in spacetime with extra dimensions.

© 2011 Elsevier B.V. All rights reserved.

## Contents

1. Introduction	00
2. Shadows for Kerr black holes	00
2.1. Mirage shapes	00
2.2. Equatorial plane observer case	00
2.3. Polar axis observer case	00
2.4. General case for the angular position of the observer	00
3. Shadows for Reissner–Nordström black holes	00
3.1. Basic definitions and equations	00
3.2. Capture cross section of photons by a Reissner–Nordström black hole	00
3.3. Shadows for a Reissner–Nordström black holes with a tidal charge	00
4. The space RadioAstron interferometer	00
5. Searches for mirages near Sgr A* with RadioAstron	00
6. Discussion	00
7. Conclusions	00
Acknowledgements	00
References	00

## 1. Introduction

There are not too many observational signatures of black holes where we actually need a strong gravitational field approximation to explain observational data. For many years bright examples

\* Corresponding author at: Institute of Theoretical and Experimental Physics, 25, B. Chermushkinskaya St., Moscow 117259, Russia.  
E-mail address: [zakharov@itep.ru](mailto:zakharov@itep.ru) (A.F. Zakharov).

Some time ago Bin-Nun (2010) discussed an opportunity that the black hole at the Galactic Center is described by the tidal Reissner--Nordstrom metric which may be admitted by the Randall--Sundrum II braneworld scenario. Bin-Nun suggested an opportunity of evaluating the black hole metric analyzing (retro-)lensing of bright stars around the black hole in the Galactic Center. Doeleman et al. (2008) evaluated a shadow size for the black hole at the Galactic Center. Measurements of the shadow size around the black hole may help to evaluate parameters of black hole metric Zakharov et al (2005). We derive an analytic expression for the black hole shadow size as a function of charge for the tidal Reissner--Nordstrom metric. We conclude that observational data concerning shadow size measurements are not consistent with significant negative charges, in particular, the significant negative charge  $Q/(4M^2)=-1.6$  (discussed by Bin-Nun (2010) is practically ruled out with a very probability (the charge is roughly speaking is beyond  $9 \sigma$  confidence level, but a negative charge is beyond  $3 \sigma$  confidence level).

## LETTERS

## Event-horizon-scale structure in the supermassive black hole candidate at the Galactic Centre

Sheperd S. Doeleman<sup>1</sup>, Jonathan Weintroub<sup>2</sup>, Alan E. E. Rogers<sup>1</sup>, Richard Plambeck<sup>3</sup>, Robert Freund<sup>4</sup>, Remo P. J. Tilanus<sup>5,6</sup>, Per Friberg<sup>5</sup>, Lucy M. Ziurys<sup>4</sup>, James M. Moran<sup>2</sup>, Brian Corey<sup>1</sup>, Ken H. Young<sup>2</sup>, Daniel L. Smythe<sup>1</sup>, Michael Titus<sup>1</sup>, Daniel P. Marrone<sup>7,8</sup>, Roger J. Cappallo<sup>1</sup>, Douglas C.-J. Bock<sup>9</sup>, Geoffrey C. Bower<sup>3</sup>, Richard Chamberlin<sup>10</sup>, Gary R. Davis<sup>5</sup>, Thomas P. Krichbaum<sup>11</sup>, James Lamb<sup>12</sup>, Holly Maness<sup>3</sup>, Arthur E. Niell<sup>1</sup>, Alan Roy<sup>11</sup>, Peter Strittmatter<sup>4</sup>, Daniel Werthimer<sup>13</sup>, Alan R. Whitney<sup>1</sup> & David Woody<sup>12</sup>

The cores of most galaxies are thought to harbour supermassive black holes, which power galactic nuclei by converting the gravitational energy of accreting matter into radiation<sup>1</sup>. Sagittarius A\* (Sgr A\*), the compact source of radio, infrared and X-ray emission at the centre of the Milky Way, is the closest example of this phenomenon, with an estimated black hole mass that is 4,000,000 times that of the Sun<sup>2,3</sup>. A long-standing astronomical goal is to resolve structures in the innermost accretion flow surrounding Sgr A\*, where strong gravitational fields will distort the appearance of radiation emitted near the black hole. Radio observations at wavelengths of 3.5 mm and 7 mm have detected intrinsic structure in Sgr A\*, but the spatial resolution of observations at these wavelengths is limited by interstellar scattering<sup>4–7</sup>. Here we report observations at a wavelength of 1.3 mm that set a size of  $37^{+16}_{-10}$  microarcseconds on the intrinsic diameter of Sgr A\*. This is less than the expected apparent size of the event horizon of the presumed black hole, suggesting that the bulk of Sgr A\* emission may not be centred on the black hole, but arises in the surrounding accretion flow.

The proximity of Sgr A\* makes the characteristic angular size scale of the Schwarzschild radius ( $R_{\text{Sch}} = 2GM/c^2$ ) larger than for any other black hole candidate. At a distance of  $\sim 8$  kpc (ref. 8), the Sgr A\* Schwarzschild radius is 10  $\mu\text{as}$ , or 0.1 astronomical unit (AU). Multi-wavelength monitoring campaigns<sup>9–11</sup> indicate that activity on scales of a few  $R_{\text{Sch}}$  in Sgr A\* is responsible for observed short-term variability and flaring from radio to X-rays, but direct observations of structure on these scales by any astronomical technique has not been possible. Very-long-baseline interferometry (VLBI) at 7 mm and 3.5 mm wavelength shows the intrinsic size of Sgr A\* to have a wavelength dependence, which yields an extrapolated size at 1.3 mm of 20–40  $\mu\text{as}$  (refs 6, 7). VLBI images at wavelengths longer than 1.3 mm, however, are dominated by interstellar scattering effects that broaden images of Sgr A\*. Our group has been working to extend VLBI arrays to 1.3 mm wavelength, to reduce the effects of interstellar scattering, and to utilize long baselines to increase angular resolution with a goal of studying the structure of Sgr A\* on scales commensurate with the putative event horizon of the black hole. Previous pioneering VLBI work at 1.4 mm wavelength

uncertainties resulted in a range for the derived size of 50–170  $\mu\text{as}$  (ref. 12).

On 10 and 11 April 2007, we observed Sgr A\* at 1.3 mm wavelength with a three-station VLBI array consisting of the Arizona Radio Observatory 10-m Submillimetre Telescope (ARO/SMT) on Mount Graham in Arizona, one 10-m element of the Combined Array for Research in Millimeter-wave Astronomy (CARMA) in Eastern California, and the 15-m James Clerk Maxwell Telescope (JCMT) near the summit of Mauna Kea in Hawaii. A hydrogen maser time standard and high-speed VLBI recording system were installed at both the ARO/SMT and CARMA sites to support the observation. The JCMT partnered with the Submillimetre Array (SMA) on Mauna Kea, which housed the maser and the VLBI recording system and provided a maser-locked receiver reference to the JCMT. Two 480-MHz passbands sampled to two-bit precision were recorded at each site, an aggregate recording rate of  $3.84 \times 10^9$  bits per second ( $\text{Gbit s}^{-1}$ ). Standard VLBI practice is to search for detections over a range of interferometer delay and delay rate. Six bright quasars were detected with high signal to noise on all three baselines allowing array geometry, instrumental delays and frequency offsets to be accurately calibrated. This calibration greatly reduced the search space for detections of Sgr A\*. All data were processed on the Mark4 correlator at the MIT Haystack Observatory in Massachusetts.

On both 10 and 11 April 2007, Sgr A\* was robustly detected on the short ARO/SMT–CARMA baseline and the long ARO/SMT–JCMT baseline. On neither day was Sgr A\* detected on the CARMA–JCMT baseline, which is attributable to the sensitivity of the CARMA station being about a third that of the ARO/SMT (owing to weather, receiver temperature and aperture efficiency). Table 1 lists the Sgr A\* detections on the ARO/SMT–JCMT baseline. The high signal to noise ratio, coupled with the tight grouping of residual delays and delay rates, makes the detections robust and unambiguous.

There are too few visibility measurements to form an image by the usual Fourier transform techniques; hence, we fit models to the visibilities (shown in Fig. 1). We first modelled Sgr A\* as a circular Gaussian brightness distribution, for which one expects a Gaussian relationship between correlated flux density and projected baseline length. The weighted least-squares best-fit model (Fig. 1) corre-

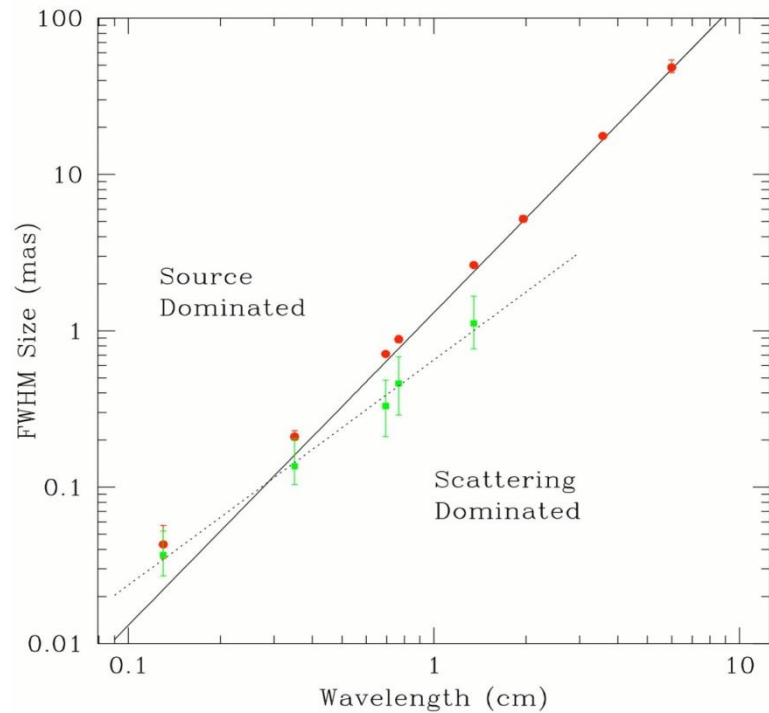


**Fig 2**

**Figure 2 Observed and intrinsic size of Sgr A\* as a function of wavelength.** Red circles show major-axis observed sizes of Sgr A\* from VLBI observations (all errors  $3\sigma$ ). Data from wavelengths of 6 cm to 7 mm are from ref. 13, data at 3.5 mm are from ref. 7, and data at 1.3 mm are from the observations reported here. The solid line is the best-fit  $\lambda^2$  scattering law from ref. 13, and is derived from measurements made at  $\lambda > 17$  cm. Below this line, measurements of the intrinsic size of Sgr A\* are dominated by scattering effects, while measurements that fall above the line indicate intrinsic structures that are larger than the scattering size (a ‘source-dominated’ regime). Green points show derived major-axis intrinsic sizes from  $2 \text{ cm} < \lambda < 1.3 \text{ mm}$  and are fitted with a  $\lambda^\alpha$  power law ( $\alpha = 1.44 \pm 0.07$ ,  $1\sigma$ ) shown as a dotted line. When the 1.3-mm point is removed from the fit, the power-law exponent becomes  $\alpha = 1.56 \pm 0.11$  ( $1\sigma$ ).

# RADIO INTERFEROMETER MUCH LARGER THE EARTH

## "SPECTR-R" (Mission "RadioAstron")

Main scientific tasks of the mission -

syntheses of high-precision images of various Universe objects, its coordinates measurements and search their variability with the time. A fringe width of the system is up to 7 micro arc seconds.

Main characteristics of the space radio telescope

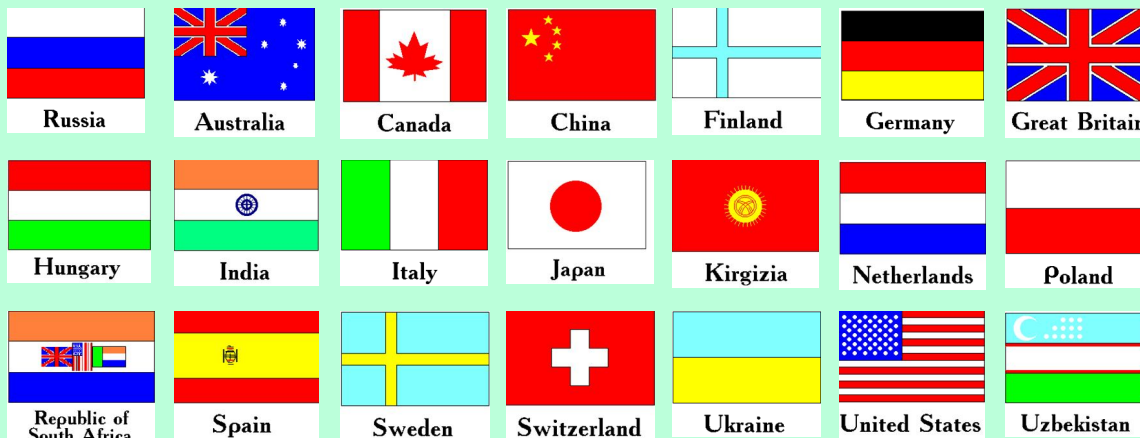
Spectral band:

- wavelength (cm) - 92; 18; 6.2; 1.19-1.63
- frequency (GHz) - 0.327; 1.66; 4.83; 18-26

Main organizations:

on scientific complex - Astro Space Center of Lebedev Physical Institute of Russian Academy of Science;

of spacecraft - Lavochkin Research Production Association of Russian Space Agency.

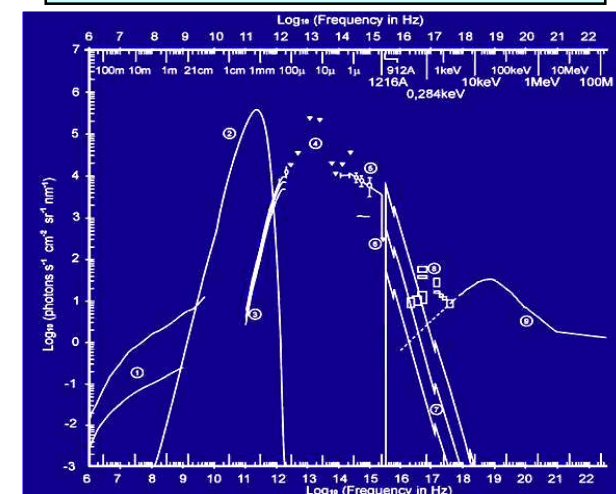


Planned launch date of the mission is **2007**.



The orbit of the mission :

- apogee - 310 000 - 370 000 km
- perigee - 10 000 - 70 000 km
- declination - 51.6°
- period variation - 7 - 10 days
- Guaranteed time of activity - 5 years
- Scientific payload mass - 2100 kg
- Pointing accuracy of radio telescope - 35"



- **ERC Synergy Grant to image event horizon of black hole**
- **Was Einstein right? The European Research Council (ERC) has awarded 14 Million Euros to a team of European astrophysicists to construct the first accurate image of a black hole. The team will test the predictions of current theories of gravity, including Einstein's theory of General Relativity. The funding is provided in the form of a 'Synergy Grant', the largest and most competitive type of grant of the ERC.**

Synergy grants are awarded by the ERC, on the basis of scientific excellence in an intricate and highly competitive selection procedure. The grants have a maximum limit of 15 Million Euros and require the collaboration of 2-4 principal investigators. In the current selection round the ERC honoured 13 out of 449 funding proposal, which corresponds to a success rate of less than 3%. Proposals were submitted from all areas of European science. This is the first time an astrophysics proposal has been awarded.

### **Black holes**

Black holes are notoriously elusive with a gravitational field so large that even light cannot escape their grip. The team plans to make an image of the event horizon – the border around a black hole which light can enter, but not leave.

“While most astrophysicists believe black holes exists, nobody has actually ever seen one”, says Heino Falcke, Professor in radio astronomy at Radboud University in Nijmegen and ASTRON, The Netherlands. “The technology is now advanced enough that we can actually image black holes and check if they truly exist as predicted: If there is no event horizon, there are no black holes”.

### **Measure the tiniest shadow**

So, if black holes are black and are hard to catch on camera, where should one look? The scientists want to peer into the heart of our own Galaxy, which hosts a mysterious radio source, called Sagittarius A\*. The object is known to have a mass of around 4 million times the mass of the Sun and is considered to be the central supermassive black hole of the Milky Way.

As gaseous matter is attracted towards the event horizon by the black hole's gravitational attraction, strong radio emission is produced before the gas disappears. The event horizon should then cast a dark shadow on that bright emission. Given the huge distance to the centre of the Milky Way, the size of the shadow is equivalent to an apple on the moon seen from the earth.

However, by combining high-frequency radio telescopes around the world, in a technique called very long baseline interferometry, or VLBI, even such a tiny feature is in principle detectable. Falcke first proposed this experiment 15 years ago and now an international effort is forming to build a global “Event Horizon Telescope” to realize it. Falcke is convinced: “With this grant from the ERC and the excellent expertise in Europe, we will be able to make it happen together with our international partners”.

•

- *The BlackHoleCam network*

### **Find more radio pulsars**

In addition, the group wants to use the same radio telescopes to find and measure pulsars around the very same black hole. Pulsars are rapidly spinning neutron stars, which can be used as highly accurate natural clocks in space.

“A pulsar around a black hole would be extremely valuable”, explains Michael Kramer, managing director of the Max-Planck-Institut für Radioastronomie in Bonn. “They allow us to determine the deformation of space and time caused by black holes and measure their properties with unprecedented precision”.

However, while radio pulsars are ubiquitous in our Milky Way, surprisingly none had been found in the centre of the Milky Way for decades. Only recently Kramer and his team found the very first radio pulsar around Sagittarius A\*. “We suspect there are many more radio pulsars, and if they are there we will find them”, says Kramer.

### **Behaviour of light and matter**

But how will scientists be really sure that there is a black hole in our Milky Way and not something else that behaves in a very similar way? To answer this question, the scientists will combine the information from the black hole shadow and from the motion of pulsars and stars around Sagittarius A\* with detailed computer simulations of the behaviour of light and matter around black holes as predicted by theory.

We have made enormous progress in computational astrophysics in recent years”, states Luciano Rezzolla, Professor of theoretical astrophysics at the Goethe University in Frankfurt and leader of the gravitational-wave modelling group at the Max-Planck-Institut für Gravitationsphysik in Potsdam.

“We can now calculate very precisely how space and time are warped by the immense gravitational fields of a black hole, and determine how light and matter propagate around black holes”, he remarks. “Einstein’s theory of General Relativity is the best theory of gravity we know, but it is not the only one. We will use these observations to find out if black holes, one of the most cherished astrophysical objects, exist or not. Finally, we have the opportunity to test gravity in a regime that until recently belonged to the realm of science fiction; it will be a turning point in modern science”, says Rezzolla.

### **Partners in Europe**

The principal investigators will closely collaborate with a number of groups throughout Europe. Team members in the ERC grant are:

- Robert Laing from the European Southern Observatory (ESO) in Garching, European project scientist of ALMA, a new high-frequency radio telescope, that the team seeks to use for their purpose,
- Frank Eisenhauer from the Max-Planck-Institut für extraterrestrische Physik in Garching, principal investigator of the upcoming GRAVITY instrument for the ESO Very Large Telescope Interferometer, to precisely measure the motion of stars and infrared flares around the Galactic Centre black hole.
- Huib van Langevelde, director of the Joint Institute for VLBI in Europe (JIVE) and Professor of Galactic radio astronomy at the University of Leiden.

- The efforts of the Max-Planck-Institut für Radioastronomie will be conducted jointly with the VLBI group and the high-frequency radio astronomy groups at the institute and their directors Anton Zensus and Karl Menten.

The scientists also want to make use of the two major European millimeter radio observatories (NOEMA and the IRAM 30m telescope) operated by IRAM, a joint German/French/Spanish radio astronomy institute.

The BlackHoleCam team will closely collaborate with the Event Horizon Telescope project, led by S. Doeleman (MIT Haystack Observatory, Boston

- The team led by three principal investigators (Heino Falcke, Radboud University Nijmegen and ASTRON, Michael Kramer, Max-Planck-Institut für Radioastronomie, and Luciano Rezzolla, Goethe University in Frankfurt and Max-Planck-Institut für Gravitationsphysik) will combine several telescopes around the globe to peer into the heart of our own Galaxy, which hosts a mysterious radio source, called Sagittarius A\*. It is considered to be the central super massive black hole.

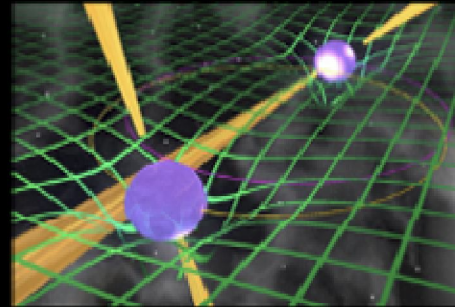
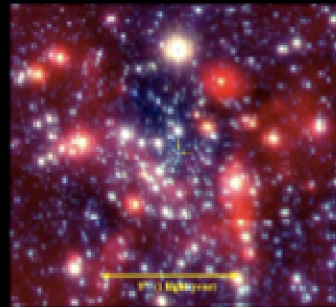
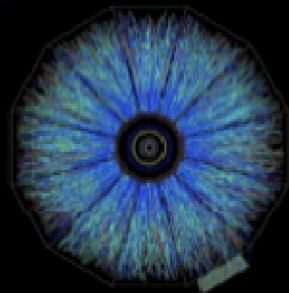
- H. Falcke, S. Markoff, Toward the event horizon—the supermassive black hole in the Galactic Center, *Classical and Quantum Gravity*, 30, Issue 24, 244003 (2013)
- The review has quoted two our papers

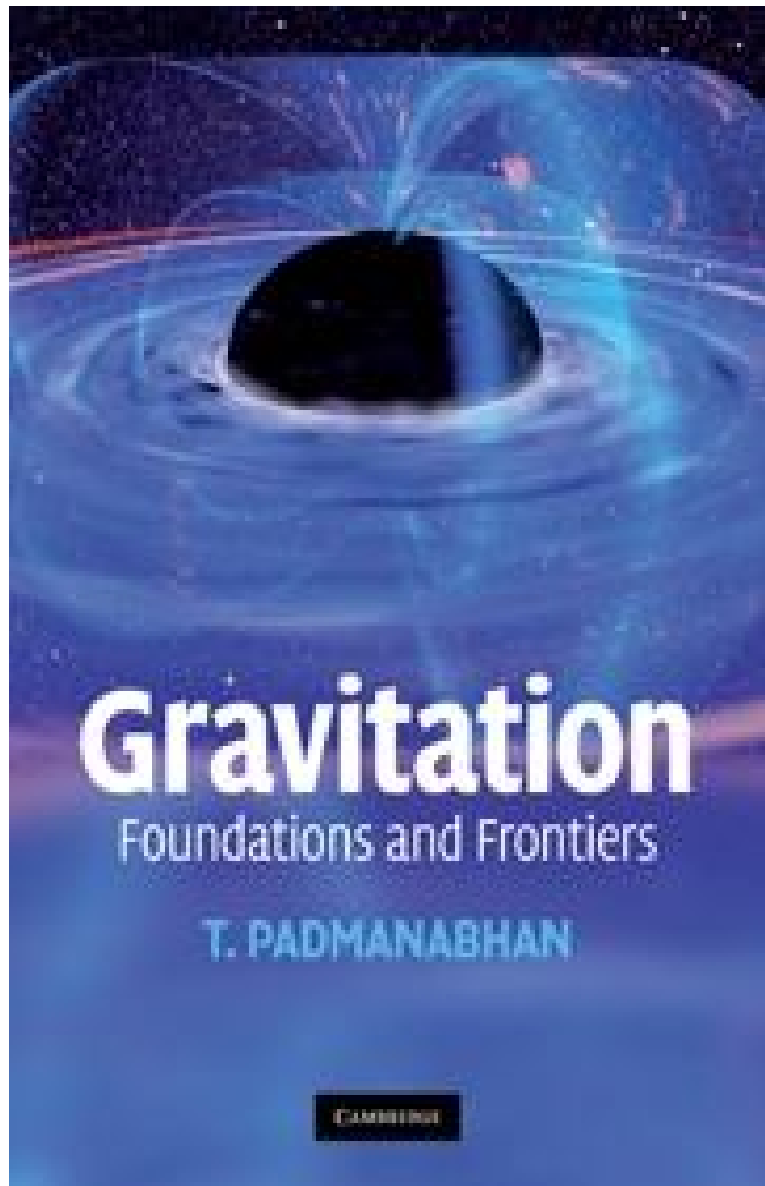




FIAS Frankfurt Institute  
for Advanced Studies

## Karl Schwarzschild Meeting 2015





# Gravitation

Foundations and Frontiers

T. PADMANABHAN

CAMBRIDGE

## An ultraluminous quasar with a twelve-billion-solar-mass black hole at redshift 6.30

Xue-Bing Wu<sup>1,2</sup>, Feige Wang<sup>1,2</sup>, Xiaohui Fan<sup>2,3</sup>, Weimin Yi<sup>4,5,6</sup>, Wenwen Zuo<sup>7</sup>, Fuyan Bian<sup>8</sup>, Linhua Jiang<sup>2</sup>, Ian D. McGreer<sup>3</sup>, Ran Wang<sup>2</sup>, Jinyi Yang<sup>1,2</sup>, Qian Yang<sup>1,2</sup>, David Thompson<sup>9</sup> & Yuri Beletsky<sup>10</sup>

So far, roughly 40 quasars with redshifts greater than  $z = 6$  have been discovered<sup>1–8</sup>. Each quasar contains a black hole with a mass of about one billion solar masses ( $10^9 M_{\odot}$ )<sup>2,6,7,9–13</sup>. The existence of such black holes when the Universe was less than one billion years old presents substantial challenges to theories of the formation and growth of black holes and the coevolution of black holes and galaxies<sup>14</sup>. Here we report the discovery of an ultraluminous quasar, SDSS J010013.02+280225.8, at redshift  $z = 6.30$ . It has an optical and near-infrared luminosity a few times greater than those of previously known  $z > 6$  quasars. On the basis of the deep absorption trough<sup>15</sup> on the blue side of the Lyman- $\alpha$  emission line in the spectrum, we estimate the proper size of the ionized proximity zone associated with the quasar to be about 26 million light years, larger than found with other  $z > 6.1$  quasars with lower luminosities<sup>16</sup>. We estimate (on the basis of a near-infrared spectrum) that the black hole has a mass of  $\sim 1.2 \times 10^{10} M_{\odot}$ , which is consistent with the  $1.3 \times 10^{10} M_{\odot}$  derived by assuming an Eddington-limited accretion rate.

High-redshift quasars have been efficiently selected using a combination of optical and near-infrared colours<sup>3,4</sup>. We have carried out a systematic survey of quasars at  $z > 5$  using photometry from the Sloan Digital Sky Survey (SDSS)<sup>17</sup>, the two Micron All Sky Survey (2MASS)<sup>18</sup> and the Wide-field Infrared Survey Explorer (WISE)<sup>19</sup>, resulting in the discovery of a significant population of luminous high-redshift quasars. SDSS J010013.02+280225.8 (hereafter J0100+2802) was selected as a high-redshift quasar candidate owing to its red optical colour (with SDSS AB magnitudes  $i_{AB} = 20.84 \pm 0.06$  and  $z_{AB} = 18.33 \pm 0.03$ ) and a photometric redshift of  $z \approx 6.3$ . It has bright detections in the 2MASS J, H and K<sub>s</sub> bands with Vega magnitudes of  $17.00 \pm 0.20$ ,  $15.98 \pm 0.19$  and  $15.20 \pm 0.16$ , respectively; it is also strongly detected in WISE, with Vega magnitudes in W1 to W4 bands of  $14.45 \pm 0.03$ ,  $13.63 \pm 0.03$ ,  $11.71 \pm 0.21$  and  $8.98 \pm 0.44$ , respectively (see Extended Data Figs 1 and 2 for images in different bands). Its colour in the two bluest WISE bands, W1 and W2, clearly differentiates it from the bulk of stars in our Galaxy<sup>20</sup>. The object was within the SDSS-III imaging area. It is close to the colour selection boundary of SDSS  $z \approx 6$  quasars<sup>1</sup>, but was assigned to low priority earlier because of its relatively red  $z_{AB} - J$  colour and its bright apparent magnitudes. It is undetected in both radio and X-ray bands by the wide-area, shallow survey instruments.

Initial optical spectroscopy on J0100+2802 was carried out on 29 December 2013 with the Lijiang 2.4-m telescope in China. The low-resolution spectrum clearly shows a sharp break at about 8,900 Å, con-

We use the multiwavelength photometry to estimate the optical luminosity at rest-frame wavelength 3,000 Å ( $L_{3,000}$ ), which is consistent with that obtained from K-band spectroscopy (see below). The latter gives a more reliable value of  $(3.15 \pm 0.47) \times 10^{47}$  erg s<sup>-1</sup>, adopting a  $\Lambda$ CDM cosmology with Hubble constant  $H_0 = 70$  km s<sup>-1</sup> Mpc<sup>-1</sup>, matter density parameter  $\Omega_M = 0.30$  and dark energy density parameter  $\Omega_{\Lambda} = 0.7$ . Assuming an empirical conversion factor from the luminosity at 3,000 Å to the bolometric luminosity<sup>21</sup>, this gives  $L_{bol} = 5.15 \times L_{3,000} = 1.62 \times 10^{48}$  erg s<sup>-1</sup> =  $4.29 \times 10^{14} L_{\odot}$  (where  $L_{\odot}$  is the solar luminosity). We obtain a similar result when estimating the bolometric luminosity from the Galactic extinction corrected absolute magnitude at rest-frame 1,450 Å, which is  $M_{1,450,AB} = -29.26 \pm 0.20$ . The luminosity of this

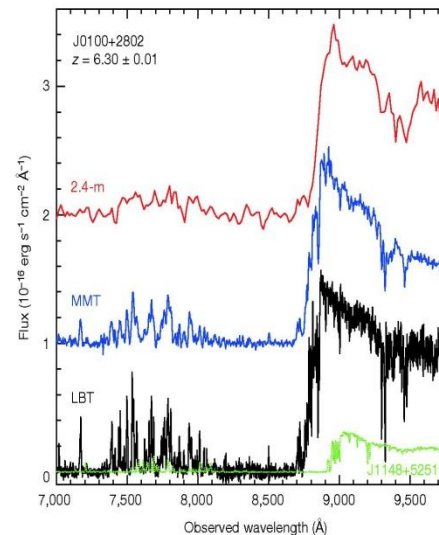


**Figure 1** | The optical spectra of J0100+2802. From top to bottom, spectra taken with the Lijiang 2.4-m telescope, the MMT and the LBT (in red, blue and black colours), respectively. For clarity, two spectra are offset upward by

NATURE | NEWS

## Young black hole had monstrous growth spurt

Super-massive object found in early Universe tests theories of cosmic evolution.

Davide Castelvecchi

25 February 2015



Print

Zhaoyu Li/SHAO

An artist's impression of a quasar with a supermassive black hole at its heart in the distant Universe.

A black hole that grew to gargantuan size in the Universe's first billion years is by far the largest yet spotted from such an early date, researchers have announced. The object, discovered by astronomers in 2013, is 12 billion times as massive as the Sun, and six times greater than its largest-known contemporaries. Its existence poses a challenge for theories of the evolution of black holes, stars and galaxies, astronomers say.

Light from the black hole took 12.9 billion years to reach Earth, so astronomers see the object as it was 900 million years after the Big Bang. That "is actually a very short time" for a black hole to have grown so large, says astronomer Xue-Bing Wu of Peking University in Beijing. He led an international collaboration that describes the discovery in *Nature*<sup>1</sup>.

For its age, this black hole "is really much more massive than anything else we have seen so far", says Christian Veillet, director of the Large Binocular Telescope Observatory in Tucson, Arizona.

# Interstellar





**Figure 13.** Inset: paint-swath accretion disk with inner and outer radii  $r = 9.26M$  and  $r = 18.70M$  before being placed around a black hole. Body: this paint-swath disk, now in the equatorial plane around a black hole with  $a/M = 0.999$ , as viewed by a camera at  $r_c = 74.1M$  and  $\theta_c = 1.511$  ( $86.56^\circ$ ), ignoring frequency shifts, associated colour and brightness changes, and lens flare. (Figure from *The Science of Interstellar* [40], used by permission of W. W. Norton & Company, Inc. and created by our Double Negative team, <sup>TM</sup> & © Warner Bros. Entertainment Inc. (s15)). This image may be used under the terms of the Creative Commons Attribution-NonCommercial-NoDerivs 3.0 (CC BY-NC-ND 3.0) license. Any further distribution of these images must maintain attribution to the author(s) and the title of the work, journal citation and DOI. You may not use the images for commercial purposes and if you remix, transform or build upon the images, you may not distribute the modified images.

itself. This entire image comes from light rays emitted by the disk's bottom face: the wide bottom portion of the image, from rays that originate behind the hole, and travel under the hole and back upward to the camera; the narrow top portion, from rays that originate on the disk's front underside and travel under the hole, upward on its back side, over its top, and down to the camera—making one full loop around the hole.

There is a third disk image whose bottom portion is barely visible near the shadow's edge. That third image consists of light emitted from the disk's top face, that travels around the hole once for the visible bottom part of the image, and one and a half times for the unresolved top part of the image.

In the remainder of this section 4 we deal with a moderately realistic accretion disk—but a disk created for *Interstellar* by Double Negative artists rather than created by solving astrophysical equations such as [32]. In appendix A.6 we give some details of how this and other Double Negative accretion disk images were created. This artists' *Interstellar* disk was chosen to be very anemic compared to the disks that astronomers see around black holes and that astrophysicists model—so the humans who travel near it will not get fried by x-rays and gamma-rays. It is physically thin and marginally optically thick and lies in the black hole's equatorial plane. It is not currently accreting onto the black hole, and it has cooled to a position-independent temperature  $T = 4500$  K, at which it emits a black-body spectrum.

Figure 14 shows an image of this artists' disk, generated with a gravitational lensing geometry and computational procedure identical to those for our paint-swath disk, figure 13

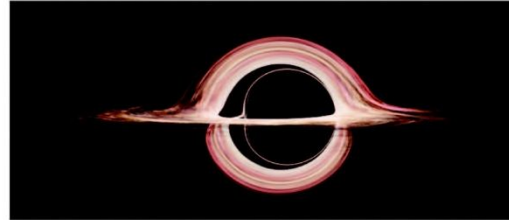


**Figure 14.** A moderately realistic accretion disk, created by Double Negative artists and gravitationally lensed by the same black hole with  $a/M = 0.999$  as in figure 13 and with the same geometry.

(no frequency shifts or associated colour and brightness changes; no lens flare). Christopher Nolan and Paul Franklin decided that the flattened left edge of the black-hole shadow, and the multiple disk images alongside that left edge, and the off-centred disk would be too confusing for a mass audience. So—although *Interstellar*'s black hole had to spin very fast to produce the huge time dilations seen in the movie—for visual purposes Nolan and Franklin slowed the spin to  $a/M = 0.6$ , resulting in the disk of figure 15(a).

**4.1.2. Colour and brightness changes due to frequency shifts.** The influences of Doppler and gravitational frequency shifts on the appearance of this disk are shown in figures 15(b) and (c).

Since the left side of the disk is moving toward the camera and the right side away with speeds of roughly  $0.55c$ , their light frequencies get shifted blueward on the left and redward on the right—by multiplicative factors of order 1.5 and 0.4 respectively when one combines the Doppler shift with a  $\sim 20\%$  gravitational redshift. These frequency changes induce changes in the disk's perceived *colours* (which we compute by convolving the frequency-shifted spectrum with the sensitivity curves of motion picture film) and also induce changes in the disk's perceived *brightness*; see appendix A.6 for some details.

In figure 15(b), we have turned on the colour changes, but not the corresponding brightness changes. As expected, the disk has become blue on the left and red on the right.

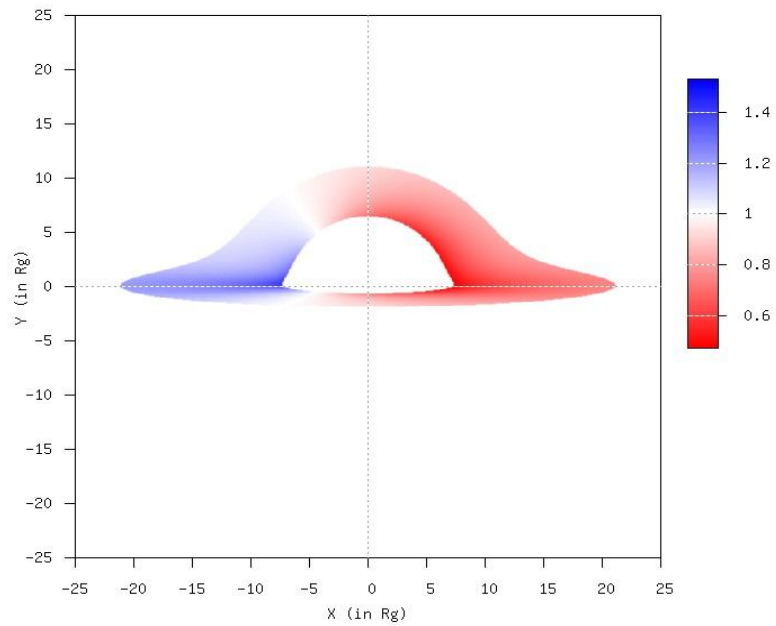
In figure 15(c), we have turned on both the colour and the brightness changes. Notice that the disk's left side, moving toward the camera, has become very bright, while the right side, moving away, has become very dim. This is similar to astrophysically observed jets, emerging from distant galaxies and quasars; one jet, moving toward Earth is typically bright, while the other, moving away, is often too dim to be seen.

#### 4.2. Lens flare and the accretion disk in the movie *Interstellar*

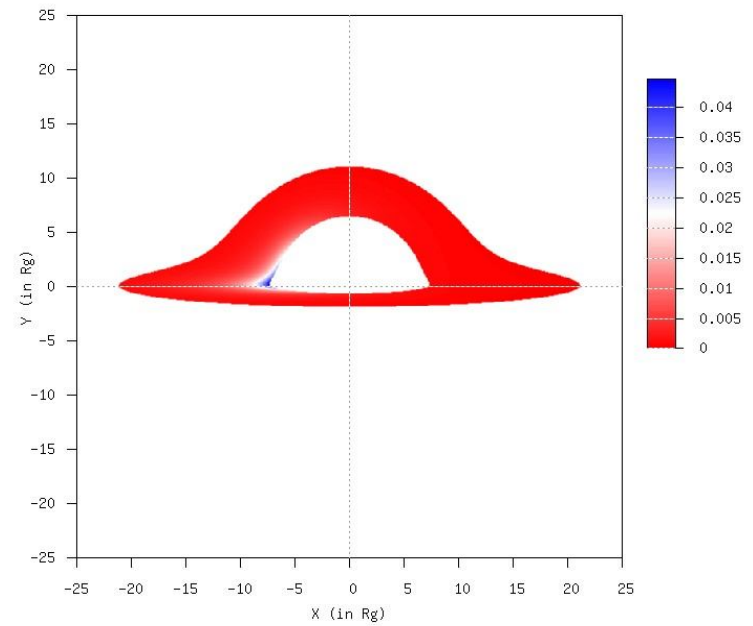
Christopher Nolan, the director and co-writer of *Interstellar*, and Paul Franklin, the visual effects supervisor, were committed to make the film as scientifically accurate as possible—within constraints of not confusing his mass audience unduly and using images that are exciting and fresh. A fully realistic accretion disk, figure 15(c), that is exceedingly lopsided, with the hole's shadow barely discernible, was obviously unacceptable.

# Schwarzschild black hole images: $\theta=85$ deg

- Redshift map

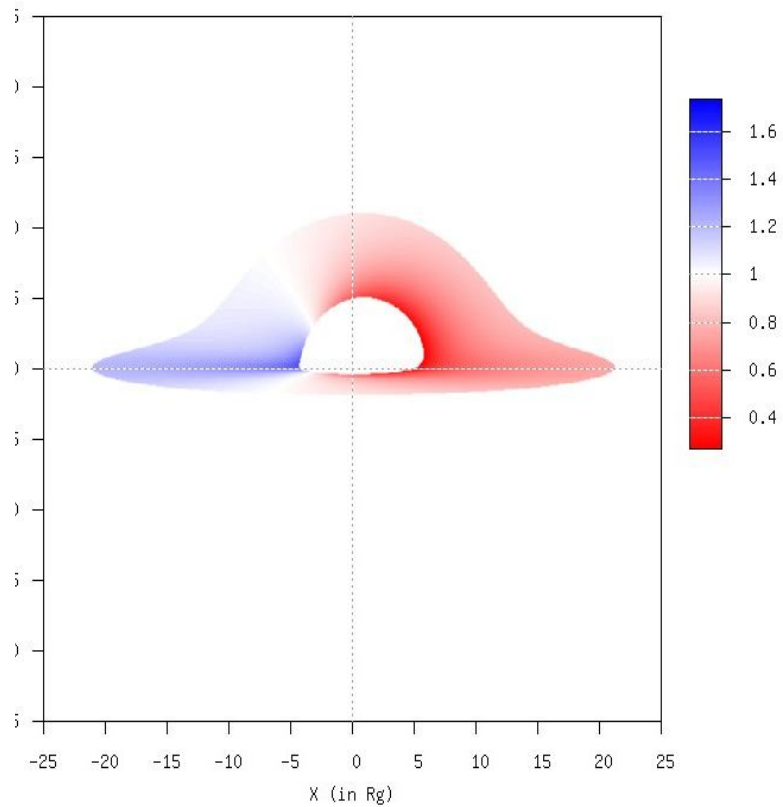


- Intensity map

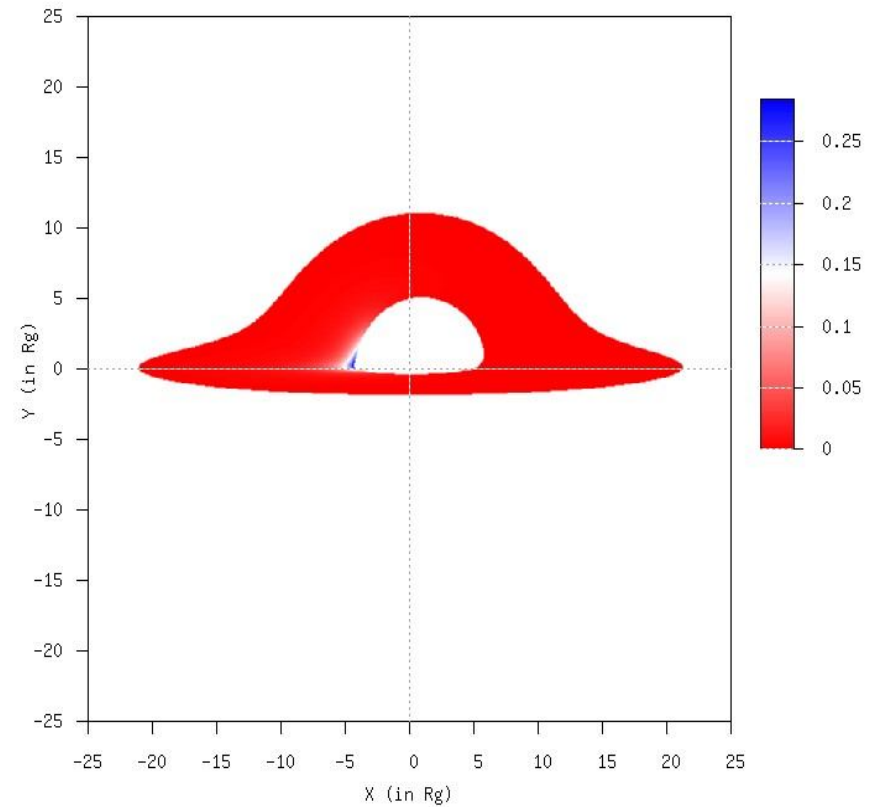


# Kerr black hole images ( $a=0.75$ ): $\theta=85$ deg

- Redshift map

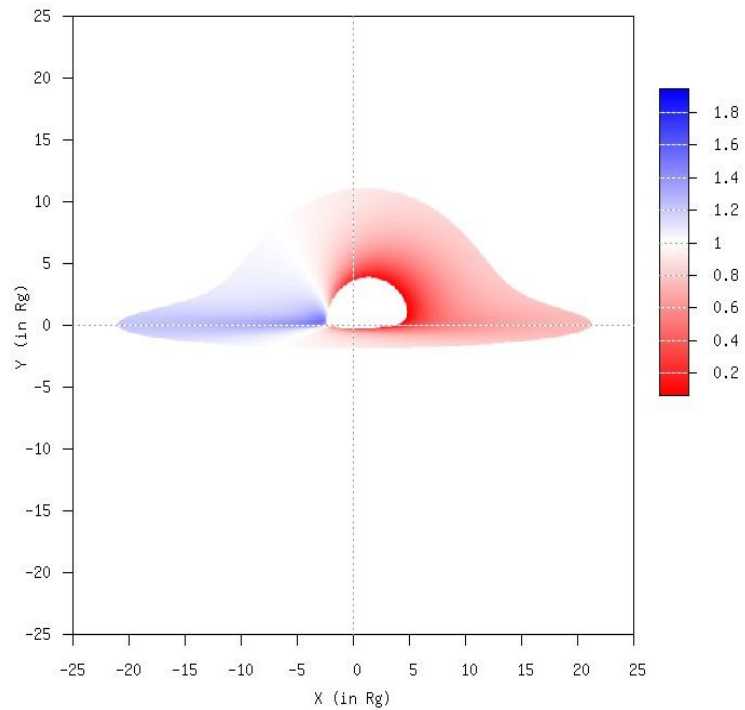


- Intensity map

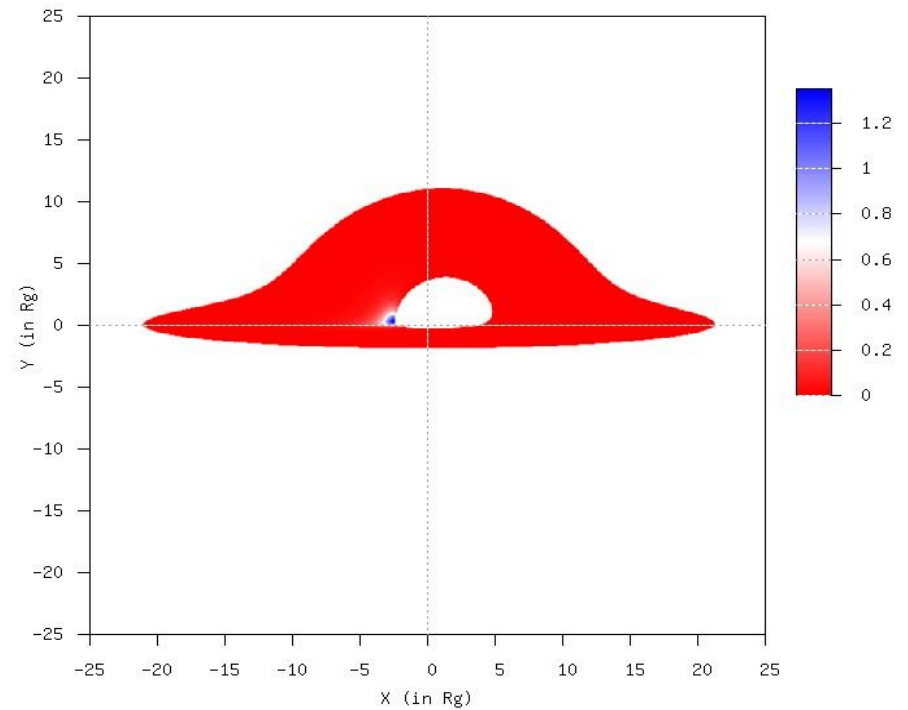


# Kerr black hole images ( $a=0.99$ ): $\theta=85$ deg

- Redshift map



- Intensity map



1973ApJ...133..237C

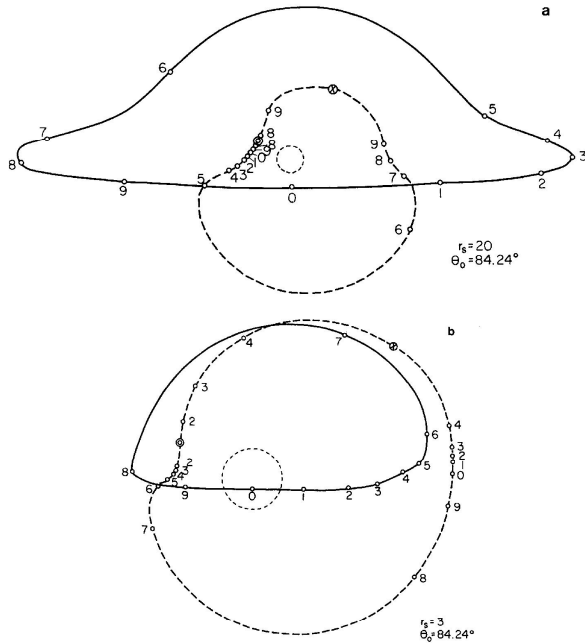


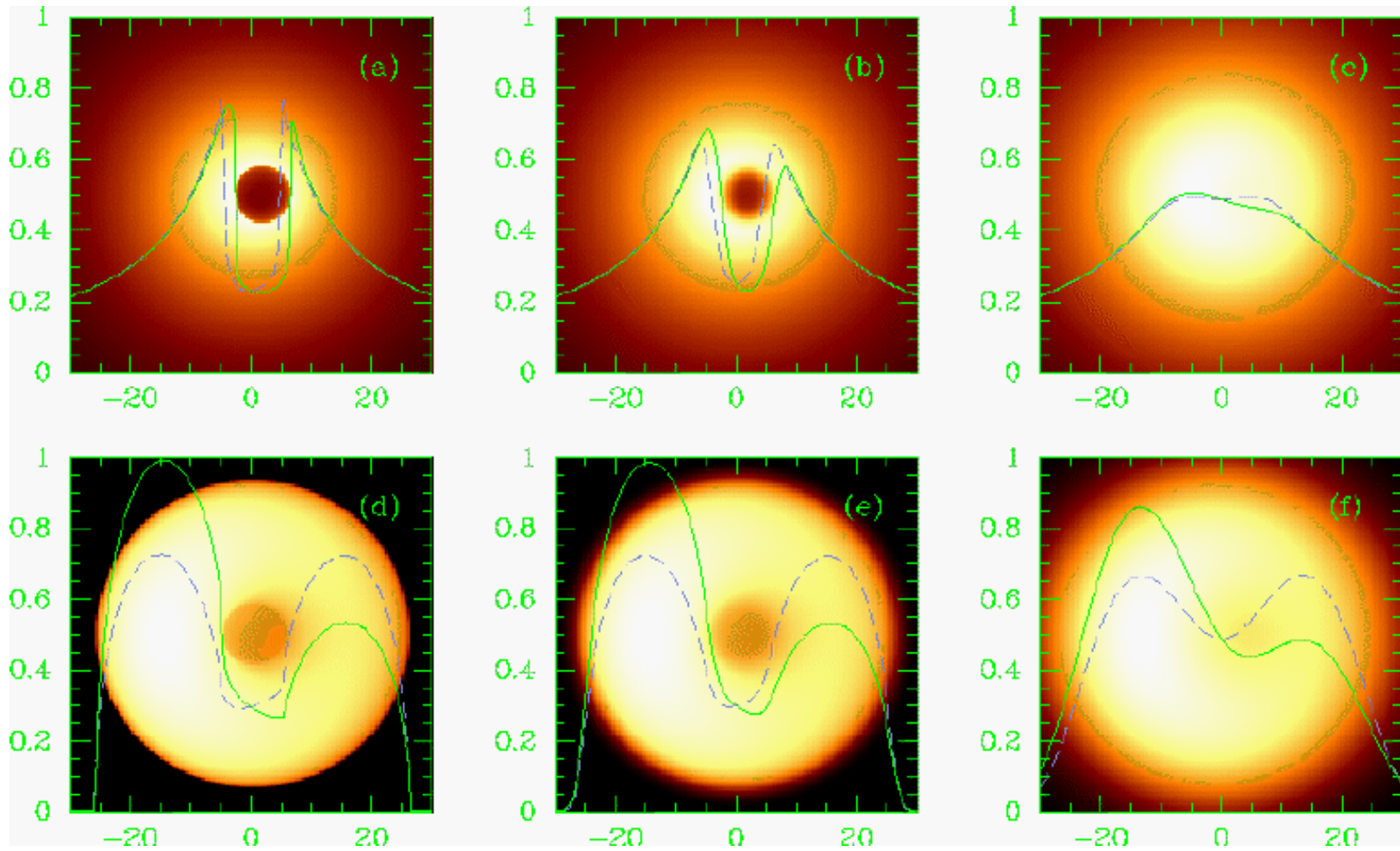
FIG. 8.—Apparent positions of the two brightest images as functions of time for two orbital radii and an observer at a polar angle  $\theta_0 = 84^\circ 24'$ . The small, dashed circle in each plot is the locus  $\alpha^2 + \beta^2 = 1$  and gives the scale of the plot. The direct image moves along the solid line; the one-orbit image, along the dashed line. Ticks mark the positions of the images at 10 equally spaced times. A pair of one-orbit images appears to be created at the points  $\odot$  and annihilated at the points  $\otimes$ . See text.

fore of  $\alpha$ ) and the variation in surface brightness increase more rapidly for the one-orbit image than for the direct image as we consider stars of progressively smaller orbital radii.

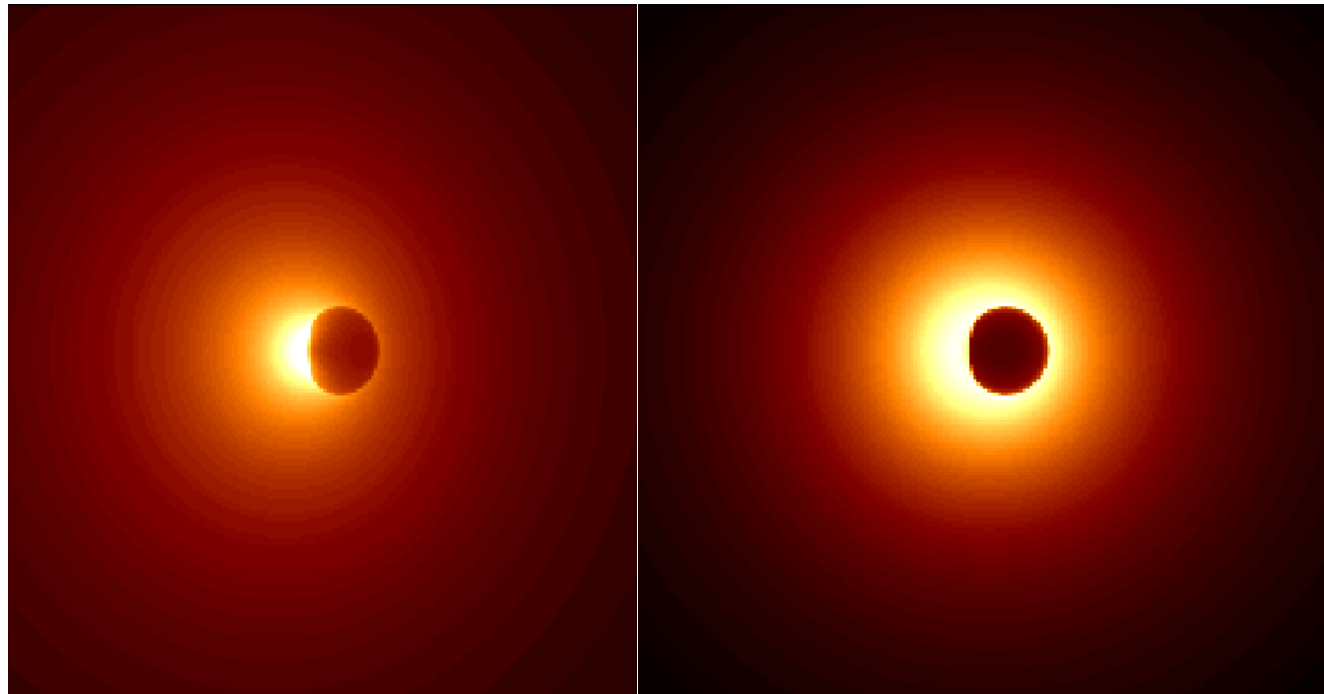
As the apparent position of the image seen by the distant observer changes, so does the corresponding direction of emission in the local rest frame of the star. If the instantaneous direction of emission of the beam of radiation which reaches the observer is represented by a point in figure 3 (for  $r_s = 1.5$ ), this point moves along the  $\cos \theta_0 = \text{const.}$  curve corresponding to the given type of image in the direction indicated by the arrows. Creation of pairs of images on the one-orbit curves is at the points marked  $\odot$ ; destruction, at points  $\otimes$ . For  $r_s = 1.5$  there is no retrograde image and, hence, no creation and destruction of images for observers with  $\theta_0 \lesssim 40^\circ$ .

When  $r_s$  is not much larger than unity, the images move very slowly on the parts of the curves nearest the backward  $\phi$ -direction and very rapidly on the remainder of the

# Falcke, Melia, Agol



# Shadows from Melia



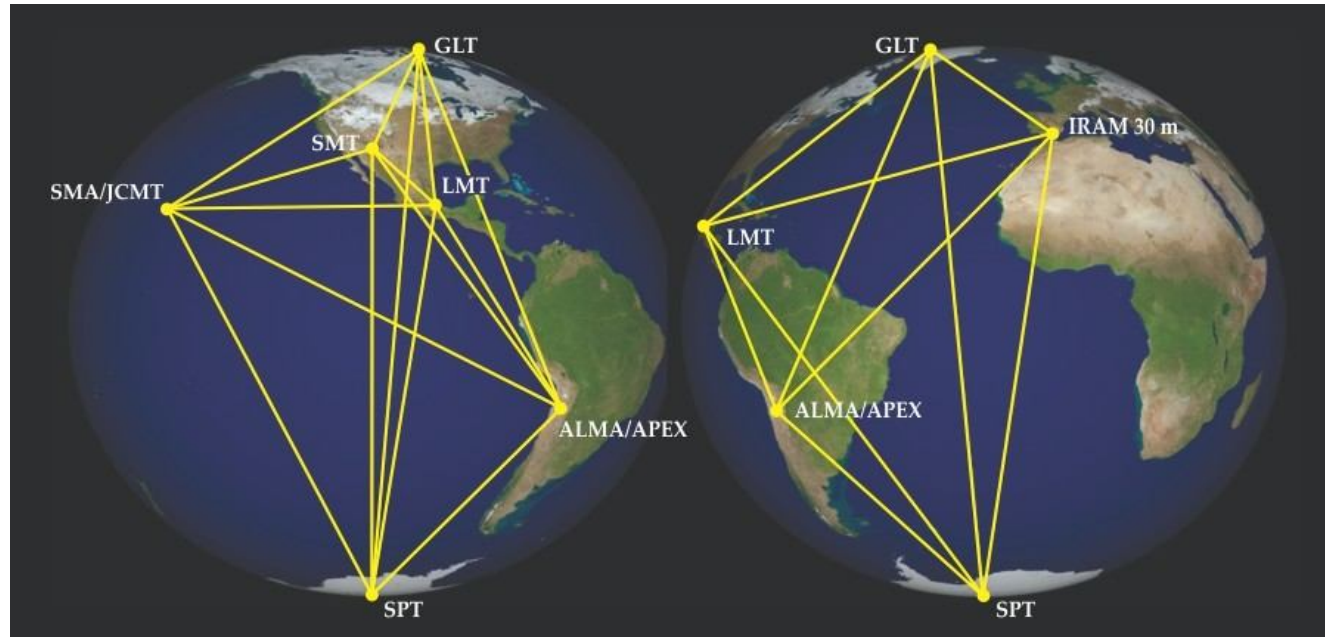


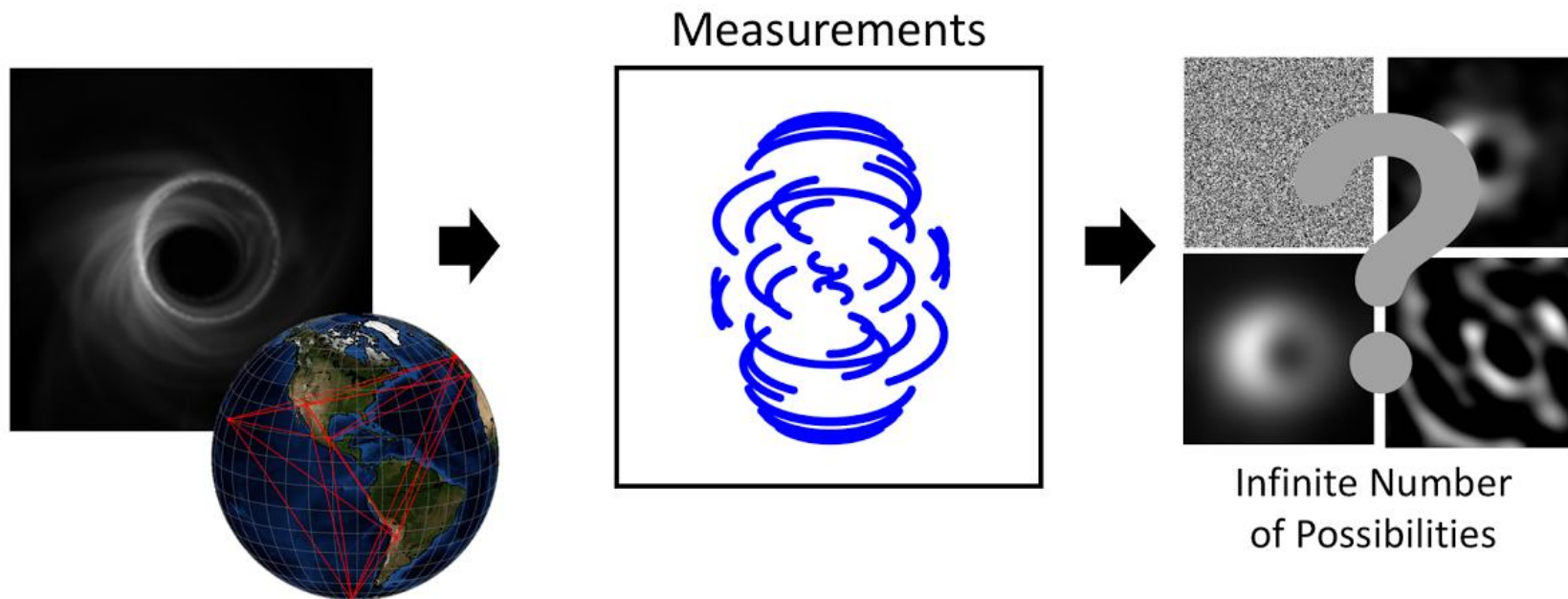
Figure 2. **The Event Horizon Telescope** is a global array of millimeter telescopes (see <http://eventhorizontelescope.org/array>) that aims to take the first pictures of black holes. (Courtesy of Dan Marrone/University of Arizona.)

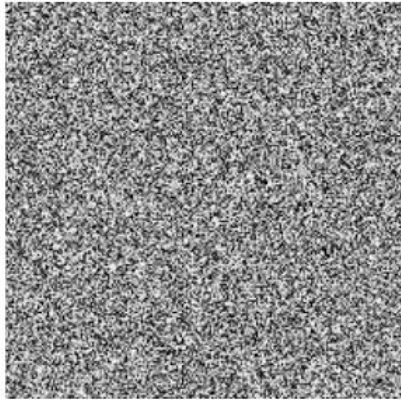
Published in: Dimitrios Psaltis; Feryal Özel; *Physics Today* **2018**, 71, 70-71.

DOI: 10.1063/PT.3.3906

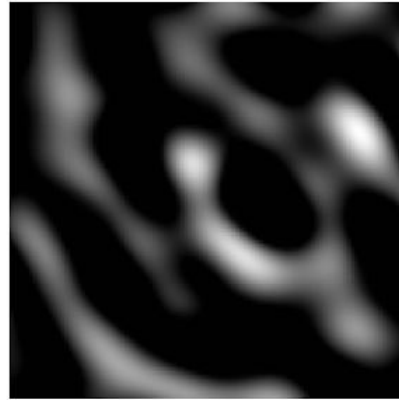
Copyright © 2018 American Institute of Physics

EHT team: “Similarly, for the EHT, the data we take only tells us only a piece of the story, as there are an infinite number of possible images that are perfectly consistent with the data we measure. But not all images are created equal— some look more like what we think of as images than others. To chose the best image, we essentially take all of the infinite images that explain our telescope measurements, and rank them by how reasonable they look. We then choose the image (or set of images) that looks most reasonable. ”

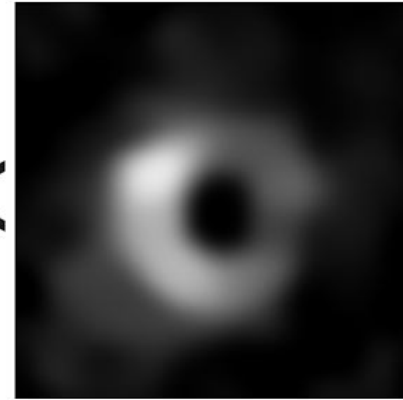




Unlikely

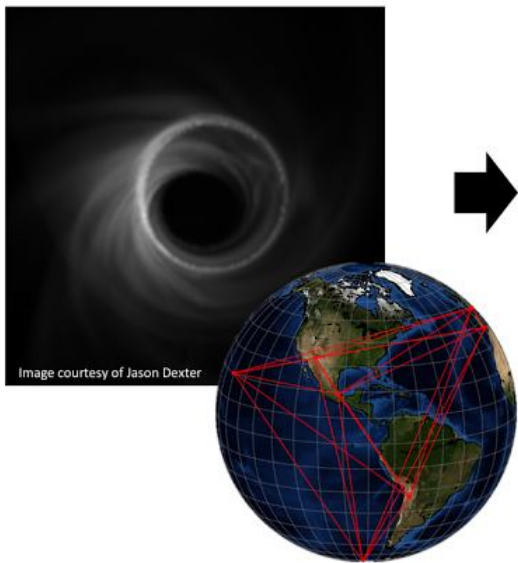


More Likely

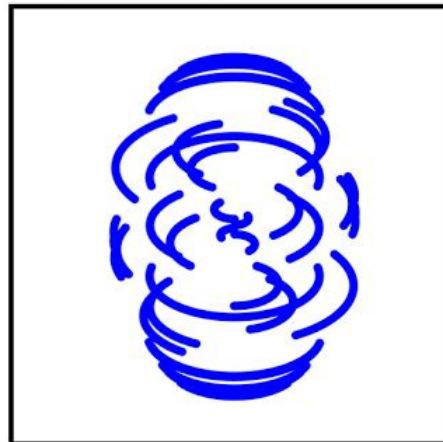


Very Likely

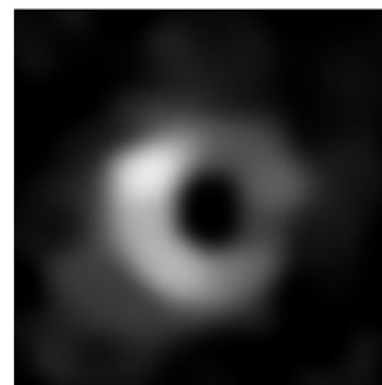




Measurements



Reconstruction





## The Size, Shape, and Scattering of Sagittarius A\* at 86 GHz: First VLBI with ALMA

S. Issaoun<sup>1,2</sup>, M. D. Johnson<sup>2</sup>, L. Blackburn<sup>2</sup>, C. D. Brinkerink<sup>1</sup>, M. Mościbrodzka<sup>1</sup>, A. Chael<sup>2</sup>, C. Goddi<sup>1,3</sup>,  
I. Martí-Vidal<sup>4</sup>, J. Wagner<sup>5</sup>, S. S. Doeleman<sup>2</sup>, H. Falcke<sup>1</sup>, T. P. Krichbaum<sup>5</sup>, K. Akiyama<sup>6,7</sup>, U. Bach<sup>5</sup>, K. L. Bouman<sup>2</sup>,  
G. C. Bower<sup>8</sup>, A. Broderick<sup>9</sup>, I. Cho<sup>10,11</sup>, G. Crew<sup>6</sup>, J. Dexter<sup>12</sup>, V. Fish<sup>6</sup>, R. Gold<sup>9,13</sup>, J. L. Gómez<sup>14</sup>, K. Hada<sup>15</sup>,  
A. Hernández-Gómez<sup>16,17</sup>, M. Janßen<sup>1</sup>, M. Kino<sup>15</sup>, M. Kramer<sup>5</sup>, L. Loinard<sup>16,18</sup>, R.-S. Lu<sup>5,19</sup>, S. Markoff<sup>20</sup>,  
D. P. Marrone<sup>21</sup>, L. D. Matthews<sup>6</sup>, J. M. Moran<sup>2</sup>, C. Müller<sup>1,5</sup>, F. Roelofs<sup>1</sup>, E. Ros<sup>5</sup>, H. Rottmann<sup>5</sup>, S. Sanchez<sup>22</sup>,  
R. P. J. Tilanus<sup>1,3</sup>, P. de Vicente<sup>23</sup>, M. Wielgus<sup>2</sup>, J. A. Zensus<sup>5</sup>, and G.-Y. Zhao<sup>10</sup>

<sup>1</sup> Department of Astrophysics/IMAPP, Radboud University, P.O. Box 9010, 6500 GL Nijmegen, The Netherlands

<sup>2</sup> Harvard-Smithsonian Center for Astrophysics, 60 Garden Street, Cambridge, MA 02138, USA

<sup>3</sup> ALLEGRO/Leiden Observatory, Leiden University, P.O. Box 9513, 2300 RA, Leiden, The Netherlands

<sup>4</sup> Department of Space, Earth and Environment, Chalmers University of Technology, Onsala Space Observatory, SE-439 92 Onsala, Sweden

<sup>5</sup> Max-Planck-Institut für Radioastronomie, Auf dem Hügel 69, D-53121 Bonn, Germany

<sup>6</sup> Massachusetts Institute of Technology, Haystack Observatory, 99 Millstone Road, Westford, MA 01886, USA

<sup>7</sup> National Radio Astronomy Observatory, 520 Edgemont Road, Charlottesville, VA 22903, USA

<sup>8</sup> Institute of Astronomy and Astrophysics, Academia Sinica, P.O. Box 23-141, Taipei 10617, Taiwan

<sup>9</sup> Perimeter Institute for Theoretical Physics, 31 Caroline Street, North Waterloo, ON N2L 2Y5, Canada

<sup>10</sup> Korea Astronomy and Space Science Institute, Daedeokdaero 776, Yuseonggu, Daejeon 34055, Republic of Korea

<sup>11</sup> University of Science and Technology, Gajeong-ro 217, Yuseong-gu, Daejeon 34113, Republic of Korea

<sup>12</sup> Max-Planck-Institut für Extraterrestrische Physik, Giessenbachstr. 1, D-85748 Garching, Germany

<sup>13</sup> Institut für Theoretische Physik, Johann Wolfgang Goethe-Universität, Max-von-Laue-Straße 1, D-60438 Frankfurt, Germany

<sup>14</sup> Instituto de Astrofísica de Andalucía-CSIC, Glorieta de la Astronomía s/n, E-18008 Granada, Spain

<sup>15</sup> National Astronomical Observatory of Japan, 2-21-1 Osawa, Mitaka, Tokyo 181-8588, Japan

<sup>16</sup> Instituto de Radioastronomía y Astrofísica, Universidad Nacional Autónoma de México, Morelia 58089, México

<sup>17</sup> IRAP, Université de Toulouse, CNRS, UPS, CNES, Toulouse, France

<sup>18</sup> Instituto de Astronomía, Universidad Nacional Autónoma de México, Apartado Postal 70-264, 04510 Ciudad de México, México

<sup>19</sup> Shanghai Astronomical Observatory, Chinese Academy of Sciences, Shanghai 200030, People's Republic of China

<sup>20</sup> Anton Pannekoek Institute for Astronomy, University of Amsterdam, 1098 XH Amsterdam, The Netherlands

<sup>21</sup> University of Arizona, 933 North Cherry Avenue, Tucson, AZ 85721, USA

<sup>22</sup> Institut de RadioAstronomie Millimétrique (IRAM), Granada, Spain

<sup>23</sup> Observatorio de Yebes (IGN), Apartado 148, E-19180, Yebes, Spain

Received 2018 October 19; revised 2018 December 7; accepted 2018 December 7; published 2019 January 21

### Abstract

The Galactic center supermassive black hole Sagittarius A\* (Sgr A\*) is one of the most promising targets to study the dynamics of black hole accretion and outflow via direct imaging with very long baseline interferometry (VLBI). At 3.5 mm (86 GHz), the emission from Sgr A\* is resolvable with the Global Millimeter VLBI Array (GMVA). We present the first observations of Sgr A\* with the phased Atacama Large Millimeter/submillimeter Array (ALMA) joining the GMVA. Our observations achieve an angular resolution of  $\sim 87 \mu\text{as}$ , improving upon previous experiments by a factor of two. We reconstruct a first image of the unscattered source structure of Sgr A\* at 3.5 mm, mitigating the effects of interstellar scattering. The unscattered source has a major-axis size of  $120 \pm 34 \mu\text{as}$  ( $12 \pm 3.4$  Schwarzschild radii) and a symmetrical morphology (axial ratio of  $1.2^{+0.3}_{-0.2}$ ), which is further supported by closure phases consistent with zero within  $3\sigma$ . We show that multiple disk-dominated models of Sgr A\* match our observational constraints, while the two jet-dominated models considered are constrained to small viewing angles. Our long-baseline detections to ALMA also provide new constraints on the scattering of Sgr A\*, and we show that refractive scattering effects are likely to be weak for images of Sgr A\* at 1.3 mm with the Event Horizon Telescope. Our results provide the most stringent constraints to date for the intrinsic morphology and refractive scattering of Sgr A\*, demonstrating the exceptional contribution of ALMA to millimeter VLBI.

**Key words:** accretion, accretion disks – galaxies: individual (Sgr A\*) – Galaxy: center – techniques: interferometric

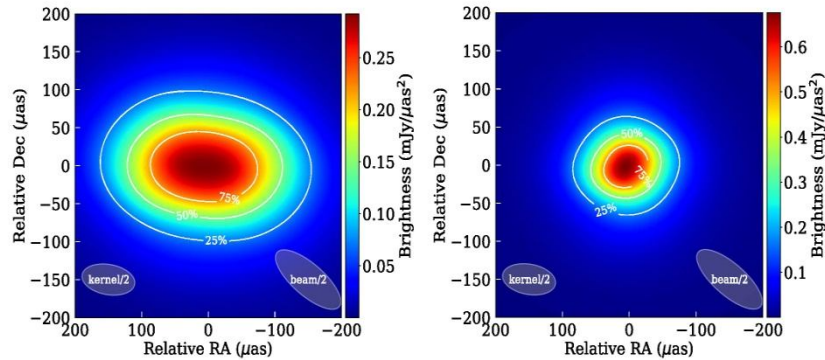


**Figure 5.** Left: scattered image of Sgr A\*, reconstructed with the second-moment regularizer and stochastic optics ( $\theta_{\text{maj}} = 228 \pm 46 \mu\text{as}$ ,  $\theta_{\text{min}} = 143 \pm 20 \mu\text{as}$  from LSQ). Right: reconstructed image from stochastic optics (Johnson 2016) of the intrinsic source ( $\theta_{\text{maj}} = 120 \pm 34 \mu\text{as}$ ,  $\theta_{\text{min}} = 100 \pm 18 \mu\text{as}$  from LSQ). In each panel, the ellipses at the bottom indicate half the size of the scatter-broadening kernel ( $\theta_{\text{maj}} = 159.9 \mu\text{as}$ ,  $\theta_{\text{min}} = 79.5 \mu\text{as}$ , PA =  $81.7^\circ$ ) and the observing beam.

excellent accuracy in previous experiments, we do not expect either of these effects to significantly advantage the reconstructions of simulated data.

In Figure 6, we present the original 3D GRMHD model images, the model images scattered with the J18 scattering model (as observed in the simulated observations), and the reconstructed observed (scattered) and intrinsic images from the imaging method. In Table 2, we compare the true intrinsic source sizes from the models to the intrinsic source sizes derived from the imaging routine. We determined the source size parameters using two methods: (1) measuring the second central moment of the image (2nd mom.) and deriving Gaussian parameters and (2) doing a 2D Gaussian fit with a least-squares minimization (LSQ) onto the image.

Next, we evaluate the difference between true and reconstructed image parameters. We sought to define an approach that quantifies these differences in a way that is related to the reconstructed image properties and the observing beam. When expressed in this way, we can use parameter errors on these reconstructed simulated images to predict uncertainties on parameters derived from our reconstructed image with data.

To this end, Table 2 expresses the difference between the true and measured source major and minor axes as a fraction of the projected beam FWHM  $\theta_{\text{beam}}$  along the corresponding axis. For the axial ratio, we express the difference between the true and measured ratios as a fraction of the cumulative error from both axes (the projected beam widths along the measured major and minor axes added quadratically).

However, while it is straightforward and well motivated to express uncertainties on axis lengths and their ratio in terms of the observing beam, uncertainty on the PA is more subtle. We opted to create an ensemble of beam-convolved reconstructed images and use the scatter in the PA of the ensemble as an estimate of the PA uncertainty. The ensemble of images is constructed by convolving the single reconstructed image with an ensemble of narrow beams, sampling all PAs. Each of these beams has a major-axis size given by the projected observing beam size along the same PA and a minor-axis size of zero. We thereby stretch the image along each direction, up to the extent of the observing beam, and examine the overall dependence of

the reconstructed image on this stretching. With this approach, images that are nearly isotropic will have large PA uncertainty, while highly elongated images (relative to the beam size) will have small PA uncertainty.

In general, we find that the LSQ method fares better than second moment for determining the source parameters, likely due to weak extended flux in the images skewing the second-moment parameters to larger values. As expected, both methods perform poorly when determining the PA of a fairly symmetrical source, for which it remains largely unconstrained. However, for more elongated source geometry, both methods are able to accurately recover the intrinsic PA. We adopt the LSQ method to quantify the size of Sgr A\* via image-domain fitting. Although the Gaussian approximation does not fully describe our source morphology, it is suitable for comparisons to visibility-domain model fits from the previous observations of Sgr A\* presented in Section 5.

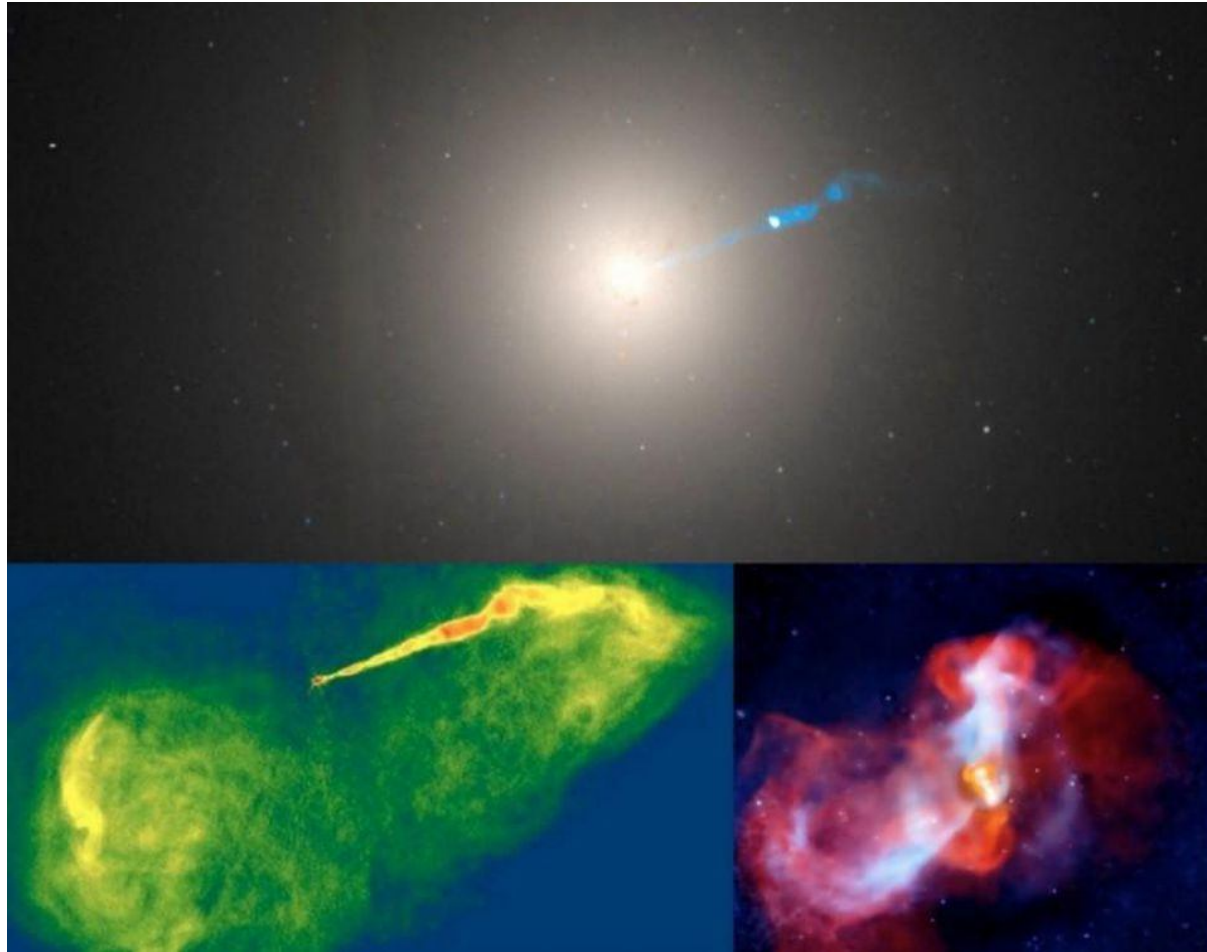
## 5. Results

### 5.1. Intrinsic Source Constraints from Imaging

Figure 5 shows the unscattered and scattered images of Sgr A\*, as imaged following the method described in Section 4. The (uniform-weighted) beam size of the Sgr A\* observations is  $(235 \times 87) \mu\text{as}$ , with a PA (east of north) of  $53.6^\circ$ . While the shorter baselines of the array (intra-VLBA, VLBA-GBT, and intra-European) see primarily a Gaussian source elongated in the east–west direction, longer baselines are expected to pick up on non-Gaussian source structure or refractive noise from interstellar scattering. In this particular observation, our longest baselines are mainly north–south to ALMA (see Figure 1), where scattering has less of an effect on the source. As seen in Figure 5, left panel, the reconstructed scattered image looks very smooth and Gaussian-like, showing no obvious refractive noise in the image. We also see a similar outcome in our imaging tests, presented in Section 4.2.3. Although the scattered images (second column in Figure 6) have visible ripples of scattering substructure, the reconstructed scattered images (third column) appear very smooth. This is likely because our GMVA+ALMA observations sample low levels of refractive noise mainly along the north–south direction, whereas our east–west sensitivity and resolution do not

- On April 10th 2019, the [Event Horizon Telescope \(EHT\) Collaboration](#) presented its first results -- an image of the supermassive black hole in galaxy M87 -- in multiple simultaneous press conferences around the world. The official EHT press release appears on the [home page](#) of this website. This page contains links to recorded press conferences, press releases from our partner institutions, and supporting materials published along with press releases.
- 
- **Press conference recordings:**
- [Brussels](#), hosted by the European Research Council (in English)
- [Santiago](#), hosted by the Joint ALMA Observatory (in Spanish and English)
- [Taipei](#), hosted by the Academia Sinica (in Chinese)
- [Tokyo](#), hosted by the National Astronomical Observatory of Japan (in Japanese)
- [Washington](#), hosted by the US National Science Foundation (in English)

- The image shows a crescent-shaped, ring-like structure with a dark central region - the black hole's shadow.
- The black hole revealed is at the center of M87, about 55 million light-years from Earth, with a mass 6.5 billion times that of the Sun.
- "This is the first direct visual evidence about black holes obtained by humans, confirming that Einstein's theory of general relativity still holds in extreme conditions," said Shen Zhiqiang, head of Shanghai Astronomical Observatory (SAO).





# EHT results in brief

- **First M87 Event Horizon Telescope Results. I. The Shadow of the Supermassive Black Hole, ApJL 875 L1.**
- To image and study this phenomenon, we have assembled the Event Horizon Telescope, a global very long baseline interferometry array observing at a wavelength of 1.3 mm. This allows us to reconstruct event-horizon-scale images of the supermassive black hole candidate in the center of the giant elliptical galaxy M87. We have resolved the central compact radio source as an asymmetric bright emission ring with a diameter of  $42 \pm 3 \mu\text{as}$ . derive a central mass of  $M_{\text{BH}} = (6.5 \pm 0.7) \times 10^9 M_{\text{Sun}}$ .
- In many AGNs, collimated relativistic plasma jets (Bridle & Perley 1984; Zensus 1997) launched by the central black hole contribute to the observed emission. These jets may be powered either by magnetic fields threading the event horizon,
- extracting the rotational energy from the black hole (Blandford & Znajek 1977), or from the accretion flow (Blandford & Payne 1982). The near-horizon emission from low-luminosity active galactic nuclei (LLAGNs; Ho 1999) is produced by
- synchrotron radiation that peaks from the radio through the far infrared. This emission may be produced either in the accretion flow (Narayan et al. 1995), the jet (Falcke et al. 1993), or both (Yuan et al. 2002).

# EHT results in brief

- We have to squeeze
  - 1) Efforts of several hundreds people for two year in 0.5 hour and
  - 2) five petabytes (5242880 Gb) information into around 20kb image (it was the goal of these intensive studies) therefore one has around  $2.5 * 10^{11}$  “compression” of information

- When viewed from infinity, a nonrotating Schwarzschild (1916) black hole has a photon capture impact parameter  $R_c = (27)^{1/2} r_g$ , where  $r_g = GM/c^2$  is the characteristic length scale of a black hole. The photon capture radius is larger than the Schwarzschild radius  $R_S$  that marks the event horizon of a nonrotating black hole,  $R_S \equiv 2 r_g$ . Photons approaching the black hole with an impact parameter  $b < R_c$  are captured and plunge into the black hole; photons with  $b > R_c$  escape to infinity; photons with  $b = R_c$  are captured on an unstable circular orbit and produce what is commonly referred to as the lensed “photon ring.” In the Kerr metric, which describes black holes with spin angular momentum,  $R_c$  consists of two parameters  $(\alpha, \beta)$  and changes with the ray’s orientation relative to the angular-momentum vector, and the black hole’s cross section is not necessarily circular (Bardeen, 1973).

- Started in 2009 (Doeleman et al. 2009), the EHT began a program to address these challenges by increasing array sensitivity.
- Parallel efforts to support infrastructure upgrades at additional VLBI sites, including the Atacama Large Millimeter/submillimeter Array (ALMA) and the Atacama Pathfinder Experiment telescope (APEX) in Chile, the Large Millimeter Telescope Alfonso Serrano (LMT) in Mexico, the IRAM 30m telescope on Pico Veleta (PV) in Spain, the Submillimeter Telescope Observatory in Arizona (SMT), the James Clerk Maxwell Telescope (JCMT) and the Submillimeter Array (SMA) in Hawai'i and the South Pole Telescope (SPT) in Antarctica extended the range of EHT baselines and coverage, and the overall collecting area of the array. These developments increased the sensitivity of the EHT by a factor of  $\sim 30$  over early experiments that confirmed horizon-scale structures in M87\* and Sgr A\* (Doeleman et al. 2008, 2012; Akiyama et al. 2015; Johnson et al. 2015; Fish et al. 2016; Lu et al. 2018). For the observations at a wavelength of 1.3 mm presented here, the EHT collaboration fielded a global VLBI array of eight stations over six geographical locations.
- Baseline lengths ranged from 160 m to 10,700 km toward M87\*, resulting in an array with a theoretical diffraction-limit resolution of  $\sim 25 \mu\text{as}$ .

The array has a nominal angular resolution of  $\lambda/L$ , where  $\lambda$  is the observing wavelength and  $L$  is the maximum projected baseline length between telescopes in the array (Thompson et al. 2017). In this way, VLBI creates a virtual telescope that spans nearly the full diameter of the Earth.

To measure interferometric visibilities, the widely separated telescopes simultaneously sample and coherently record the radiation field from the source. Synchronization using the Global Positioning System typically achieves temporal alignment of these recordings within tens of nanoseconds. Each station is equipped with a hydrogen maser frequency standard. With the atmospheric conditions during our observations the coherent integration time was typically 10 s (see Figure 2 in Paper II). Use of hydrogen maser frequency standards at all EHT sites ensures coherence across the array over this timescale. After observations, recordings are staged at a central location, aligned in time, and signals from each telescope-pair are cross-correlated.

While VLBI is well established at centimeter and millimeter wavelengths (Boccardi et al. 2017; Thompson et al. 2017) and can be used to study the immediate environments of black holes (Krichbaum et al. 1993; Doeleman et al. 2001), the extension of VLBI to a wavelength of 1.3 mm has required long-term technical developments. Challenges at shorter wavelengths include increased noise in radio receiver electronics, higher atmospheric opacity, increased phase fluctuations caused by atmospheric turbulence, and decreased efficiency and size of radio telescopes in the millimeter and submillimeter observing bands. Started in 2009 (Doeleman et al. 2009a), the EHT began a program to address these challenges by increasing array sensitivity. Development and deployment of broadband VLBI systems (Whitney et al. 2013; Vertatschitsch et al. 2015) led to data recording rates that now exceed those of typical cm-VLBI arrays by more than an order of magnitude. Parallel efforts to support infrastructure upgrades at additional VLBI sites, including the Atacama Large Millimeter/submillimeter Array (ALMA; Matthews et al. 2018; Goddi et al. 2019) and the Atacama Pathfinder Experiment telescope (APEX) in Chile (Wagner et al. 2015), the Large Millimeter Telescope Alfonso Serrano (LMT) in Mexico (Ortiz-León et al. 2016), the IRAM 30 m telescope on Pico Veleta (PV) in Spain (Greve et al. 1995), the Submillimeter Telescope Observatory in Arizona (SMT; Baars et al. 1999), the James Clerk Maxwell Telescope (JCMT) and the Submillimeter Array (SMA) in Hawai'i (Doeleman et al. 2008; Primiani et al. 2016; Young et al. 2016), and the South Pole Telescope (SPT) in Antarctica (Kim et al. 2018a), extended the range of EHT baselines and coverage, and the overall collecting area of the array. These developments increased the sensitivity of the EHT by a factor of  $\sim 30$  over early experiments that confirmed horizon-scale structures in M87\* and Sgr A\* (Doeleman et al. 2008, 2012; Akiyama et al. 2015; Johnson et al. 2015; Fish et al. 2016; Lu et al. 2018).

For the observations at a wavelength of 1.3 mm presented here, the EHT collaboration fielded a global VLBI array of eight stations over six geographical locations. Baseline lengths ranged from 160 m to 10,700 km toward M87\*, resulting in an array with a theoretical diffraction-limit resolution of  $\sim 25 \mu\text{as}$  (see Figures 1 and 2, and Paper II).

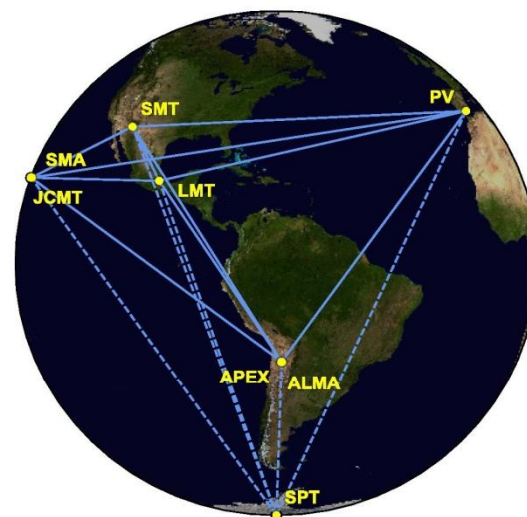


**Figure 1.** Eight stations of the EHT 2017 campaign over six geographic locations as viewed from the equatorial plane. Solid baselines represent mutual visibility on M87\* (+12° declination). The dashed baselines were used for the calibration source 3C279 (see Papers III and IV).

median zenith atmospheric opacities at 230 GHz ranging from 0.03 to 0.28 over the different locations. The observations were scheduled as a series of scans of three to seven minutes in duration, with M87\* scans interleaved with those on the quasar 3C 279. The number of scans obtained on M87\* per night ranged from 7 (April 10) to 25 (April 6) as a result of different observing schedules. A description of the M87\* observations, their correlation, calibration, and validated final data products is presented in Paper III and briefly summarized here.

At each station, the astronomical signal in both polarizations and two adjacent 2 GHz wide frequency bands centered at 227.1 and 229.1 GHz were converted to baseband using standard heterodyne techniques, then digitized and recorded at a total rate of 32 Gbps. Correlation of the data was carried out using a software correlator (Deller et al. 2007) at the MIT Haystack Observatory and at the Max-Planck-Institut für Radioastronomie, each handling one of the two frequency bands. Differences between the two independent correlators were shown to be negligible through the exchange of a few identical scans for cross comparison. At correlation, signals were aligned to a common time reference using an a priori Earth geometry and clock model.

A subsequent fringe-fitting step identified detections in correlated signal power while phase calibrating the data for residual delays and atmospheric effects. Using ALMA as a highly sensitive reference station enabled critical corrections for ionospheric and tropospheric distortions at the other sites. Fringe fitting was performed with three independent automated pipelines, each tailored to the specific characteristics of the EHT

# Event Horizon Telescope (EHT)

A Global Network of Radio Telescopes



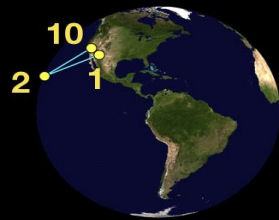
## 2018 Observatories

- ALMA**  Atacama Large Millimeter/ submillimeter Array  
CHAJNANTOR PLATEAU, CHILE
- APEX**  Atacama Pathfinder EXperiment  
CHAJNANTOR PLATEAU, CHILE
- 30-M**  IRAM 30-M Telescope  
PICO VELETA, SPAIN
- JCMT**  James Clerk Maxwell Telescope  
MAUNAKEA, HAWAII
- LMT**  Large Millimeter Telescope  
SIERRA NEGRA, MEXICO
- SMA**  Submillimeter Array  
MAUNAKEA, HAWAII
- SMT**  Submillimeter Telescope  
MOUNT GRAHAM, ARIZONA
- SPT**  South Pole Telescope  
SOUTH POLE STATION
- GLT**  The Greenland Telescope  
THULE AIR BASE, GREENLAND, DENMARK
- Kitt Peak**  Kitt Peak 12-meter Telescope  
KITZ PEAK, ARIZONA, USA
- NOEMA**  NOEMA Observatory  
PLATEAU DE BURE, FRANCE

Observing in 2020



Credit: M. Wielgus, D. Pesce



2009-2012



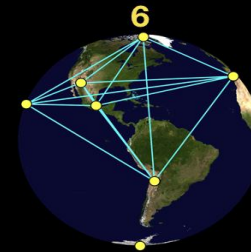
2013



2017



Event Horizon Telescope



2018



2021

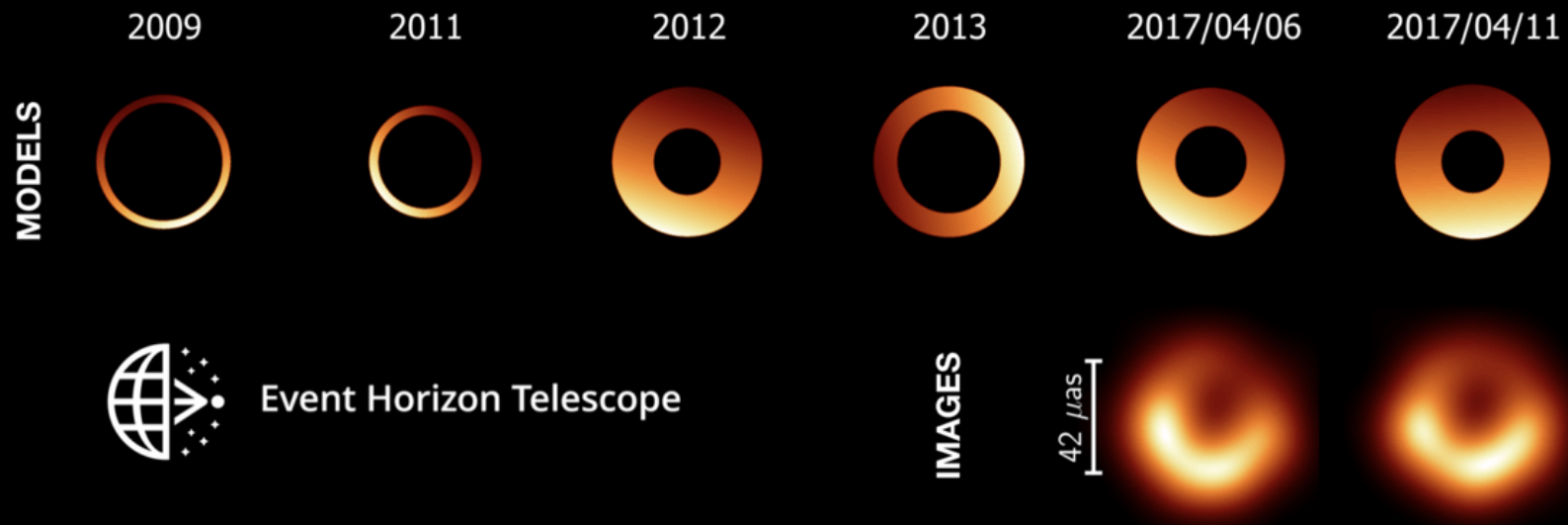
## The EHT array observing M87\*

1. **Mt Graham, Arizona, USA**  
SMT: Submillimeter Telescope (since 2009)
2. **Maunakea, Hawai'i, USA**  
JCMT: James Clerk Maxwell Telescope (since 2009)  
SMA: Submillimeter Array (since 2011)  
CSO: Caltech Submillimeter Observatory (2011)
3. **Atacama, Chile**  
APEX: Atacama Pathfinder Experiment (since 2013)  
ALMA: Atacama Large Millimeter/submillimeter Array (since 2017)
4. **Sierra Negra, Mexico**  
LMT: Large Millimeter Telescope Alfonso Serrano (since 2017)
5. **Pico Veleta, Spain**  
IRAM 30m: IRAM 30-meter telescope (since 2017)
6. **Thule, Greenland**  
GLT: Greenland Telescope (since 2018)
7. **Plateau de Bure, France**  
NOEMA: NOthern Extended Millimeter Array (since 2021)
8. **Kitt Peak, Arizona, USA**  
KP: ARO 12m Radio Telescope (since 2021)
9. **South Pole**  
SPT: South Pole Telescope (since 2017, not directly observing M87\*)
10. **Cedar Flat, California, USA**  
CARMA: Combined Array for Research in Millimeter-wave Astronomy (2009-2013)

## M87\* black hole appearance in 2009-2017

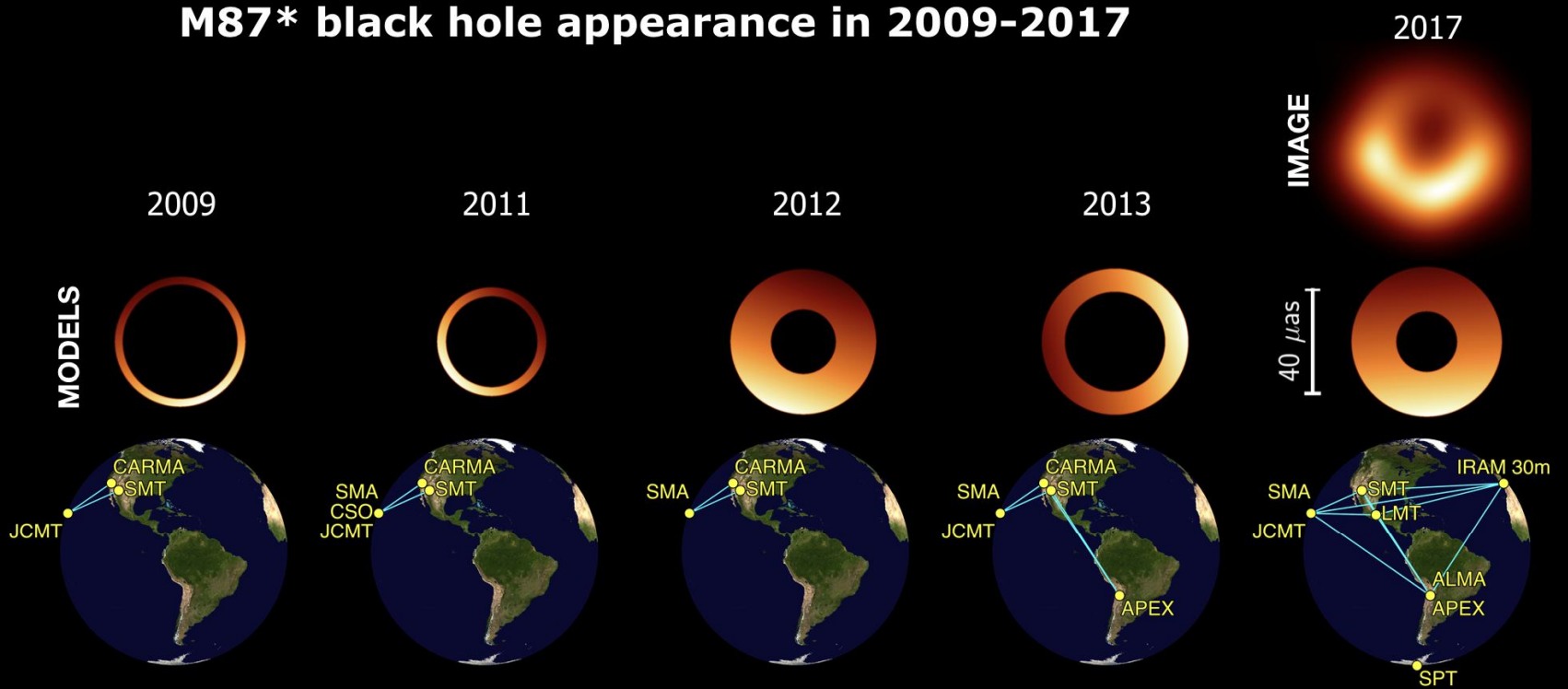
1/3

The EHT observed M87\* in 2009-2017. Only 2017 data allow to create images, but in all cases we can use simple geometric models to constrain approximated source morphology.



Credit: M. Wielgus

# M87\* black hole appearance in 2009-2017



Event Horizon Telescope

Credit: M. Wielgus, D. Pesce

# Observations, Correlation, and Calibration

- The EHT observed M87\* on 2017 April 5, 6, 10, and 11 with the EHT. Weather was uniformly good to excellent with nightly median zenith atmospheric opacities at 230 GHz ranging from 0.03 to 0.28 over the different locations. The observations were scheduled as a series of scans of three to seven minutes in duration.
- The number of scans obtained on M87\* per night ranged from 7 (April 10) to 25 (April 6) as a result of different observing schedules.
- Correlation of the data was carried out using a software correlator at the MIT Haystack Observatory and at the Max-Planck-Institut für Radioastronomie, each handling one of the two frequency bands. Differences between the two independent correlators were shown to be negligible through the exchange of a few identical scans for cross comparison.

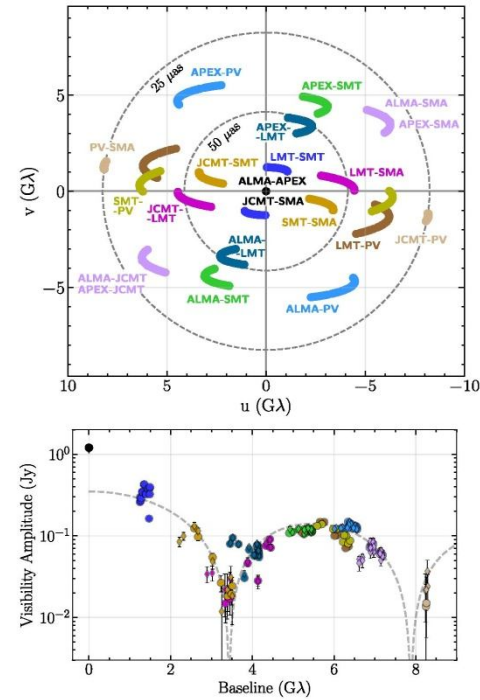


**Figure 2.** Top:  $(u, v)$  coverage for M87\*, aggregated over all four days of the observations.  $(u, v)$  coordinates for each antenna pair are the source-projected baseline length in units of the observing wavelength  $\lambda$  and are given for conjugate pairs. Baselines to ALMA/APEX and to JCMT/SMA are redundant. Dotted circular lines indicate baseline lengths corresponding to fringe spacings of 50 and 25  $\mu\text{as}$ . Bottom: final calibrated visibility amplitudes of M87\* as a function of projected baseline length on April 11. Redundant baselines to APEX and JCMT are plotted as diamonds. Error bars correspond to thermal (statistical) uncertainties. The Fourier transform of an azimuthally symmetric thin ring model with diameter 46  $\mu\text{as}$  is also shown with a dashed line for comparison.

(Greisen 2003; Whitney et al. 2004; McMullin et al. 2007, I. M. van Bemmel et al. 2019, in preparation).

Data from the fringe-fitting pipelines were scaled from correlation coefficients to a uniform physical flux density scale (in Jansky) by using an independent a priori estimate of the sensitivity of each telescope. The accuracies of the derived station sensitivities were estimated to be 5%–10% in amplitude, although certain uncharacterized losses (e.g., from poor pointing or focus) can exceed the error budget. By assuming total flux density values derived from ALMA interferometric data (Goddi et al. 2019) and utilizing array redundancy via network calibration (Paper III), we refined the absolute amplitude calibration of telescopes that are colocated and have redundant baselines, i.e., ALMA/APEX and JCMT/SMA.

The median scan-averaged signal-to-noise ratio for M87\* was  $>10$  on non-ALMA baselines and  $>100$  on baselines to ALMA, leading to small statistical errors in visibility amplitude

and phase. Comparisons between the three independent pipelines, the two polarizations, and the two frequency bands enabled estimation of systematic baseline errors of around  $1^\circ$  in visibility phase and 2% for visibility amplitudes. These small limiting errors remain after fitting station sensitivities and unknown station phases via self-calibration (Pearson & Readhead 1984) and affect interferometric closure quantities (Rogers et al. 1974; Readhead et al. 1980). Following data validation and pipeline comparisons, a single pipeline output was designated as the primary data set of the first EHT science data release and used for subsequent results, while the outputs of the other two pipelines offer supporting validation data sets.

The final calibrated complex visibilities  $V(u, v)$  correspond to the Fourier components of the brightness distribution on the sky at spatial frequency  $(u, v)$  determined by the projected baseline expressed in units of the observing wavelength (van Cittert 1934; Thompson et al. 2017). Figure 2 shows the  $(u, v)$  coverage and calibrated visibility amplitudes of M87\* for April 11. The visibility amplitudes resemble those of a thin ring (i.e., a Bessel function  $J_0$ ; see Figure 10.12 in Thompson et al. 2017). Such a ring model with diameter 46  $\mu\text{as}$  has a first null at 3.4  $G\lambda$ , matching the minimum in observed flux density and is consistent with a reduced flux density on the longest Hawai‘i–Spain baseline (JCMT/SMA–PV) near 8  $G\lambda$ . This particular ring model, shown with a dashed line in the bottom panel of Figure 2, is only illustrative and does not fit all features in the data. First, visibility amplitudes on the shortest VLBI baselines suggest that about half of the compact flux density seen on the  $\sim 2$  km ALMA–APEX baseline is resolved out by the interferometer beam (Paper IV). Second, differences in the depth of the first minimum as a function of orientation, as well as highly nonzero measured closure phases, indicate some degree of asymmetry in the source (Papers III, VI). Finally, the visibility amplitudes represent only half of the information available to us. We will next explore images and more complex geometrical models that can fit the measured visibility amplitudes and phases.

## 5. Images and Features

We reconstructed images from the calibrated EHT visibilities, which provide results that are independent of models (Paper IV). However, there are two major challenges in reconstructing images from EHT data. First, EHT baselines sample a limited range of spatial frequencies, corresponding to angular scales between 25 and 160  $\mu\text{as}$ . Because the  $(u, v)$  plane is only sparsely sampled (Figure 2), the inverse problem is under-constrained. Second, the measured visibilities lack absolute phase calibration and can have large amplitude calibration uncertainties.

To address these challenges, imaging algorithms incorporate additional assumptions and constraints that are designed to produce images that are physically plausible (e.g., positive and compact) or conservative (e.g., smooth), while remaining consistent with the data. We explored two classes of algorithms for reconstructing images from EHT data. The first class of algorithms is the traditional CLEAN approach used in radio interferometry (e.g., Högbom 1974; Clark 1980). CLEAN is an inverse-modeling approach that deconvolves the interferometer point-spread function from the Fourier-transformed visibilities. When applying CLEAN, it is necessary to iteratively self-calibrate the data between rounds of imaging to solve for time-variable phase and amplitude errors in the data. The second class of algorithms is the so-called regularized

# Thompson et al. (2017)

**Table 10.2** Visibility functions for azimuthally symmetric source distributions<sup>a</sup>

Model	$I(r)/I_0$	FWHM	$\mathcal{V}(q)/I_0$	$\mathcal{V}(0)/I_0$	$A^b$
Delta function	$\delta(r)$	–	1	–	–
Ring	$\delta(r - a)$	$2a$	$J_0(2\pi a q)$	1	$\pi^2 a^2$
Disk <sup>c</sup>	$\Pi\left(\frac{r}{a}\right)$	$2a$	$\pi a^2 \frac{J_1(2\pi a q)}{\pi a q}$	$\pi a^2$	$\frac{\pi^2}{2} a^2$
Annulus <sup>d</sup>	$\Pi\left(\frac{r}{a_2}\right) - \Pi\left(\frac{r}{a_1}\right)$	$2a_2$	$\pi a_2^2 \left[ \frac{J_1(2\pi a_2 q)}{\pi a_2 q} \right] - \pi a_1^2 \left[ \frac{J_1(2\pi a_1 q)}{\pi a_1 q} \right]$	$\pi(a_2^2 - a_1^2)$	$\frac{\pi^2}{2} \frac{a_2^4 - a_1^4}{a_2^2 - a_1^2}$
Gaussian	$e^{-r^2/2a^2}$	$\sqrt{8 \ln 2} a$	$2\pi a^2 e^{-2\pi^2 a^2 q^2}$	$2\pi a^2$	$2\pi^2 a^2$
Uniform sphere <sup>c</sup>	$\sqrt{1 - \left(\frac{r}{a}\right)^2} \Pi\left(\frac{r}{a}\right)$	$\frac{\sqrt{3}}{2} a$	$\sqrt{\frac{\pi}{2}} (2\pi a^2) \frac{J_{3/2}(2\pi a q)}{(2\pi a q)^{3/2}}$ $= \frac{2\pi a^2}{(2\pi a q)^3} [\sin(2\pi a q) - 2\pi a q \cos(2\pi a q)]$	$\frac{2\pi}{3} a^2$	$\frac{\pi^2 a^2}{4}$

<sup>a</sup>For additional models and fitting algorithms, see Lobanov (2015), Ng et al. (2008), and Martí-Vidal et al. (2014).

<sup>b</sup>Taylor expansion:  $\mathcal{V}(q) = \mathcal{V}(0)[1 - Aq^2]$ .

<sup>c</sup> $\Pi$ , modified unit rectangle function:  $\Pi(x) = 1, 0 < x \leq 1$ ;  $\Pi(x) = 0$  otherwise.

<sup>d</sup> $a_2$  = outer radius,  $a_1$  = inner radius.

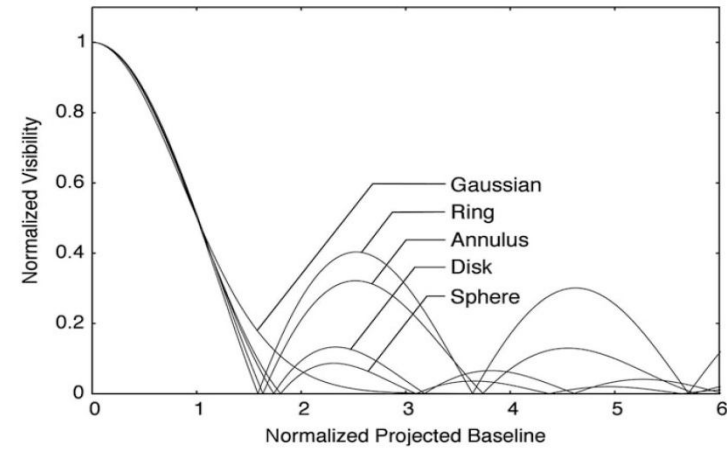


**Fig. 10.11** Normalized visibility models,  $|V|/V_0$ , vs. projected baseline length,  $q$ , for azimuthally symmetric source models described in Table 10.2.

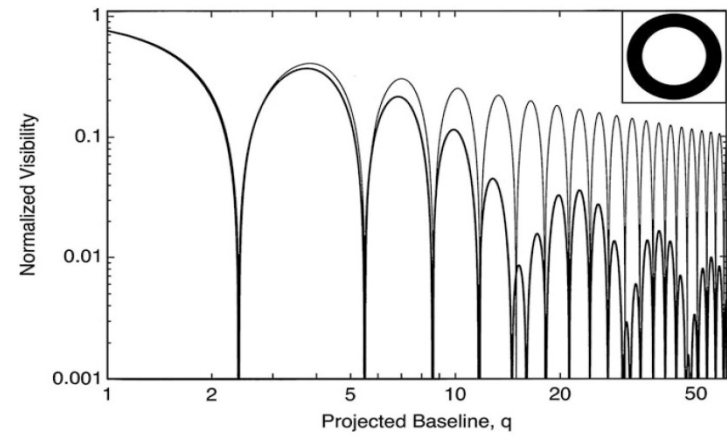


**Fig. 10.12** (thin line) Visibility amplitude for a ring source with radius 1. (thick line) Visibility amplitude for an annular source with inner and outer radii of 0.8 and 1.2, respectively. Adapted from Bracewell (2000).

- Figure 2 shows the  $(u, v)$  coverage and calibrated visibility amplitudes of M87\* for April 11. The visibility amplitudes resemble those of a thin ring (i.e., a Bessel function  $J_0$ ; see Figure 10.12 in Thompson et al. 2017). Such a ring model with diameter  $46 \mu\text{as}$  has a first null at  $3.4 G\lambda$ , matching the minimum in observed flux density and is consistent with a reduced flux density on the longest Hawai'i–Spain baseline (JCMT/SMA-PV) near  $8 G\lambda$ . This particular ring model, shown with a dashed line in the bottom panel of Figure 2, is only illustrative and does not fit all features in the data.

- EHT team explored two classes of algorithms for reconstructing images from EHT data. The first class of algorithms is the traditional CLEAN approach used in radio interferometry (e.g., Högbom 1974; Clark 1980). CLEAN is an inverse-modeling approach that deconvolves the interferometer point-spread function from the Fourier-transformed visibilities. When applying CLEAN, it is necessary to iteratively self-calibrate the data between rounds of imaging to solve for time-variable phase and amplitude errors in the data.
- The second class of algorithms is the so-called regularized maximum likelihood (RML; e.g., Narayan & Nityananda 1986; Wiaux et al. 2009; Thiébaud 2013). RML is a forward-modeling approach that searches for an image that is not only consistent with the observed data but also favors specified image properties (e.g., smoothness or compactness). As with CLEAN, RML methods typically iterate between imaging and self-calibration, although they can also be used to image directly on robust closure quantities immune to station-based calibration errors. RML methods have been extensively developed for the EHT (e.g., Honma et al. 2014; Bouman et al. 2016; Akiyama et al. 2017; Chael et al. 2018).

- There are two major challenges in reconstructing images from EHT data. First, EHT baselines sample a limited range of spatial frequencies, corresponding to angular scales between 25 and 160  $\mu\text{as}$ . Because the  $(u, v)$  plane is only sparsely sampled (Figure 2), **the inverse problem is under-constrained**. Second, the measured visibilities lack absolute phase calibration and can have large amplitude calibration uncertainties.
- To address these challenges, imaging algorithms incorporate additional assumptions and constraints that are designed to produce images that are physically plausible (e.g., positive and compact) or conservative (e.g., smooth), while remaining consistent with the data. (Similarly, for a linear incorrect problem an assumption about monotone behavior of an unknown function reduces an original problem to correct one).

- Every imaging algorithm has a variety of free parameters that can significantly affect the final image. The EHT team adopted a two stage imaging approach to control and evaluate biases in the reconstructions from our choices of these parameters. In the first stage, four teams worked independently to reconstruct the first EHT images of M87\* using an early engineering data release. The teams worked without interaction to minimize shared bias, yet each produced an image with a similar prominent feature: a ring of diameter  $\sim 38\text{--}44 \mu\text{as}$  with enhanced brightness to the south.

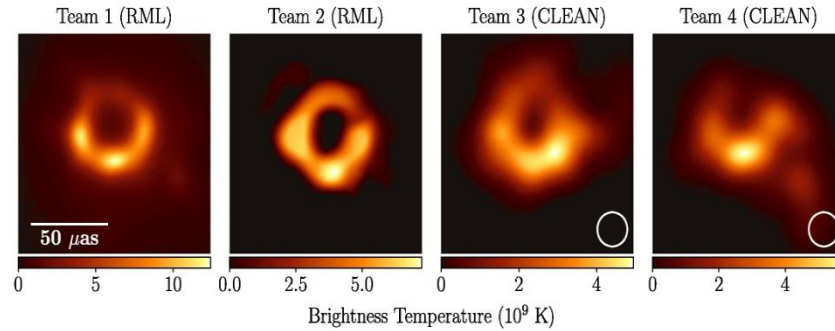


**Figure 4.** The first EHT images of M87, blindly reconstructed by four independent imaging teams using an early, engineering release of data from the April 11 observations. These images all used a single polarization (LCP) rather than Stokes  $I$ , which is used in the remainder of this Letter. Images from Teams 1 and 2 used RML methods (no restoring beam); images from Teams 3 and 4 used CLEAN (restored with a circular  $20 \mu\text{as}$  beam, shown in the lower right). The images all show similar morphology, although the reconstructions show significant differences in brightness temperature because of different assumptions regarding the total compact flux density (see Table 2) and because restoring beams are applied only to CLEAN images.

	Team 1	Team 2	Team 3	Team 4
<b>Image Properties</b>				
Method	RML	RML	CLEAN	CLEAN
$F_{\text{jet}}$ (Jy)	0.94	0.43	0.42	0.42
Engineering Data (10 s avg., LCP, 0% sys. error)				
$\chi_{\text{CP}}^2$	2.06	2.48	2.44	2.33
$\chi_{\text{log CA}}^2$	1.20	2.16	2.15	1.43
Science Release (scan-avg., Stokes $I$ , 0% sys. error)				
$\chi_{\text{CP}}^2$	1.13	5.40	2.28	1.89
$\chi_{\text{log CA}}^2$	2.12	5.41	3.90	5.32
Science Release (scan-avg., Stokes $I$ , 1% sys. error)				
$\chi_{\text{CP}}^2$	1.00	3.85	2.04	1.55
$\chi_{\text{log CA}}^2$	1.96	5.07	3.64	4.8
Science Release (scan-avg., Stokes $I$ , 10% sys. error)				
$\chi_{\text{CP}}^2$	0.49	0.95	1.11	0.48
$\chi_{\text{log CA}}^2$	0.46	1.36	0.98	0.79

**Note.** Data metrics are shown as originally computed on April 11 data (using 10 s averaged engineering data with LCP) and using the data from the first EHT science release (scan-averaged, Stokes  $I$ ) when 0%, 1% and 10% systematic error has been included. Teams 2–4 chose to exclude the intra-site baselines in their imaging. However, for consistency with our later  $\chi^2$  values computed from science release data, we include these baselines when computing  $\chi^2$  after adding an extended component to these images containing the missing flux density.

structures, including sources without the prominent ring observed in our images of M87.

We emphasize that the ensemble of results from these parameter surveys do not correspond to a posterior distribution of reconstructed images. Our surveys are coarse-grained and do not completely explore the choices in the imaging process. Nonetheless, they identify regions of imaging parameter space that consistently produce faithful image reconstructions on synthetic data, and they help us identify which features of our reconstructions are consistent and which features vary with specific parameter choices.

### 6.1. Synthetic Source Models and Data

To create a testing suite of synthetic data, we selected simple geometric models that have corresponding visibility amplitudes that are similar to those observed in M87 (Figure 2). The primary data properties that we used to define similarity are (1) a large decrease in flux density on baselines between 0 and  $1 \text{ G}\lambda$ , indicating extended structure, (2) visibility nulls at  $\sim 3.4$  and  $\sim 8.3 \text{ G}\lambda$ , and (3) a high secondary peak between the nulls at  $\sim 6 \text{ G}\lambda$ , which recovers  $\sim 15\%$  of the total compact flux density.

We selected four models with distinct compact morphologies that each reproduce these features of the M87 data. The four models are (1) a tapered ring with  $44 \mu\text{as}$  ring diameter, (2) a tapered crescent of the same diameter with its brightest point oriented directly south, (3) a tapered disk with  $70 \mu\text{as}$  diameter, and (4) two different circular Gaussian components separated by  $32.3 \mu\text{as}$  at a position angle of  $292^\circ$ . To ensure rough consistency and compatibility with the M87 parameters estimated in Section 4, we adopted a total compact flux density of  $0.6 \text{ Jy}$  for all these simple geometric models. Note that none of the synthetic EHT data sets generated from these simple models reproduces all features seen in the M87 data. For example, the ring and disk models both have point symmetry, so all their closure phases are either  $0^\circ$  or  $180^\circ$ .

To simulate the effects of a large-scale jet on our data (which only significantly affects intra-site visibilities), we added a three-component Gaussian model that approximates the inner M87 jet at  $3 \text{ mm}$  (e.g., Kim et al. 2018a). The jet also has  $0.6 \text{ Jy}$  of total flux density, giving a total image flux density in each case (compact+jet) of  $1.2 \text{ Jy}$ . To produce non-closing systematic errors from polarimetric leakage, we also included linear polarization in each model. For additional details on these simulated models and data, see Appendix C.1. Figure 5 shows these model images.

We generated synthetic data from each image using the `eht-imaging` software library. The synthetic data were produced with the baseline coverage and sensitivity of the EHT on all four days of the 2017 observations. Station-based errors were added in a Jones matrix formalism (Thompson et al. 2017; see Appendix C.2). To simulate a lack of absolute phase

- In the second imaging stage, we developed three imaging pipelines, each using a different software package and associated methodology. Each pipeline surveyed a range of imaging parameters, producing between  $\sim 10^3$  and  $10^4$  images from different parameter combinations. We determined a “Top-Set” of parameter combinations that both produced images of M87\* that were consistent with the observed data and that reconstructed accurate images from synthetic data sets corresponding to four known geometric models (ring, crescent, filled disk, and asymmetric double source). For all pipelines, the Top-Set images showed an asymmetric ring with a diameter of  $\sim 40 \mu\text{as}$ , with differences arising primarily in the effective angular resolutions achieved by different methods.

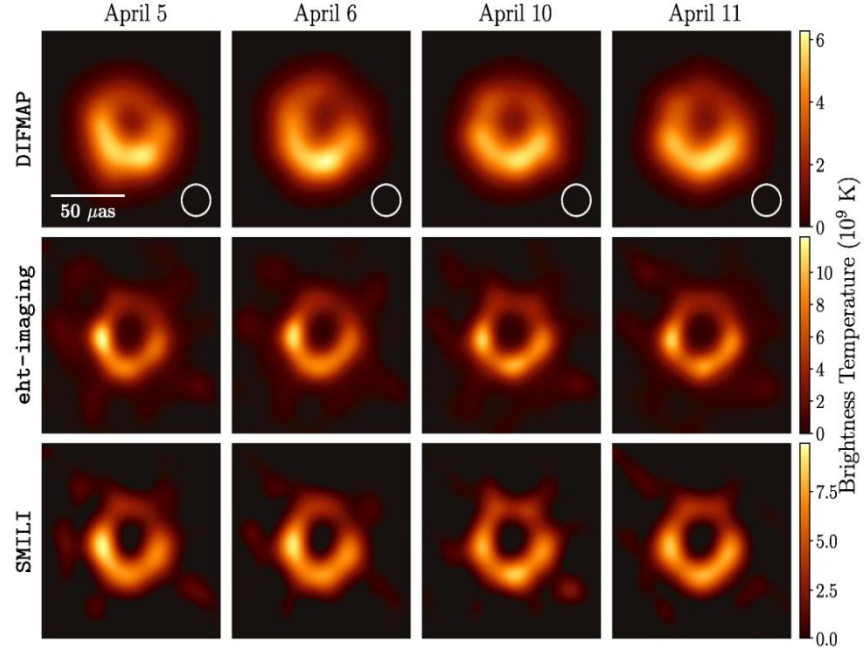


**Figure 11.** Fiducial images of M87 on all four observed days from each of the three imaging pipelines. CLEAN images (from DIFMAP) are shown after convolution with a  $20 \mu\text{as}$  beam; *eht-imaging* and SMILI results have no restoring beam applied. Different selected fiducial imaging parameters (e.g., compact flux) result in different peak brightness temperatures for each method, as indicated by the unique color bars for each row.

**Table 4**  
Equivalent Blurring Values  $\alpha$  from the Fiducial and Top Set Images from Each Pipeline on Each of the Four Simple Geometric Models in the Training Set

	$\alpha$ ( $\mu\text{as}$ ), Ring			$\alpha$ ( $\mu\text{as}$ ), Crescent			$\alpha$ ( $\mu\text{as}$ ), Disk			$\alpha$ ( $\mu\text{as}$ ), Double		
	Fiducial	Mean	Std. Dev.	Fiducial	Mean	Std. Dev.	Fiducial	Mean	Std. Dev.	Fiducial	Mean	Std. Dev.
DIFMAP	19.4	21.2	1.5	19.0	21.6	1.5	18.5	21.2	2.1	19.8	21.6	1.5
<i>eht-imaging</i>	9.4	13.4	3.3	9.3	12.2	1.8	18.0	20.5	2.0	11.3	15.8	3.4
SMILI	10.6	12.2	2.8	10.6	12.2	2.3	12.3	18.7	3.1	11.3	14.8	3.4

**Note.** For each pipeline, we give  $\alpha$  for the fiducial image, as well as the mean and standard deviation of  $\alpha$  across the Top Set.

expected from differences in the underlying methods. For instance, the prior and mask sizes are treated differently in different scripts: a hard mask was used for DIFMAP, a softer mask for SMILI, and only weak constraints on compactness were used for *eht-imaging*. However, other choices are unexpected. For example, the top-ranked parameter combinations (i.e., the fiducial parameters) for the DIFMAP and SMILI pipelines use a total compact flux density of 0.5 Jy, favoring this value over the true total compact flux density of 0.6 Jy. However, these preferences are mild, and the Top Set from each pipeline includes images with all values of total compact flux density surveyed, from 0.4 to 0.8 Jy (see Table 3). We explore the dependence of the assumed compact flux density in Appendix H.

## 7. Fiducial M87 Images: Properties and Uncertainties

Having determined fiducial imaging parameters via tests on synthetic data (Section 6.3.1), we now show the corresponding fiducial M87 images from each imaging method for each day of the 2017 EHT observations. We also assess the consistency of the fiducial images with the data, discuss other visibility-domain properties of these images, and estimate image uncertainties resulting from imaging parameter choices.

### 7.1. Fiducial M87 Images

Figure 11 shows the fiducial images from each day of EHT observations and each imaging method. These fiducial images are broadly consistent; all twelve images have a prominent,

- For each pipeline, we determined the single combination of fiducial imaging parameters out of the Top-Set that performed best across all the synthetic data sets and for each associated imaging methodology (see Figure 11 in Paper IV). Because the angular resolutions of the reconstructed images vary among the pipelines, we blurred each image with a circular Gaussian to a common, conservative angular resolution of  $20 \mu\text{as}$ . The top part of Figure 3 shows an image of M87\* on April 11 obtained by averaging the three pipelines' blurred fiducial images. The image is dominated by a ring with an asymmetric azimuthal profile that is oriented at a position angle  $\sim 170^\circ$  east of north. Although the measured position angle increases by  $\sim 20^\circ$  between the first two days and the last two days, the image features are broadly consistent across the different imaging methods and across all four observing days.

maximum likelihood (RML; e.g., Narayan & Nityananda 1986; Wiaux et al. 2009; Thiébaud 2013). RML is a forward-modeling approach that searches for an image that is not only consistent with the observed data but also favors specified image properties (e.g., smoothness or compactness). As with CLEAN, RML methods typically iterate between imaging and self-calibration, although they can also be used to image directly on robust closure quantities immune to station-based calibration errors. RML methods have been extensively developed for the EHT (e.g., Honma et al. 2014; Bouman et al. 2016; Akiyama et al. 2017; Chael et al. 2018b; see also Paper IV).

Every imaging algorithm has a variety of free parameters that can significantly affect the final image. We adopted a two-stage imaging approach to control and evaluate biases in the reconstructions from our choices of these parameters. In the first stage, four teams worked independently to reconstruct the first EHT images of M87\* using an early engineering data release. The teams worked without interaction to minimize shared bias, yet each produced an image with a similar prominent feature: a ring of diameter  $\sim 38\text{--}44 \mu\text{as}$  with enhanced brightness to the south (see Figure 4 in Paper IV).

In the second imaging stage, we developed three imaging pipelines, each using a different software package and associated methodology. Each pipeline surveyed a range of imaging parameters, producing between  $\sim 10^3$  and  $10^4$  images from different parameter combinations. We determined a “Top-Set” of parameter combinations that both produced images of M87\* that were consistent with the observed data and that reconstructed accurate images from synthetic data sets corresponding to four known geometric models (ring, crescent, filled disk, and asymmetric double source). For all pipelines, the Top-Set images showed an asymmetric ring with a diameter of  $\sim 40 \mu\text{as}$ , with differences arising primarily in the effective angular resolutions achieved by different methods.

For each pipeline, we determined the single combination of fiducial imaging parameters out of the Top-Set that performed best across all the synthetic data sets and for each associated imaging methodology (see Figure 11 in Paper IV). Because the angular resolutions of the reconstructed images vary among the pipelines, we blurred each image with a circular Gaussian to a common, conservative angular resolution of  $20 \mu\text{as}$ . The top part of Figure 3 shows an image of M87\* on April 11 obtained by averaging the three pipelines’ blurred fiducial images. The image is dominated by a ring with an asymmetric azimuthal profile that is oriented at a position angle  $\sim 170^\circ$  east of north. Although the measured position angle increases by  $\sim 20^\circ$  between the first two days and the last two days, the image features are broadly consistent across the different imaging methods and across all four observing days. This is shown in the bottom part of Figure 3, which reports the images on different days (see also Figure 15 in Paper IV). These results are also consistent with those obtained from visibility-domain fitting of geometric and general-relativistic magnetohydrodynamics (GRMHD) models (Paper VI).

## 6. Theoretical Modeling

The appearance of M87\* has been modeled successfully using GRMHD simulations, which describe a turbulent, hot, magnetized disk orbiting a Kerr black hole. They naturally produce a powerful jet and can explain the broadband spectral energy distribution observed in LLAGNs. At a wavelength of 1.3 mm, and as observed here, the simulations also predict a shadow and an asymmetric emission ring. The latter does not necessarily coincide

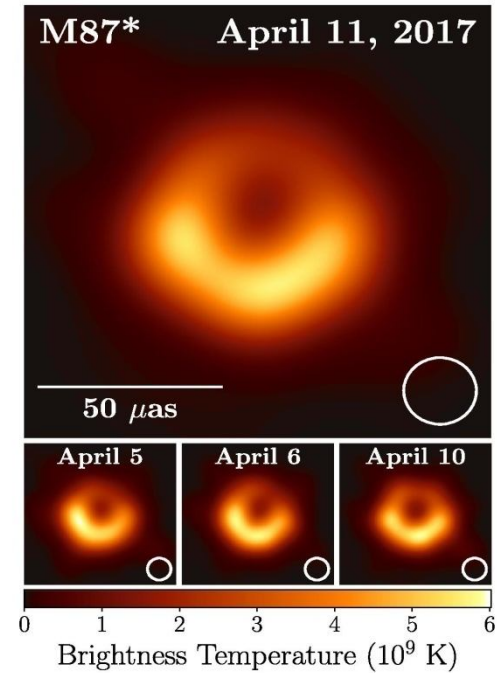


**Figure 3.** Top: EHT image of M87\* from observations on 2017 April 11 as a representative example of the images collected in the 2017 campaign. The image is the average of three different imaging methods after convolving each with a circular Gaussian kernel to give matched resolutions. The largest of the three kernels ( $20 \mu\text{as}$  FWHM) is shown in the lower right. The image is shown in units of brightness temperature,  $T_b = S\lambda^2/2k_B\Omega$ , where  $S$  is the flux density,  $\lambda$  is the observing wavelength,  $k_B$  is the Boltzmann constant, and  $\Omega$  is the solid angle of the resolution element. Bottom: similar images taken over different days showing the stability of the basic image structure and the equivalence among different days. North is up and east is to the left.

with the innermost stable circular orbit, or ISCO, and is instead related to the lensed photon ring. To explore this scenario in great detail, we have built a library of synthetic images (Image Library) describing magnetized accretion flows onto black holes in GR<sup>145</sup> (Paper V). The images themselves are produced from a library of simulations (Simulation Library) collecting the results of four codes solving the equations of GRMHD (Gammie et al. 2003; Sądowski et al. 2014; Porth et al. 2017; Liska et al. 2018). The elements of the Simulation Library have been coupled to three different general-relativistic ray-tracing and radiative-transfer codes (GRRT, Bronzwaer et al. 2018; Mościbrodzka & Gammie 2018; Z. Younsi et al. 2019, in preparation). We limit ourselves to providing here a brief description of the initial setups and the physical scenarios explored in the simulations; see Paper V for details on both the GRMHD and GRRT codes, which have been cross-validated

<sup>145</sup> More exotic spacetimes, such as dilaton black holes, boson stars, and gravastars, have also been considered (Paper V).

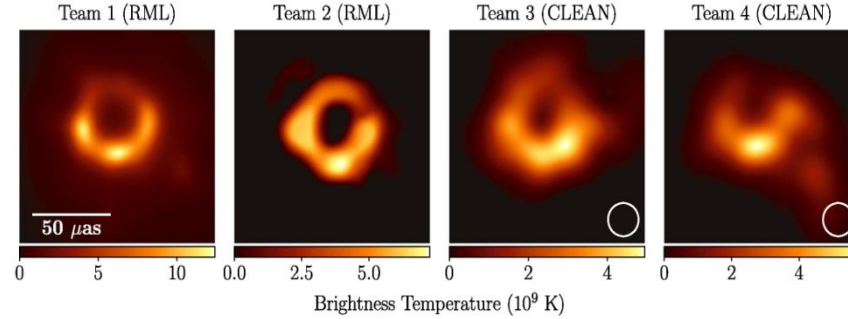


**Figure 4.** The first EHT images of M87, blindly reconstructed by four independent imaging teams using an early, engineering release of data from the April 11 observations. These images all used a single polarization (LCP) rather than Stokes  $I$ , which is used in the remainder of this Letter. Images from Teams 1 and 2 used RML methods (no restoring beam); images from Teams 3 and 4 used CLEAN (restored with a circular  $20 \mu\text{as}$  beam, shown in the lower right). The images all show similar morphology, although the reconstructions show significant differences in brightness temperature because of different assumptions regarding the total compact flux density (see Table 2) and because restoring beams are applied only to CLEAN images.

**Table 2**  
Image Properties and Data Consistency Metrics  
for the First M87 Images (See Figure 4)

	Team 1	Team 2	Team 3	Team 4
Image Properties				
Method	RML	RML	CLEAN	CLEAN
$F_{\text{opt}}$ (Jy)	0.94	0.43	0.42	0.42
Engineering Data (10 s avg., LCP, 0% sys. error)				
$\chi_{\text{CP}}^2$	2.06	2.48	2.44	2.33
$\chi_{\text{log CA}}^2$	1.20	2.16	2.15	1.43
Science Release (scan-avg., Stokes $I$ , 0% sys. error)				
$\chi_{\text{CP}}^2$	1.13	5.40	2.28	1.89
$\chi_{\text{log CA}}^2$	2.12	5.41	3.90	5.32
Science Release (scan-avg., Stokes $I$ , 1% sys. error)				
$\chi_{\text{CP}}^2$	1.00	3.85	2.04	1.55
$\chi_{\text{log CA}}^2$	1.96	5.07	3.64	4.8
Science Release (scan-avg., Stokes $I$ , 10% sys. error)				
$\chi_{\text{CP}}^2$	0.49	0.95	1.11	0.48
$\chi_{\text{log CA}}^2$	0.46	1.36	0.98	0.79

**Note.** Data metrics are shown as originally computed on April 11 data (using 10 s averaged engineering data with LCP) and using the data from the first EHT science release (scan-averaged, Stokes  $I$ ) when 0%, 1% and 10% systematic error has been included. Teams 2–4 chose to exclude the intra-site baselines in their imaging. However, for consistency with our later  $\chi^2$  values computed from science release data, we include these baselines when computing  $\chi^2$  after adding an extended component to these images containing the missing flux density.

structures, including sources without the prominent ring observed in our images of M87.

We emphasize that the ensemble of results from these parameter surveys do not correspond to a posterior distribution of reconstructed images. Our surveys are coarse-grained and do not completely explore the choices in the imaging process. Nonetheless, they identify regions of imaging parameter space that consistently produce faithful image reconstructions on synthetic data, and they help us identify which features of our reconstructions are consistent and which features vary with specific parameter choices.

### 6.1. Synthetic Source Models and Data

To create a testing suite of synthetic data, we selected simple geometric models that have corresponding visibility amplitudes that are similar to those observed in M87 (Figure 2). The primary data properties that we used to define similarity are (1) a large decrease in flux density on baselines between 0 and  $1 \text{ G}\lambda$ , indicating extended structure, (2) visibility nulls at  $\sim 3.4$  and  $\sim 8.3 \text{ G}\lambda$ , and (3) a high secondary peak between the nulls at  $\sim 6 \text{ G}\lambda$ , which recovers  $\sim 15\%$  of the total compact flux density.

We selected four models with distinct compact morphologies that each reproduce these features of the M87 data. The four models are (1) a tapered ring with  $44 \mu\text{as}$  ring diameter, (2) a tapered crescent of the same diameter with its brightest point oriented directly south, (3) a tapered disk with  $70 \mu\text{as}$  diameter, and (4) two different circular Gaussian components separated by  $32.3 \mu\text{as}$  at a position angle of  $292^\circ$ . To ensure rough consistency and compatibility with the M87 parameters estimated in Section 4, we adopted a total compact flux density of  $0.6 \text{ Jy}$  for all these simple geometric models. Note that none of the synthetic EHT data sets generated from these simple models reproduces all features seen in the M87 data. For example, the ring and disk models both have point symmetry, so all their closure phases are either  $0^\circ$  or  $180^\circ$ .

To simulate the effects of a large-scale jet on our data (which only significantly affects intra-site visibilities), we added a three-component Gaussian model that approximates the inner M87 jet at  $3 \text{ mm}$  (e.g., Kim et al. 2018a). The jet also has  $0.6 \text{ Jy}$  of total flux density, giving a total image flux density in each case (compact+jet) of  $1.2 \text{ Jy}$ . To produce non-closing systematic errors from polarimetric leakage, we also included linear polarization in each model. For additional details on these simulated models and data, see Appendix C.1. Figure 5 shows these model images.

We generated synthetic data from each image using the `eht-imaging` software library. The synthetic data were produced with the baseline coverage and sensitivity of the EHT on all four days of the 2017 observations. Station-based errors were added in a Jones matrix formalism (Thompson et al. 2017; see Appendix C.2). To simulate a lack of absolute phase

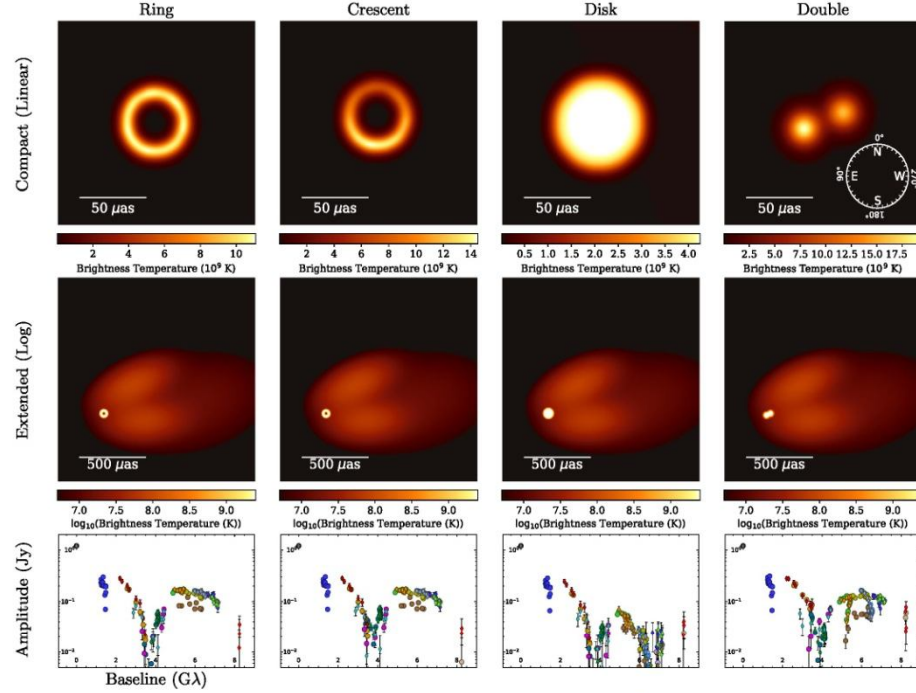


**Figure 5.** The four simple geometric models and synthetic data sets used in the parameter surveys (see Appendix C for details). Top: linear scale images, highlighting the compact structure of the models. Middle: logarithmic scale images, highlighting the larger-scale jet added to each model image. Bottom: one realization of simulated visibility amplitudes corresponding to the April 11 observations of M87. We indicate the conventions for cardinal direction and position angle used throughout this Letter on the upper-right panel. Note that east is oriented to the left, and position angles are defined east of north.

calibration, a random station phase is adopted for each scan. Independent station-based gains were applied to each visibility, with two components of each gain factor drawn from normal distributions: one term that was constant over the observation, and one that varied randomly among scans. We captured the increased uncertainty and variability in station gains at the LMT (Section 4.1) by giving these gain terms larger variances. Time-independent polarimetric leakage terms were drawn from a complex Gaussian distribution with 5% standard deviation, motivated by previous estimates of the polarization leakage at EHT sites (Johnson et al. 2015). Identical gain, phase, and leakage contamination was applied to the high- and low-band data. Figure 5 shows four examples of visibility amplitudes generated using this procedure. Appendix C.2 provides full details about the synthetic data generation procedure.

Furthermore, to test whether or not our results are sensitive to specific choices made in the synthetic data generation, we compared our generated synthetic data and reconstructed images to results from another VLBI data simulator, `Meq-Silhouette+rPICARD` (Blecher et al. 2017; Janssen et al. 2019). `MeqSilhouette+rPICARD` takes a more physical approach to mm-VLBI synthetic data generation (with added corruption based on, e.g., measured weather parameters and

antenna pointing offsets) and it uses the full `CASA`-based EHT reduction pipeline for calibration. Despite the differences in approach, both synthetic data pipelines yield comparable results (see Appendix C.3 and Figure 31). We use `eht-imaging` for all further synthetic data in this Letter.

## 6.2. Imaging Pipelines and Parameter Survey Space

To survey the space of imaging parameters relevant to each imaging software package and to test their effects on reconstructions of simulated data, we designed scripted imaging pipelines in three software packages: `DIFMAP`, `eht-imaging`, and `SMILI`. Each pipeline has some choices that are fixed (e.g., the convergence criterion, the pixel size, etc.) but takes additional parameters (e.g., the regularizer weights, the total compact flux density) as arguments. We then reconstructed images from all M87 and synthetic data sets using all possible parameter combinations on a coarse grid in the space of these parameters. We chose large ranges for each parameter, deliberately including values that we expected to produce poor reconstructions.

The parameter choices and the values surveyed vary among the three pipelines, and the pipelines also differ in which frequency

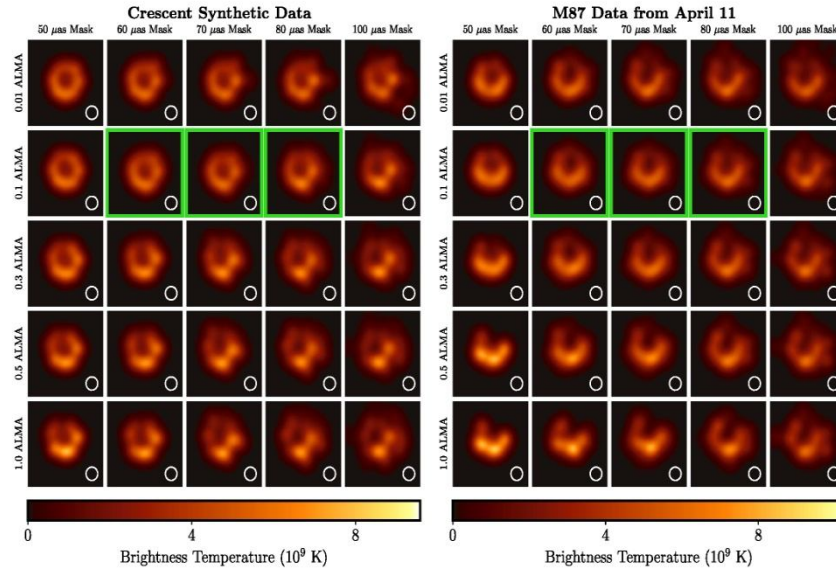


**Figure 6.** Selection of the DIFMAP (CLEAN) parameter survey results on real and synthetic data with April 11 EHT baseline coverage. A 2D slice of the 5D parameter space is displayed, corresponding to different diameters of the circular mask and the data weight on ALMA in self-calibration. All other parameters are kept constant (Compact Flux = 0.5 Jy,  $\kappa = -1$ , Stop Condition = Flux Reached). The left panel shows results of the parameter search on the Crescent synthetic data, while the right panel shows reconstructions for the same parameters on M87 data. Images that meet the threshold for the Top Set are outlined in green (see Section 6.3.1).

thereby accounting for small, non-closing systematic errors from, e.g., polarimetric leakage. We surveyed values of 0%, 1%, 2%, and 5% in computing this additional systematic uncertainty. Note that these levels of systematic uncertainty do not necessarily correspond with the estimated level of non-closing errors presented in Paper III; however, additional systematic uncertainty beyond the a priori estimate can help in avoiding overfitting to a few sensitive baselines (e.g., those to ALMA) during image optimization.

The final pre-imaging step is to *inverse taper* the visibility amplitudes. Specifically, we divide the visibility amplitudes and their estimated error by the Fourier transform of a  $5 \mu\text{as}$  FWHM Gaussian, thereby raising the amplitudes on long baselines while preserving the S/N. At the end of the script, after producing an image from the inverse-tapered data, we convolve the reconstructed image with a  $5 \mu\text{as}$  FWHM Gaussian to ensure that it will fit the original, untapered data. This procedure enforces a limiting angular resolution of  $5 \mu\text{as}$  in the final reconstructed images.

After the data have been prepared, the `eht-imaging` script proceeds to imaging, using a  $64 \times 64$  pixel grid with a  $128 \mu\text{as}$  FOV. The script alternates between solving for the optimal image under the current data constraints and self-calibrating the complex station gains (Equation (7)). The first imaging iteration uses only visibility amplitudes and closure quantities. Because the amplitudes are uncalibrated in this iteration, systematic error tolerance is added on top of the (potentially inflated) thermal uncertainty for the visibility amplitudes, using the systematic error budget provided in Paper III for all sites

except LMT, which has its budget increased by 15%. After phase self-calibration, complex visibilities are used for optimization in combination with closure quantities.

Between imaging iterations, the image is convolved with a circular Gaussian with a FWHM corresponding to the nominal array resolution,  $\lambda/|u|_{\text{max}} \approx 25 \mu\text{as}$ . This procedure aids convergence to a global minimum by moving intermediate images away from local minima. In each iteration, we increase the weight on data terms relative to the regularizers and reduce the systematic noise tolerance for amplitude calibration uncertainties. The final reconstructed image is convolved with the same  $5 \mu\text{as}$  Gaussian that was used for the inverse taper, ensuring consistency with the original data while imposing a constraint that no features in the reconstructed image can be finer than  $5 \mu\text{as}$ .

Figure 7 shows a 2D slice of the `eht-imaging` parameter survey results from varying the weights on the MEM and the TV regularizers. In this figure, we show the results for both synthetic data from a crescent model and for EHT M87 data from April 11.

### 6.2.3. SMILI

In the SMILI imaging pipeline, we reconstructed images using low-band EHT data and utilized weighted- $\ell_1$  ( $\ell_1^w$ ), TV, and TSV regularizers (see Appendix A).  $\ell_1^w$  favors sparsity in the image domain, using a circular Gaussian prior image as a “soft mask,” which increasingly penalizes pixel intensities farther from the image center. In contrast, TV favors sparsity in the gradient domain (leading to piecewise-smooth images), and TSV favors overall image smoothness. The SMILI search

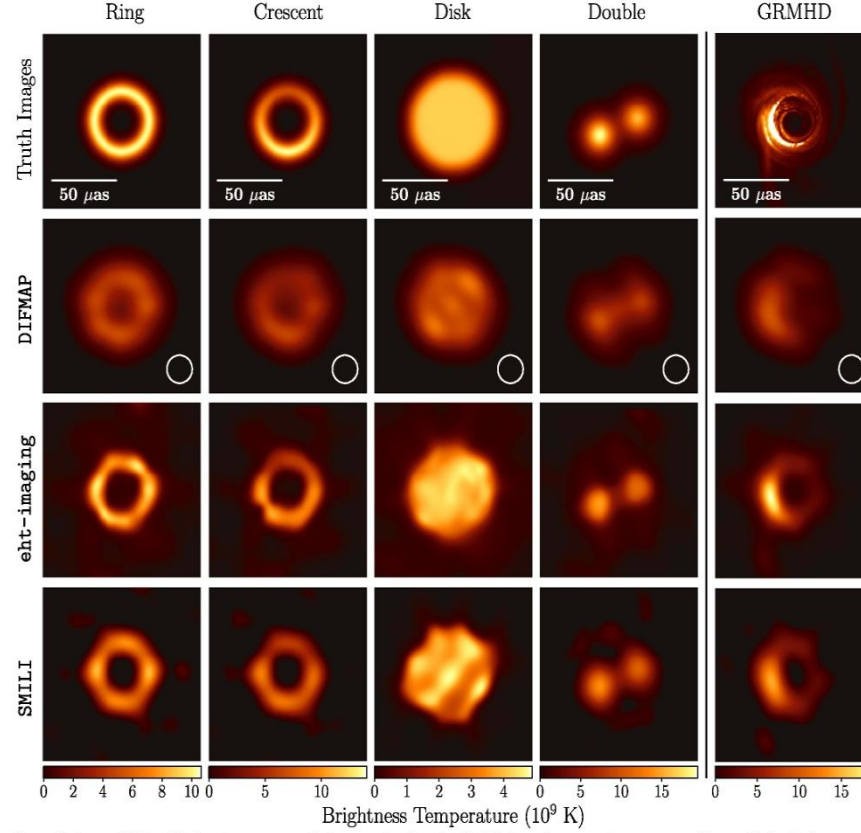


**Figure 10.** Cross-validation of the imaging parameter selection procedure. In each of the left four columns, we show reconstructed images for the simple geometric source models. These reconstructions do not use the fiducial imaging parameters identified by the full training set; instead, we selected the imaging parameters for each geometric source model after excluding that particular model from the parameter selection process. For example, in the disk reconstructions, the parameters were selected by assessing reconstructions of only the ring, crescent, and double source models. Thus, the selected parameters vary among these four columns, but we can verify that the training sets do not overly constrain the outcomes. In the fifth column, we show reconstructions of a GRMHD snapshot (Paper V) using the fiducial M87 parameters selected from all four geometric models. That is, the script and parameters used to produce these GRMHD image reconstructions are identical to those used to produce our fiducial M87 images (shown in Figure 11). Because the GRMHD snapshot has a substantially higher peak brightness than the reconstructions, its column has been scaled to the peak brightness of the *eht-imaging* reconstruction.

where the sum is over all  $N$  pixels in the two images,  $\langle X \rangle$  and  $\langle Y \rangle$  are the mean pixel values in the images, and  $\sigma_X$  and  $\sigma_Y$  are the standard deviations of the pixel values in the two images. The normalized cross-correlation quantifies image similarity, where a value of 1 implies perfect correlation between images, 0 implies no correlation, and  $-1$  implies perfect anti-correlation. Because the absolute visibility phase is unknown and, thus, the image centroid for reconstructions is not fixed, we compute  $\rho_{NX}$  for each possible discrete shift between the images and select the largest value. Before computing  $\rho_{NX}$  for DIFMAP images, the CLEAN components are convolved with a restoring beam with FWHM of  $20 \mu\text{as}$ .

We choose the median value of  $\rho_{NX}$  across all days as the representative value for a given combination of imaging parameters on a particular model. Taking the median allows us to incorporate days with different baseline coverage in the scoring procedure while preventing the poorest reconstructions (e.g., those on April 10) from dominating the outcome.

While  $\rho_{NX}$  is a useful measure of relative agreement among images, it does not provide an absolute score of reconstruction quality. For instance, Figure 9 shows that convolving the four geometric source models with the same circular Gaussian of FWHM  $\alpha$  produces  $\rho_{NX}$  values (computed against the original image) that are different depending on the underlying model. Thus, to better standardize the interpretation of  $\rho_{NX}$  for

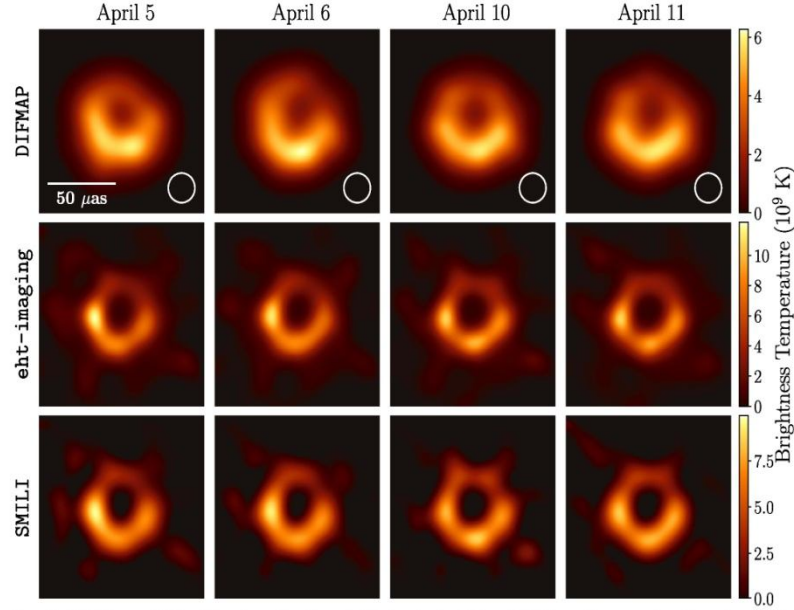


**Figure 11.** Fiducial images of M87 on all four observed days from each of the three imaging pipelines. CLEAN images (from DIFMAP) are shown after convolution with a  $20 \mu\text{as}$  beam; *eht-imaging* and SMILI results have no restoring beam applied. Different selected fiducial imaging parameters (e.g., compact flux) result in different peak brightness temperatures for each method, as indicated by the unique color bars for each row.

**Table 4**  
Equivalent Blurring Values  $\alpha$  from the Fiducial and Top Set Images from Each Pipeline on Each of the Four Simple Geometric Models in the Training Set

	$\alpha$ ( $\mu\text{as}$ ), Ring			$\alpha$ ( $\mu\text{as}$ ), Crescent			$\alpha$ ( $\mu\text{as}$ ), Disk			$\alpha$ ( $\mu\text{as}$ ), Double		
	Fiducial	Mean	Std. Dev.	Fiducial	Mean	Std. Dev.	Fiducial	Mean	Std. Dev.	Fiducial	Mean	Std. Dev.
DIFMAP	19.4	21.2	1.5	19.0	21.6	1.5	18.5	21.2	2.1	19.8	21.6	1.5
<i>eht-imaging</i>	9.4	13.4	3.3	9.3	12.2	1.8	18.0	20.5	2.0	11.3	15.8	3.4
SMILI	10.6	12.2	2.8	10.6	12.2	2.3	12.3	18.7	3.1	11.3	14.8	3.4

**Note.** For each pipeline, we give  $\alpha$  for the fiducial image, as well as the mean and standard deviation of  $\alpha$  across the Top Set.

expected from differences in the underlying methods. For instance, the prior and mask sizes are treated differently in different scripts: a hard mask was used for DIFMAP, a softer mask for SMILI, and only weak constraints on compactness were used for *eht-imaging*. However, other choices are unexpected. For example, the top-ranked parameter combinations (i.e., the fiducial parameters) for the DIFMAP and SMILI pipelines use a total compact flux density of  $0.5 \text{ Jy}$ , favoring this value over the true total compact flux density of  $0.6 \text{ Jy}$ . However, these preferences are mild, and the Top Set from each pipeline includes images with all values of total compact flux density surveyed, from  $0.4$  to  $0.8 \text{ Jy}$  (see Table 3). We explore the dependence of the assumed compact flux density in Appendix H.

## 7. Fiducial M87 Images: Properties and Uncertainties

Having determined fiducial imaging parameters via tests on synthetic data (Section 6.3.1), we now show the corresponding fiducial M87 images from each imaging method for each day of the 2017 EHT observations. We also assess the consistency of the fiducial images with the data, discuss other visibility-domain properties of these images, and estimate image uncertainties resulting from imaging parameter choices.

### 7.1. Fiducial M87 Images

Figure 11 shows the fiducial images from each day of EHT observations and each imaging method. These fiducial images are broadly consistent; all twelve images have a prominent,

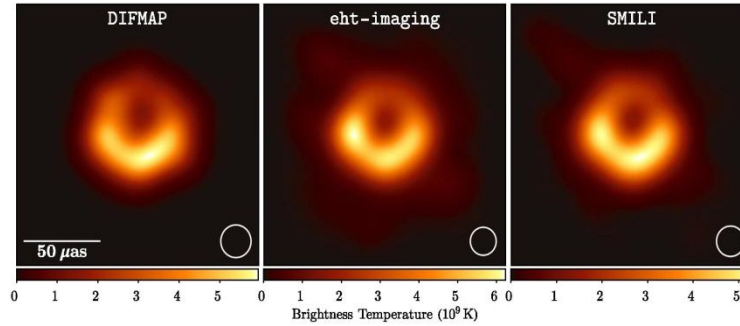


**Figure 14.** Fiducial images of M87 on April 11 from our three separate imaging pipelines after restoring each to an equivalent resolution. The *eht-imaging* and *SMILI* images have been restored with 17.1 and 18.6  $\mu\text{s}$  FWHM Gaussian beams, respectively, to match the resolution of the *DIFMAP* reconstruction restored with a 20  $\mu\text{s}$  beam.

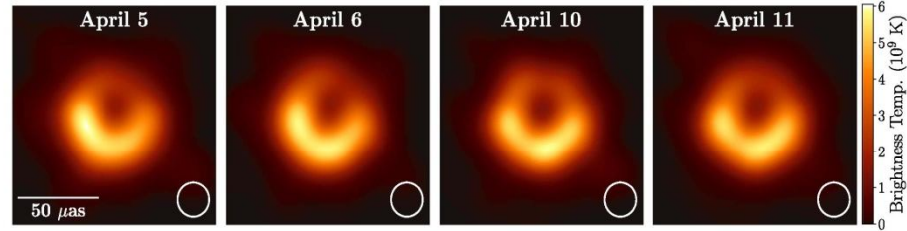


**Figure 15.** Averages of the three fiducial images of M87 for each of the four observed days after restoring each to an equivalent resolution, as in Figure 14. The indicated beam is 20  $\mu\text{s}$  (i.e., that of *DIFMAP*, which is always the largest of the three individual beams).

Figure 15 as a conservative representation of our final M87 imaging results.

The fiducial images from each pipeline (Figure 11), as well as the conservative, blurred, pipeline-averaged images (Figure 15) provide some evidence for evolution in the ring structure between April 5, 6 and 10, 11. We discuss this evolution in more detail in Appendix E (Figure 33). Some change in the image structure between April 5, 6 and 10, 11 is necessitated by the variations seen in the underlying closure phases (Paper III). We find more variation in the image pairs that are separated by larger intervals, suggesting that these variations are intrinsic. However, we cannot unambiguously associate the observed variability with coherent evolution of a specific image feature.

Figure 16 shows the visibility amplitude and phase for each of the three April 11 fiducial images as a function of vector baseline. Note that no restoring beam is required for CLEAN in this visibility-domain analysis. Each image produces nulls in the visibility amplitude near the SMA–SMT baseline, consistent with the observed amplitudes (see Figure 2). The visibility phase shows rapid swings at these nulls. The visibilities of the images from the different pipelines are most similar near the EHT measurements, as expected. On longer baselines than those sampled by the EHT, the *DIFMAP* image produces much higher visibility amplitudes than those of the

*eht-imaging* and *SMILI* images, as expected from the fact that the *DIFMAP* image is fundamentally a collection of point sources.

## 7.2. Image Uncertainties

Measuring the variation in images produced in a parameter survey Top Set allows us to evaluate image uncertainties due to the explored imaging choices. Figure 17 shows uncertainties related to imaging assumptions from the largest Top Set (that of the *eht-imaging* parameter survey) on April 11 data.

Reconstructed image uncertainties are concentrated in the regions with enhanced brightness, notably in the three “knots” in the lower half of the ring (Figure 17; top panel). These are also the regions that show the most variation among different imaging methods (Appendix I compares their azimuthal profiles). Visibility-domain modeling provides another method to assess image structure. In Paper VI, we explore fitting simple crescent models to the data. For instance, a crescent with a brightness gradient and blurring reproduces the north–south asymmetry in images without additional azimuthal structure (the “blurred and slashed with LSG” crescent of Paper VI). However, this model gives  $\chi^2_{\text{CP}}$  between 3.2 and 11.5 and  $\chi^2_{\text{log CA}}$  between 2.2 and 6.6 for different days and bands when assuming 0% systematic error (compare with Table 5). Adding additional degrees of freedom in the form of three additional Gaussian components to the crescent

# Theoretical Modeling

- The appearance of M87\* has been modeled successfully using GRMHD simulations, which describe a turbulent, hot, magnetized disk orbiting a Kerr black hole. They naturally produce a powerful jet and can explain the broadband spectral energy distribution observed in LLAGNs. At a wavelength of 1.3 mm, and as observed here, the simulations also predict a shadow and an asymmetric emission ring. To explore this scenario in great detail, we have built a library of synthetic images (Image Library) describing magnetized accretion flows onto black holes in GR. The images themselves are produced from a library of simulations (Simulation Library) collecting the results of four codes solving the equations of GRMHD (Gammie et al. 2003; Sądowski et al. 2014; Porth et al. 2017; Liska et al. 2018). The elements of the Simulation Library have been coupled to three different general-relativistic ray-tracing and radiative-transfer codes (GRRT, Bronzwaer et al. 2018; Mościbrodzka & Gammie 2018; Z. Younsi et al. 2019, in preparation).



- A typical GRMHD simulation in the library is characterized by two parameters: the dimensionless spin  $a_* = Jc^2/(GM^2)$ , where  $J$  and  $M$  are, respectively, the spin angular momentum and mass of the black hole, and  $\varphi$  is power of the magnetic flux over the mass flux event horizon ( $\phi = \Phi / (M \cdot c^2)$ ).

- These two parameters allow us to describe accretion disks that are either prograde ( $a_* > 0$ ) or retrograde ( $a_* < 0$ ) with respect to the black hole spin axis, and whose accretion flows are either “SANE” (from “Standard and Normal Evolution,” Narayan et al. 2012) with  $\phi \sim 1$ , or “MAD” (from “Magnetically Arrested Disk,” Narayan et al. 2003) with  $\phi \sim 15$ .
- Varying  $a_*$  and  $\phi$ , the EHT team have performed 43 high-resolution, three-dimensional and long-term simulations covering well the physical properties of magnetized accretion flows onto Kerr black holes.

- Because the photons at 1.3mm wavelength observed by the EHT are believed to be produced by synchrotron emission, whose absorption and emission coefficients depend on the electron distribution function, we consider the plasma to be composed of electrons and ions that have the same temperature in the magnetically dominated regions of the flow (funnel), but have a substantially different temperature in the gas dominated regions (disk midplane). In particular, we consider the plasma to be composed of nonrelativistic ions with temperature  $T_i$  and relativistic electrons with temperature  $T_e$ . A simple prescription for the ratio of the temperatures of the two species can then be imposed in terms of a single parameter (Mościbrodzka et al. 2016), such that the bulk of the emission comes either from weakly magnetized (small  $R_{high}$ ,  $T_e = T_i / R_{high}$ ) or strongly magnetized (large  $R_{high}$ ,  $T_e = T_i$ ) regions. In SANE models, the disk (jet) is weakly (strongly) magnetized, so that low (high)  $R_{high}$  models produce most of the emission in the disk (jet). MAD models, there are strongly magnetized regions everywhere and the emission is mostly from the disk midplane. While this prescription is not the only one possible, it has the advantage of being simple, sufficiently generic, and robust.

- Since each GRMHD simulation can be used to describe several different physical scenarios by changing the prescribed electron distribution function, we have used the Simulation Library to generate more than 420 different physical scenarios. Each scenario is then used to generate hundreds of snapshots at different times in the simulation leading to more than 62,000 objects in the Image Library.
- As an example, the top row of Figure 4 shows three GRMHD model snapshots from the Image Library with different spins and flow type, which fitted closure phases and amplitudes of the April 11 data best.
- In Fig. 4 (bottom): the same theoretical models, processed through a VLBI simulation pipeline with the same schedule, telescope characteristics, and weather parameters as in the April 11 run and imaged in the same way as Figure 3. Note that although the fit to the observations is equally good in the three cases, they refer to radically different physical scenarios; this highlights that a single good fit does not imply that a model is preferred over others

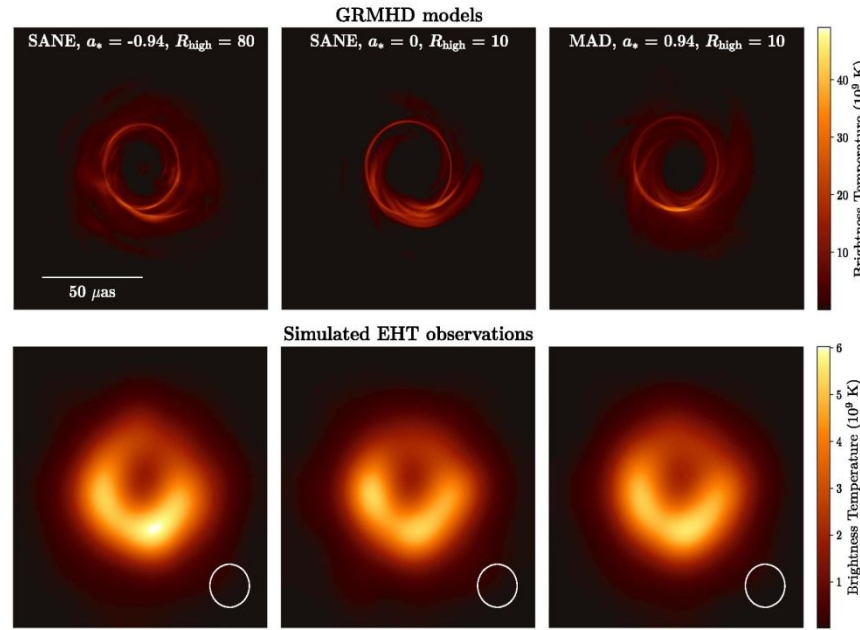


**Figure 4.** Top: three example models of some of the best-fitting snapshots from the image library of GRMHD simulations for April 11 corresponding to different spin parameters and accretion flows. Bottom: the same theoretical models, processed through a VLBI simulation pipeline with the same schedule, telescope characteristics, and weather parameters as in the April 11 run and imaged in the same way as Figure 3. Note that although the fit to the observations is equally good in the three cases, they refer to radically different physical scenarios; this highlights that a single good fit does not imply that a model is preferred over others (see Paper V).

spin energy through mechanisms akin to the Blandford–Znajek process.

### 7. Model Comparison and Parameter Estimation

In Paper VI, the black hole mass is derived from fitting to the visibility data of geometric and GRMHD models, as well as from measurements of the ring diameter in the image domain. Our measurements remain consistent across methodologies, algorithms, data representations, and observed data sets.

Motivated by the asymmetric emission ring structures seen in the reconstructed images (Section 5) and the similar emission structures seen in the images from GRMHD simulations (Section 6), we developed a family of geometric crescent models (see, e.g., Kamruddin & Dexter 2013) to compare directly to the visibility data. We used two distinct Bayesian-inference algorithms and demonstrate that such crescent models are statistically preferred over other comparably complex geometric models that we have explored. We find that the crescent models provide fits to the data that are statistically comparable to those of the reconstructed images presented in Section 5, allowing us to determine the basic parameters of the crescents. The best-fit models for the asymmetric emission ring have diameters of  $43 \pm 0.9 \mu\text{as}$  and fractional widths relative to the diameter of

The diameters of the geometric crescent models measure the characteristic sizes of the emitting regions that surround the shadows and not the sizes of the shadows themselves (see, e.g., Psaltis et al. 2015; Johannsen et al. 2016; Kuramochi et al. 2018, for potential biases).

We model the crescent angular diameter  $d$  in terms of the gravitational radius and distance,  $\theta_g \equiv GM/c^2D$ , as  $d = \alpha\theta_g$ , where  $\alpha$  is a function of spin, inclination, and  $R_{\text{high}}$  ( $\alpha \simeq 9.6\text{--}10.4$  corresponds to emission from the lensed photon ring only). We calibrate  $\alpha$  by fitting the geometric crescent models to a large number of visibility data generated from the Image Library. We can also fit the model visibilities generated from the Image Library to the M87\* data, which allows us to measure  $\theta_g$  directly. However, such a procedure is complicated by the stochastic nature of the emission in the accretion flow (see, e.g., Kim et al. 2016). To account for this turbulent structure, we developed a formalism and multiple algorithms that estimate the statistics of the stochastic components using ensembles of images from individual GRMHD simulations. We find that the visibility data are not inconsistent with being a realization of many of the GRMHD simulations. We conclude that the recovered model parameters are consistent across algorithms.

Finally, we extract ring diameter, width, and shape directly

# Basic Statements

- First, the observed image is consistent with the hypothesis that it is produced by a magnetized accretion flow orbiting within a few  $r_g$  of the event horizon of a Kerr black hole. The asymmetric ring is produced by a combination of strong gravitational lensing and relativistic beaming, while the central flux depression is the observational signature of the black hole shadow.
- Second, the north–south asymmetry in the emission ring is controlled by the black hole spin and can be used to deduce its orientation. The north–south asymmetry is consistent with models in which the black hole spin is pointing away from Earth and inconsistent with models in which the spin points toward Earth.
- Third, adopting an inclination of  $17^\circ$  between the approaching jet and the line of sight (Walker et al. 2018), the west orientation of the jet, and a corotating disk model, matter in the bottom part of the image is moving toward the observer (**clockwise rotation as seen from Earth**). Finally, models with  $a_* = 0$  are disfavored by the very conservative observational requirement that the jet power be  $P_{\text{jet}} > 10^{42} \text{ erg s}^{-1}$ .

# Model Comparison and Parameter Estimation

THE ASTROPHYSICAL JOURNAL LETTERS, 875:L1 (17pp), 2019 April 10

The EHT Collaboration et al.

**Table 1**  
Parameters of M87\*

Parameter	Estimate
Ring diameter <sup>a</sup> $d$	$42 \pm 3 \mu\text{as}$
Ring width <sup>a</sup>	$< 20 \mu\text{as}$
Crescent contrast <sup>b</sup>	$> 10:1$
Axial ratio <sup>a</sup>	$< 4:3$
Orientation PA	$150^\circ\text{--}200^\circ$ east of north
$\theta_g = GM/De^2$ <sup>c</sup>	$3.8 \pm 0.4 \mu\text{as}$
$\alpha = d/\theta_g$ <sup>d</sup>	$11^{+0.5}_{-0.3}$
$M$ <sup>e</sup>	$(6.5 \pm 0.7) \times 10^9 M_\odot$
Parameter	Prior Estimate
$D$ <sup>e</sup>	$(16.8 \pm 0.8) \text{ Mpc}$
$M(\text{stars})$ <sup>e</sup>	$6.2^{+1.1}_{-0.6} \times 10^9 M_\odot$
$M(\text{gas})$ <sup>e</sup>	$3.5^{+0.9}_{-0.3} \times 10^9 M_\odot$

**Notes.**

<sup>a</sup> Derived from the image domain.

<sup>b</sup> Derived from crescent model fitting.

<sup>c</sup> The mass and systematic errors are averages of the three methods (geometric models, GRMHD models, and image domain ring extraction).

<sup>d</sup> The exact value depends on the method used to extract  $d$ , which is reflected in the range given.

<sup>e</sup> Rederived from likelihood distributions (Paper VI).

procedure, we infer values of  $\theta_g$  and  $\alpha$  for regularized maximum likelihood and CLEAN reconstructed images.

Combining results from all methods, we measure emission region diameters of  $42 \pm 3 \mu\text{as}$ , angular sizes of the gravitational radius  $\theta_g = 3.8 \pm 0.4 \mu\text{as}$ , and scaling factors in the range  $\alpha = 10.7\text{--}11.5$ , with associated errors of  $\sim 10\%$ . For the distance of  $16.8 \pm 0.8 \text{ Mpc}$  adopted here, the black hole mass is  $M = (6.5 \pm 0.7) \times 10^9 M_\odot$ ; the systematic error refers to the 68% confidence level and is much larger than the statistical error of  $0.2 \times 10^9 M_\odot$ . Moreover, by tracing the peak of the emission in the ring we can determine the shape of the image and obtain a ratio between major and minor axis of the ring that is  $\lesssim 4:3$ ; this corresponds to a  $\lesssim 10\%$  deviation from circularity in terms of root-mean-square distance from an average radius.

Table 1 summarizes the measured parameters of the image features and the inferred black hole properties based on data from all bands and all days combined. The inferred black hole mass strongly favors the measurement based on stellar dynamics (Gebhardt et al. 2011). The size, asymmetry, brightness contrast, and circularity of the reconstructed images and geometric models, as well as the success of the GRMHD simulations in describing the interferometric data, are consistent with the EHT images of M87\* being associated with strongly lensed emission from the vicinity of a Kerr black hole.

## 8. Discussion

A number of elements reinforce the robustness of our image

our measurement of the black hole mass in M87\* is not inconsistent with all of the prior mass measurements, this allows us to conclude that the null hypothesis of the Kerr metric (Psaltis et al. 2015; Johannsen et al. 2016), namely, the assumption that the black hole is described by the Kerr metric, has not been violated. Fourth, the observed emission ring reconstructed in our images is close to circular with an axial ratio  $\lesssim 4:3$ ; similarly, the time average images from our GRMHD simulations also show a circular shape. After associating to the shape of the shadow a deviation from the circularity—measured in terms of root-mean-square distance from an average radius in the image—that is  $\lesssim 10\%$ , we can set an initial limit of order four on relative deviations of the quadrupole moment from the Kerr value (Johannsen & Psaltis 2010). Stated differently, if  $Q$  is the quadrupole moment of a Kerr black hole and  $\Delta Q$  the deviation as deduced from circularity, our measurement—and the fact that the inclination angle is assumed to be small—implies that  $\Delta Q/Q \lesssim 4$  ( $\Delta Q/Q = \epsilon$  in Johannsen & Psaltis 2010).

Finally, when comparing the visibility amplitudes of M87\* with 2009 and 2012 data (Doeleman et al. 2012; Akiyama et al. 2015), the overall radio core size at a wavelength of 1.3 mm has not changed appreciably, despite variability in total flux density. This stability is consistent with the expectation that the size of the shadow is a feature tied to the mass of the black hole and not to properties of a variable plasma flow.

It is also straightforward to reject some alternative astrophysical interpretations. For instance, the image is unlikely to be produced by a jet-feature as multi-epoch VLBI observations of the plasma jet in M87 (Walker et al. 2018) on scales outside the horizon do not show circular rings. The same is typically true for AGN jets in large VLBI surveys (Lister et al. 2018). Similarly, were the apparent ring a random alignment of emission blobs, they should also have moved away at relativistic speeds, i.e., at  $\sim 5 \mu\text{as day}^{-1}$  (Kim et al. 2018b), leading to measurable structural changes and sizes. GRMHD models of hollow jet cones could show under extreme conditions stable ring features (Pu et al. 2017), but this effect is included to a certain extent in our Simulation Library for models with  $R_{\text{high}} > 10$ . Finally, an Einstein ring formed by gravitational lensing of a bright region in the counter-jet would require a fine-tuned alignment and a size larger than that measured in 2012 and 2009.

At the same time, it is more difficult to rule out alternatives to black holes in GR, because a shadow can be produced by any compact object with a spacetime characterized by unstable circular photon orbits (Mizuno et al. 2018). Indeed, while the Kerr metric remains a solution in some alternative theories of gravity (Barausse & Sotiriou 2008; Psaltis et al. 2008), non-Kerr black hole solutions do exist in a variety of such modified theories (Berti et al. 2015). Furthermore, exotic alternatives to black holes, such as naked singularities (Shaikh et al. 2019), boson stars (Kaup 1968; Liebling & Palenzuela 2012), and gravastars (Mazur & Mottola 2004; Chirenti & Rezzolla 2007), are admissible solutions within GR and provide concrete, albeit

- The best-fit models for the asymmetric emission ring have diameters of  $43 \pm 0.9 \mu\text{as}$  and fractional widths relative to the diameter of  $< 0.5$ .
- We model the crescent angular diameter  $d$  in terms of the gravitational radius and distance,  $\theta_g = GM / (c^2 D)$ , as  $d = \alpha \theta_g$  where  $\alpha$  is a function of spin, inclination, and  $R_{high}$  ( $9.6 < \alpha < 10.4$ ] corresponds to emission from the lensed photon ring only). We calibrate  $\alpha$  by fitting the geometric crescent models to a large number of visibility data generated from the Image Library. We can also fit the model visibilities generated from the Image Library to the M87\* data, which allows us to measure  $\theta_g$  directly. Combining results from all methods, we measure emission region diameters of  $42 \pm 3 \mu\text{as}$ , angular sizes of the gravitational radius  $\theta_g = 3.8 \pm 0.4 \mu\text{as}$ , and scaling factors in the range  $\alpha = 10.7 - 11.5$ , with associated errors of  $\sim 10\%$ . For the distance of  $16.8 \pm 0.8 \text{ Mpc}$  adopted here, the black hole mass is  $M = (6.5 \pm 0.7) \times 10^9 M_{\text{sun}}$ ; the systematic error refers to the 68% confidence level and is much larger than the statistical error of  $0.2 \times 10^9 M_{\text{sun}}$ .

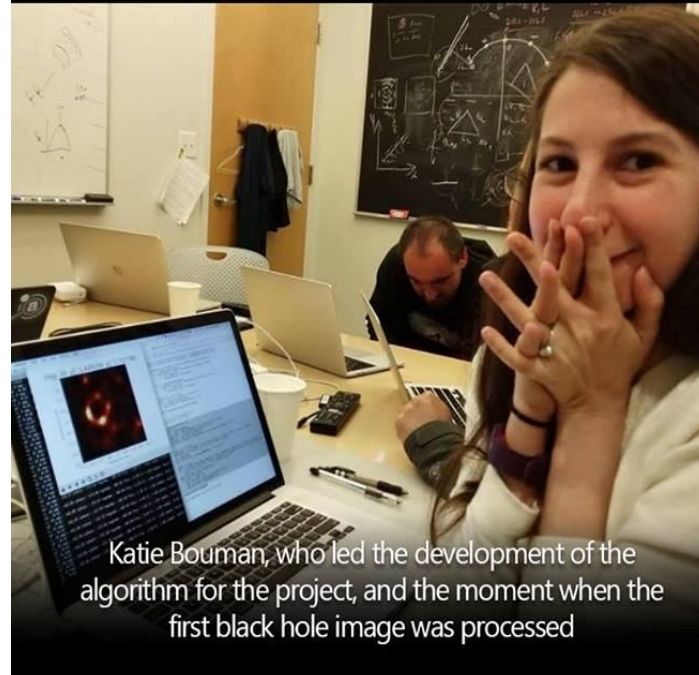
- It is difficult to rule out alternatives to black holes in GR, because a shadow can be produced by any compact object with a spacetime characterized by unstable circular photon orbits (Mizuno et al. 2018). Indeed, while the Kerr metric remains a solution in some alternative theories of gravity (Barausse & Sotiriou 2008; Psaltis et al. 2008), non-Kerr black hole solutions do exist in a variety of such modified theories (Berti et al. 2015). Furthermore, exotic alternatives to black holes, such as naked singularities (Shaikh et al. 2019), boson stars (Kaup 1968; Liebling & Palenzuela 2012), and gravastars (Mazur & Mottola 2004; Chirenti & Rezzolla 2007), are admissible solutions within GR and provide concrete, albeit contrived, models. Some of such exotic compact objects can already be shown to be incompatible with our observations given our maximum mass prior

# POWEHI

- It's been christened Powehi -- a Hawaiian phrase referring to an "embellished dark source of unending creation." (украшенный темный источник бесконечного творения)
- The responsibility of finding it a name fell to Larry Kimura, a Hawaiian language professor at the University of Hawaii at Hilo, who was approached by astronomers involved with the project. Two of the eight telescopes used to capture the photograph are located in Hawaii.
- It puts together two terms from the chant: Po, meaning profound dark source of unending creation, and wehi (or wehiwehi) which is one of the several ways that po is described in the chant.
- To have the privilege of giving a Hawaiian name to the very first scientific confirmation of a black hole is very meaningful to me and my Hawaiian lineage that comes from po," he added. "I hope we are able to continue naming future black holes from Hawaii astronomy according to the Kumulipo.
- <https://edition.cnn.com/2019/04/12/world/black-hole-name-powehi-scli-intl/index.html>



5 petabytes (5,242,880 Gigabytes) of data necessary to image a black hole



Katie Bouman, who led the development of the algorithm for the project, and the moment when the first black hole image was processed

# A.F. Zakharov & F. De Paolis, A.A. Nucita, G.Ingrosso, **Astron. & Astrophys.**, **442, 795 (2005)**

As it was explained by Zakharov et al. (2005a,b) this leads to the formation of shadows described by the critical value of  $L_{cr}$  or, in other words, in the spherically symmetric case, shadows are circles with radii  $L_{cr}$ . Therefore, measuring the shadow size, one could evaluate the black hole charge in black hole mass units  $M$ .

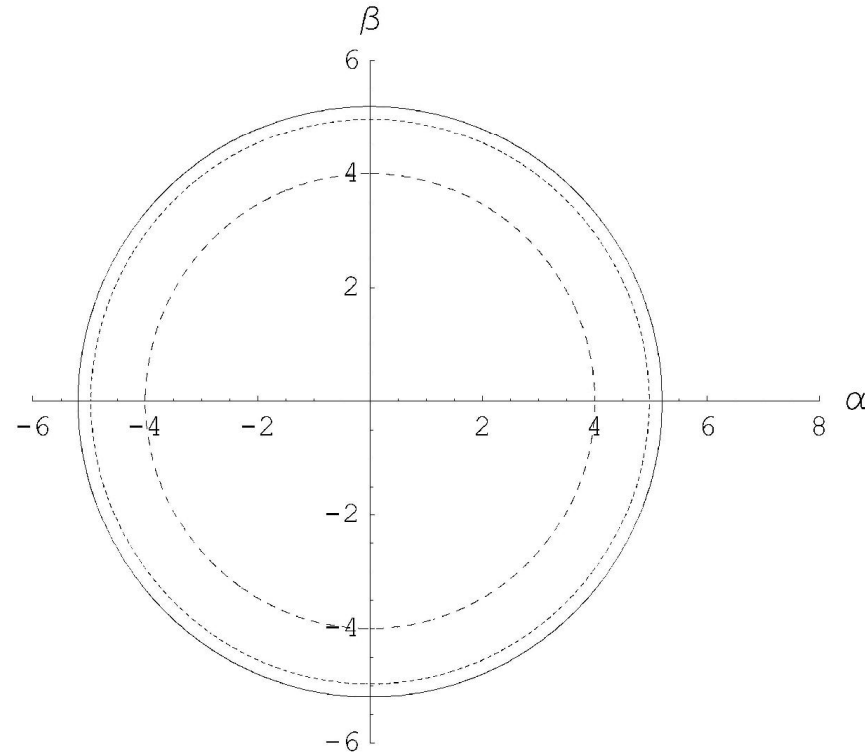


**Fig. 1.** Shadow (mirage) sizes are shown for selected charges of black holes  $Q = 0$  (solid line),  $Q = 0.5$  (short dashed line) and  $Q = 1$  (long dashed line).

**Constraints on black-hole charges with the 2017 EHT observations of M87\***

Prashant Kocherlakota<sup>1</sup>, Luciano Rezzolla,<sup>1-3</sup> Heino Falcke,<sup>4</sup> Christian M. Fromm,<sup>5,6,1</sup> Michael Kramer,<sup>7</sup> Yosuke Mizuno,<sup>8,9</sup> Antonios Nathanail,<sup>9,10</sup> Héctor Olivares,<sup>11</sup> Ziri Younsi,<sup>11,3</sup> Kazunori Akiyama,<sup>12,13,5</sup> Antxon Alberdi,<sup>14</sup> Walter Alef,<sup>7</sup> Juan Carlos Algaba,<sup>15</sup> Richard Anantua,<sup>5,6,16</sup> Keiichi Asada,<sup>17</sup> Rebecca Azulay,<sup>18,19,7</sup> Anne-Kathrin Baczo,<sup>7</sup> David Ball,<sup>20</sup> Mislav Baloković,<sup>5,6</sup> John Barrett,<sup>12</sup> Bradford A. Benson,<sup>21,22</sup> Dan Bintley,<sup>23</sup> Lindy Blackburn,<sup>5,6</sup> Raymond Blundell,<sup>6</sup> Wilfred Boland,<sup>24</sup> Katherine L. Bouman,<sup>5,6,25</sup> Geoffrey C. Bower,<sup>26</sup> Hope Boyce,<sup>27,28</sup> Michael Bremer,<sup>29</sup> Christiaan D. Brinkerink,<sup>4</sup> Roger Brissenden,<sup>5,6</sup> Silke Britzen,<sup>7</sup> Avery E. Broderick,<sup>30-32</sup> Dominique Brogiere,<sup>29</sup> Thomas Bronzwaer,<sup>4</sup> Do-Young Byun,<sup>33,34</sup> John E. Carlstrom,<sup>35,22,36,37</sup> Andrew Chael,<sup>38,39</sup> Chi-kwan Chan,<sup>20,40</sup> Shami Chatterjee,<sup>41</sup> Koushik Chatterjee,<sup>42</sup> Ming-Tang Chen,<sup>26</sup> Yongjun Chen (陈永军),<sup>43,44</sup> Paul M. Chesler,<sup>5</sup> Ilje Cho,<sup>33,34</sup> Pierre Christian,<sup>45</sup> John E. Conway,<sup>46</sup> James M. Cordes,<sup>41</sup> Thomas M. Crawford,<sup>47,23,5</sup> Geoffrey B. Crew,<sup>12</sup> Alejandro Cruz-Orsorio,<sup>9</sup> Yuzhu Cui,<sup>47,48</sup> Jordy Davelaar,<sup>49,16,4</sup> Mariafelicia De Laurentis,<sup>50,9,51</sup> Roger Deane,<sup>52-54</sup> Jessica Dempsey,<sup>23</sup> Gregory Desvignes,<sup>55</sup> Sheperd S. Doeleman,<sup>5,6</sup> Ralph P. Eatough,<sup>56,7</sup> Joseph Farah,<sup>6,5,57</sup> Vincent L. Fish,<sup>12</sup> Ed Fomalont,<sup>58</sup> Raquel Fraga-Encinas,<sup>4</sup> Per Friberg,<sup>23</sup> H. Alyson Ford,<sup>59</sup> Antonio Fuentes,<sup>14</sup> Peter Galison,<sup>60,61</sup> Charles F. Gammie,<sup>62,63</sup> Roberto García,<sup>29</sup> Olivier Gentaz,<sup>29</sup> Boris Georgiev,<sup>31,32</sup> Ciriaco Goddi,<sup>4,64</sup> Roman Gold,<sup>65,30</sup> José L. Gómez,<sup>14</sup> Arturo I. Gómez-Ruiz,<sup>66,67</sup> Minfeng Gu (顾敏峰),<sup>43,68</sup> Mark Gurwell,<sup>6</sup> Kazuhiro Hada,<sup>47,48</sup> Daryl Haggard,<sup>27,28</sup> Michael H. Hecht,<sup>12</sup> Ronald Hesper,<sup>69</sup> Luis C. Ho (何子山),<sup>70,71</sup> Paul Ho,<sup>17</sup> Mareki Honma,<sup>47,48,72</sup> Chih-Wei L. Huang,<sup>17</sup> Lei Huang (黄磊),<sup>43,68</sup> David H. Hughes,<sup>66</sup> Shiro Ikeda,<sup>13,73-75</sup> Makoto Inoue,<sup>17</sup> Sara Issaoun,<sup>4</sup> David J. James,<sup>5,6</sup> Buell T. Jannuzi,<sup>20</sup> Michael Janssen,<sup>7</sup> Britton Jeter,<sup>31,32</sup> Wu Jiang (江楷),<sup>43</sup> Alejandra Jimenez-Rosales,<sup>4</sup> Michael D. Johnson,<sup>5,6</sup> Svetlana Jorstad,<sup>76,7</sup> Taehyun Jung,<sup>33,34</sup> Mansour Karami,<sup>30,31</sup> Ramesh Karuppusamy,<sup>7</sup> Tomohisa Kawashima,<sup>78</sup> Garrett K. Keating,<sup>6</sup> Mark Kettenis,<sup>79</sup> Dong-Jin Kim,<sup>7</sup> Jae-Young Kim,<sup>33,7</sup> Jongsoo Kim,<sup>33</sup> Junhan Kim,<sup>20,25</sup> Motoki Kino,<sup>13,80</sup> Jun Yi Koay,<sup>17</sup> Yutaro Kofuji,<sup>47,72</sup> Patrick M. Koch,<sup>17</sup> Shoko Koyama,<sup>17</sup> Carsten Kramer,<sup>29</sup> Thomas P. Krichbaum,<sup>7</sup> Cheng-Yu Kuo,<sup>81,17</sup> Tod R. Lauer,<sup>82</sup> Sang-Sung Lee,<sup>33</sup> Aviad Levis,<sup>25</sup> Yan-Rong Li (李彦荣),<sup>83</sup> Zhiyuan Li (李志远),<sup>84,85</sup> Michael Lindqvist,<sup>46</sup> Rocco Lico,<sup>14,7</sup> Greg Lindahl,<sup>6</sup> Jun Liu (刘俊),<sup>7</sup> Kuo Liu,<sup>7</sup> Elisabetta Liuzzo,<sup>86</sup> Wen-Ping Lo,<sup>17,87</sup> Andrei P. Lobanov,<sup>7</sup> Laurent Loinard,<sup>88,89</sup> Colin Lonsdale,<sup>12</sup> Ru-Sen Lu (路如森),<sup>43,44,7</sup> Nicholas R. MacDonald,<sup>7</sup> Jirong Mao (毛基荣),<sup>90-92</sup> Nicola Marchili,<sup>86,7</sup> Sera Markoff,<sup>42,93</sup> Daniel P. Marrone,<sup>20</sup> Alan P. Marscher,<sup>76</sup> Iván Martí-Vidal,<sup>18,19</sup> Satoki Matsushita,<sup>17</sup> Lynn D. Matthews,<sup>12</sup> Lia Medeiros,<sup>94,20</sup> Karl M. Menten,<sup>7</sup> Izumi Mizuno,<sup>23</sup> James M. Moran,<sup>5,6</sup> Kotaro Moriyama,<sup>12,47</sup> Monika Moscibrodzka,<sup>4</sup> Cornelia Müller,<sup>7,4</sup> Gibwa Musoke,<sup>42,4</sup> Alejandro Mus Mejías,<sup>18,19</sup> Hiroshi Nagai,<sup>13,48</sup> Neil M. Nagar,<sup>95</sup> Masanori Nakamura,<sup>96,17</sup> Ramesh Narayan,<sup>5,6</sup> Gopal Narayanan,<sup>7</sup> Iniyar Natarajan,<sup>97</sup> Joseph Neilsen,<sup>39</sup> Roberto Neri,<sup>29</sup> Chunhong Ni,<sup>31,32</sup> Aristeidis Noutsos,<sup>7</sup> Michael A. Nowak,<sup>100</sup> Hiroki Okino,<sup>47,72</sup> Gisela N. Ortiz-León,<sup>7</sup> Tomoaki Oyama,<sup>47</sup> Feryal Özel,<sup>20</sup> Daniel C. M. Palumbo,<sup>5,6</sup> Jongho Park,<sup>17</sup> Nimesh Patel,<sup>6</sup> Ue-Li Pen,<sup>30,101-103</sup> Dominic W. Pesce,<sup>5,6</sup> Vincent Piétu,<sup>29</sup> Richard Plambeck,<sup>104</sup> Aleksandar PopStefanija,<sup>97</sup> Oliver Porth,<sup>42,9</sup> Felix M. Pötzl,<sup>7</sup> Ben Prather,<sup>62</sup> Jorge A. Preciado-López,<sup>30</sup> Dimitrios Psaltis,<sup>20</sup> Hung-Yi Pu,<sup>105,17,30</sup> Venkatesh Ramakrishnan,<sup>98</sup> Ramprasad Rao,<sup>26</sup> Mark G. Rawlings,<sup>23</sup> Alexander W. Raymond,<sup>5,6</sup> Angelo Ricarte,<sup>5,6</sup> Bart Ripperda,<sup>106,16</sup> Freek Roelofs,<sup>4</sup> Alan Rogers,<sup>12</sup> Eduardo Ros,<sup>7</sup> Mel Rose,<sup>20</sup> Arash Roshanineshat,<sup>20</sup> Helge Rottmann,<sup>7</sup> Alan L. Roy,<sup>7</sup> Chet Ruzszyk,<sup>12</sup> Kazi L. J. Rygl,<sup>86</sup> Salvador Sánchez,<sup>107</sup> David Sánchez-Argüelles,<sup>66,67</sup> Mahito Sasada,<sup>47,108</sup> Tuomas Savolainen,<sup>109,110,7</sup> F. Peter Schloerb,<sup>97</sup> Karl-Friedrich Schuster,<sup>29</sup> Lijing Shao,<sup>7,71</sup> Zhiqiang Shen (沈志强),<sup>43,44</sup> Des Small,<sup>79</sup> Bong Won Sohn,<sup>33,34,111</sup> Jason SooHoo,<sup>12</sup> He Sun (孙赫),<sup>25</sup> Fumie Tazaki,<sup>47</sup> Alexandra J. Tetarenko,<sup>112</sup> Paul Tiede,<sup>31,32</sup> Remo P. J. Tilanus,<sup>4,64,113,20</sup> Michael Titus,<sup>12</sup> Kenji Toma,<sup>114,115</sup> Pablo Torme,<sup>7,107</sup> Tyler Trent,<sup>20</sup> Efthalia Traianou,<sup>7</sup> Sascha Trippe,<sup>116</sup> Ilse van Bemmell,<sup>79</sup> Huib Jan van Langevelde,<sup>79,117</sup> Daniel R. van Rossum,<sup>4</sup> Jan Wagner,<sup>7</sup> Derek Ward-Thompson,<sup>118</sup> John Wardle,<sup>119</sup> Jonathan Weintraub,<sup>5,6</sup> Norbert Wex,<sup>7</sup> Robert Wharton,<sup>7</sup> Maciek Wielgus,<sup>5,6</sup> George N. Wong,<sup>62</sup> Qingwen Wu (吴庆文),<sup>120</sup> Doosoo Yoon,<sup>42</sup> André Young,<sup>4</sup> Ken Young,<sup>6</sup> Feng Yuan (袁峰),<sup>43,68,121</sup> Ye-Fei Yuan (袁业飞),<sup>122</sup> J. Anton Zensus,<sup>7</sup> Guang-Yao Zhao,<sup>14</sup> and Shan-Shan Zhao<sup>43</sup>

(EHT Collaboration)

<sup>1</sup>*Institut für Theoretische Physik, Goethe-Universität, Max-von-Laue-Strasse 1, 60438 Frankfurt, Germany*<sup>2</sup>*Frankfurt Institute for Advanced Studies, Ruth-Moufang-Strasse 1, 60438 Frankfurt, Germany*<sup>3</sup>*School of Mathematics, Trinity College, Dublin 2, Ireland*<sup>4</sup>*Department of Astrophysics, Institute for Mathematics, Astrophysics and Particle Physics (IMAPP), Radboud University, P.O. Box 9010, 6500 GL Nijmegen, Netherlands*<sup>5</sup>*Black Hole Initiative at Harvard University, 20 Garden Street, Cambridge, Massachusetts 02138, USA*

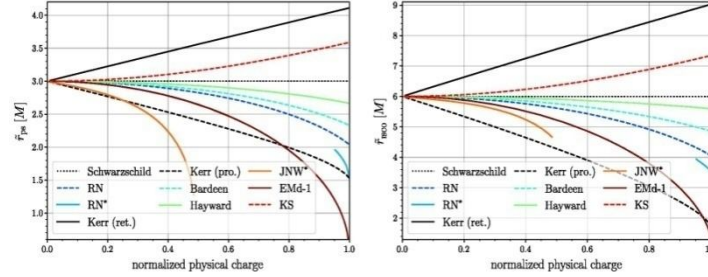


FIG. 1. Left: variation in the photon sphere radii for the single-charge nonrotating solutions as a function of the normalized physical charge. Right: The same as in the left panel but for the ISCO radii. We include also, for comparison, the variation in the Kerr equatorial prograde and retrograde photon sphere and ISCO radii in the left and right panels respectively.

depend exclusively on the  $g_{tt}$  component of the metric when expressed using an areal radial coordinate  $\tilde{r}$  (see, e.g., [28,36]). To gauge the effect of spin, we also show the variation in the locations of the equatorial prograde and retrograde circular photon orbits and the ISCOs in the Kerr black-hole spacetime, expressed in terms of the Cartesian Kerr-Schild radial coordinate  $r_{\text{CKS}}$ , which, in the equatorial plane, is related to the Boyer-Lindquist radial coordinate used elsewhere in this work  $r$  simply via [90]

$$r_{\text{CKS}} = \sqrt{r^2 + a^2}. \quad (15)$$

It is apparent from Fig. 1 that the maximum deviation in the photon-sphere size from the Schwarzschild solution occurs for the EMD-1 black hole and is  $\approx 75\%$ , while the size of the prograde equatorial circular photon orbit for Kerr deviates by at most  $\approx 50\%$ . Similarly, the maximum variation in the ISCO size also occurs for the EMD-1 solution and is  $\approx 73\%$ , while the prograde equatorial ISCO for Kerr can differ by  $\approx 66\%$ .

### V. CHARGE CONSTRAINTS FROM THE EHT M87\* OBSERVATIONS

We first consider compact objects with a single “charge,” and report in the left panel of Fig. 2 the variation in the shadow radius for various spherically symmetric black hole solutions, as well as for the RN and JNW naked singularities.<sup>3</sup> More specifically, we consider the black-hole

<sup>3</sup>While the electromagnetic and scalar charge parameters for the RN and JNW spacetimes are allowed to take values  $\hat{q} > 1$  and  $0 < \hat{b} := 1 - \hat{v} < 1$  respectively, they do not cast shadows for  $\hat{q} > \sqrt{9/8}$  and  $0.5 \leq \hat{b} < 1$  (see, e.g., Sec. IV D of [36] and references therein).

solutions given by Reissner-Nordström (RN) [62], Bardeen [63,75], Hayward [64,91], Kazakov-Solodukhin (KS) [66], and also the asymptotically-flat Einstein-Maxwell-dilaton (EMd-1) with  $\phi_\infty = 0$  and  $\alpha_1 = 1$  [67,68,88] solution (see Sec. IV of [36] for further details on these solutions). For each of these solutions we vary the corresponding charge (in units of  $M$ ) in the allowed range, i.e., RN:  $0 < \hat{q} \leq 1$ ; Bardeen:  $0 < \hat{q}_m \leq \sqrt{16/27}$ ; Hayward:  $0 < \hat{l} \leq \sqrt{16/27}$ ; Frolov:  $0 < \hat{l} \leq \sqrt{16/27}$ ,  $0 < \hat{q} \leq 1$ ; KS:  $0 < \hat{l}$ ; EMD-1:  $0 < \hat{q} < \sqrt{2}$ , but report the normalized value in the figure so that all curves are in a range between 0 and 1. The figure shows the variation in the shadow size of KS black holes over the parameter range  $0 < \hat{l} < \sqrt{2}$ . Note that the shadow radii tend to become smaller with increasing physical charge, but also that this is not universal behavior, since the KS black holes have increasing shadow radii (the singularity is smeared out on a surface for this solution, which increases in size with increasing  $\hat{l}$ ).

Overall, it is apparent that the regular Bardeen, Hayward, and Frolov black-hole solutions are compatible with the present constraints. At the same time, the Reissner-Nordström and Einstein-Maxwell-dilaton 1 black-hole solutions, for certain values of the physical charge, produce shadow radii that lie outside the  $1-\sigma$  region allowed by the 2017 EHT observations, and we find that these solutions are now constrained to take values in,  $0 < \hat{q} \lesssim 0.90$  and  $0 < \hat{q} \lesssim 0.95$  respectively. Furthermore, the Reissner-Nordström naked singularity is entirely eliminated as a viable model for M87\* and the Janis-Newman-Winicour naked singularity parameter space is restricted further by this measurement to  $0 < \hat{b} \lesssim 0.47$ . Finally, we also find that the KS black hole is also restricted to have charges in the range  $\hat{l} < 1.53$ . In addition, note that the nonrotating Einstein-Maxwell-dilaton 2 (EMd-2) solution [70]—which depends on two

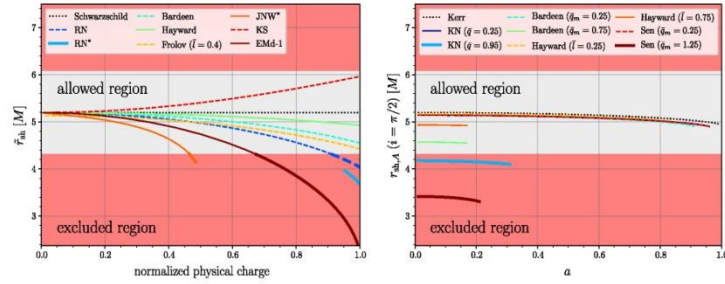


FIG. 2. Left: shadow radii  $r_{\text{sh}}$  for various spherically symmetric black-hole solutions, as well as for the JNW and RN naked singularities (marked with an asterisk), as a function of the physical charge normalized to its maximum value. The gray/red shaded regions refer to the areas that are  $1-\sigma$  consistent/inconsistent with the 2017 EHT observations and highlight that the latter set constrains on the physical charges (see also Fig. 3 for the Emd-2 black hole). Right: shadow areal radii  $r_{\text{sh},A}$  as a function of the dimensionless spin  $a$  for four families of black-hole solutions when viewed on the equatorial plane ( $i = \pi/2$ ). Also in this case, the observations restrict the ranges of the physical charges of the Kerr-Newman and the Sen black holes (see also Fig. 3).

independent charges—can also produce shadow radii that are incompatible with the EHT observations; we will discuss this further below. The two Emd black-hole solutions (1 and 2) correspond to fundamentally different field contents, as discussed in [70].

We report in the right panel of Fig. 2 the shadow areal radius  $r_{\text{sh},A}$  for a number of stationary black holes, such as Kerr [72], Kerr-Newman (KN) [73], Sen [74], and the rotating versions of the Bardeen and Hayward black holes [75]. The data refers to an observer inclination angle of  $i = \pi/2$ , and we find that the variation in the shadow size with spin at higher inclinations (of up to  $i = \pi/100$ ) is at most about 7.1% (for  $i = \pi/2$ , this is 5%); of course, at zero-spin the shadow size does not change with inclination. The shadow areal radii are shown as a function of the dimensionless spin of the black hole  $a := J/M^2$ , where  $J$  is its angular momentum, and for representative values of the additional parameters that characterize the solutions. Note that—similar to the angular momentum for a Kerr black hole—the role of an electric charge or the presence of a de Sitter core (as in the case of the Hayward black holes) is to reduce the apparent size of the shadow. Furthermore, on increasing the spin parameter, we recover the typical trend that the shadow becomes increasingly noncircular, as encoded, e.g., in the distortion parameter  $\delta_{\text{sh}}$  defined in [57,83] (see Appendix). Also in this case, while the regular rotating Bardeen and Hayward solutions are compatible with the present constraints set by the 2017 EHT observations, the Kerr-Newman and Sen families of black holes can produce shadow areal radii that lie outside of the  $1-\sigma$  region allowed by the observations.

To further explore the constraints on the excluded regions for the Einstein-Maxwell-dilaton 2 and the Sen black holes, we report in Fig. 3 the relevant ranges for these two solutions. The Einstein-Maxwell-dilaton 2 black holes are nonrotating but have two physical charges expressed by the coefficients  $0 < \bar{q}_e < \sqrt{2}$  and  $0 < \bar{q}_m < \sqrt{2}$ , while the Sen black holes spin ( $a$ ) and have an additional electromagnetic charge  $\bar{q}_m$ . Also in this case, the gray/red shaded regions refer to the areas that are consistent/inconsistent with the 2017 EHT observations. The figure shows rather easily that for these two black-hole families there are large

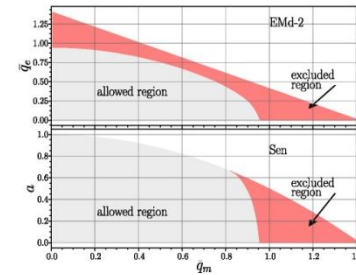
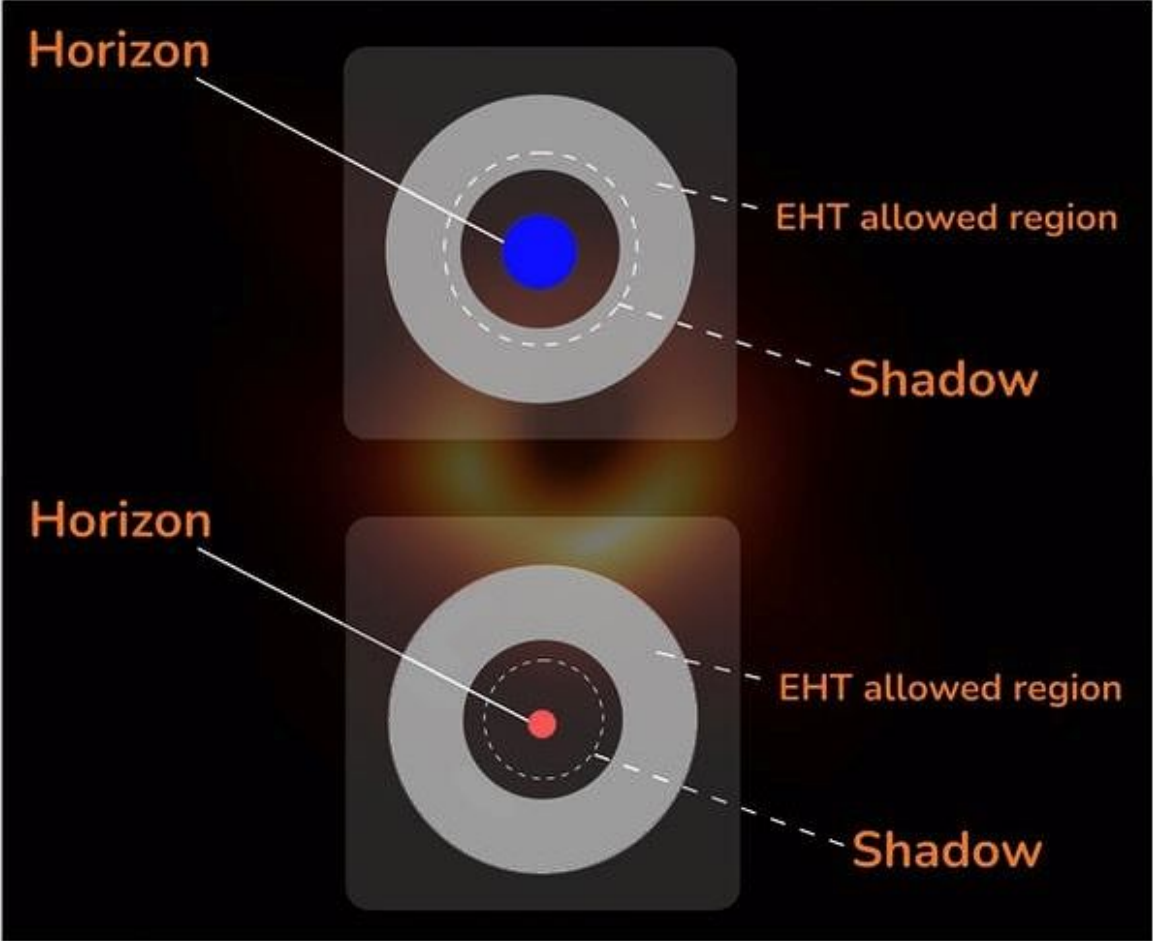


FIG. 3. Constraints set by the 2017 EHT observations on the nonrotating Einstein-Maxwell-dilaton 2 and on the rotating Sen black holes. Also in this case, the gray/red shaded regions refer to the areas that are  $1-\sigma$  consistent/inconsistent with the 2017 EHT observations).





## First M87 Event Horizon Telescope Results. VII. Polarization of the Ring

The Event Horizon Telescope Collaboration

(See the end matter for the full list of authors.)

Received 2020 November 23; revised 2021 February 15; accepted 2021 February 16; published 2021 March 24

### Abstract

In 2017 April, the Event Horizon Telescope (EHT) observed the near-horizon region around the supermassive black hole at the core of the M87 galaxy. These 1.3 mm wavelength observations revealed a compact asymmetric ring-like source morphology. This structure originates from synchrotron emission produced by relativistic plasma located in the immediate vicinity of the black hole. Here we present the corresponding linear-polarimetric EHT images of the center of M87. We find that only a part of the ring is significantly polarized. The resolved fractional linear polarization has a maximum located in the southwest part of the ring, where it rises to the level of  $\sim 15\%$ . The polarization position angles are arranged in a nearly azimuthal pattern. We perform quantitative measurements of relevant polarimetric properties of the compact emission and find evidence for the temporal evolution of the polarized source structure over one week of EHT observations. The details of the polarimetric data reduction and calibration methodology are provided. We carry out the data analysis using multiple independent imaging and modeling techniques, each of which is validated against a suite of synthetic data sets. The gross polarimetric structure and its apparent evolution with time are insensitive to the method used to reconstruct the image. These polarimetric images carry information about the structure of the magnetic fields responsible for the synchrotron emission. Their physical interpretation is discussed in an accompanying publication.

*Unified Astronomy Thesaurus concepts:* Polarimetry (1278); Radio interferometry (1346); Very long baseline interferometry (1769); Supermassive black holes (1663); Active galactic nuclei (16); Low-luminosity active galactic nuclei (2033); Astronomy data modeling (1859); Galaxy accretion disks (562); Galaxies: individual: M87

### 1. Introduction

The Event Horizon Telescope (EHT) Collaboration has recently reported the first images of the event-horizon-scale structure around the supermassive black hole in the core of the massive elliptical galaxy M87, one of its two main targets.<sup>130</sup> The EHT images of M87's core at 230 GHz (1.3 mm wavelength) revealed a ring-like structure whose diameter of  $42 \mu\text{as}$ , brightness temperature, shape, and asymmetry are interpreted as synchrotron emission from relativistic electrons gyrating around magnetic field lines in close vicinity to the event horizon. We have described the details of the EHT's instrumentation, data calibration pipelines, data analyses and imaging procedures, and the theoretical interpretation of these first images in a series of publications (Event Horizon Telescope Collaboration et al. 2019a, 2019b, 2019c, 2019d, 2019e, 2019f, hereafter Papers I, II, III, IV, V, VI, respectively).

In this Letter, we present the first *polarimetric* analysis of the 2017 EHT observations of M87 and the first images of the linearly polarized radiation surrounding the M87 black hole shadow. These polarimetric images provide essential new information about the

structure of magnetic field lines near the event horizon of M87's central supermassive black hole, and they put tight constraints on the theoretical interpretations of the nature of the ring and of relativistic jet-launching theories. The theoretical implications of these images and the constraints that they place on the magnetic field structure and accretion state of the black hole are discussed in an accompanying work (Event Horizon Telescope Collaboration et al. 2021, hereafter Paper VIII). Readers interested in the details of the data reduction, methodology, and validation can find a detailed index of this Letter in Section 1.2. Readers primarily interested in the results may skip directly to Section 5 and to subsequent discussion and conclusions in Section 6.

#### 1.1. Previous Polarimetric Observations of the M87 Jet

The giant elliptical galaxy Messier 87 (M87, NGC 4486) is the central member of the Virgo cluster of galaxies and hosts a low-luminosity radio source (Virgo A, 3C 274, B1228+126). M87 is nearby and bright, and at its center is one of the best-studied active galactic nuclei (AGNs). M87 was the first galaxy in which an extragalactic jet (first described as a "narrow ray") extending from the nucleus was discovered (Curtis 1918). This kiloparsec-scale jet is visible, with remarkably similar morphology, at all wavelengths from radio to X-ray. The optical radiation from the jet on kpc scales was found to be linearly polarized by Baade (1956), which was confirmed by Hiltner (1959), suggesting that the emission mechanism is synchrotron radiation.

The central engine that powers the jet contains one of the most massive black holes known, measured from the central stellar velocity dispersion (Gebhardt et al. 2011;  $M = (6.6 \pm 0.4) \times 10^9 M_{\odot}$ ) and directly from the size of the observed emitting

<sup>127</sup> NASA Hubble Fellowship Program, Einstein Fellow.

<sup>128</sup> EACOA Fellow.

<sup>129</sup> UKRI Stephen Hawking Fellow.

<sup>130</sup> The other primary target being the black hole in Sgr A\* in the center of the Milky Way.

Original content from this work may be used under the terms of the Creative Commons Attribution 4.0 licence. Any further distribution of this work must maintain attribution to the author(s) and the title of the work, journal citation and DOI.

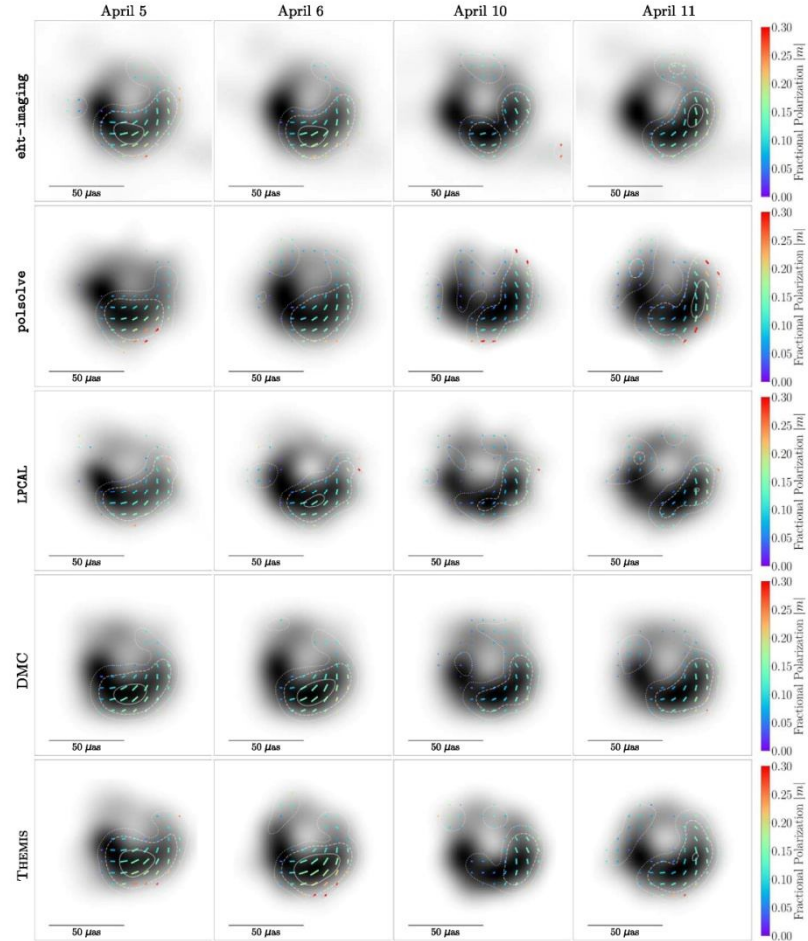


**Figure 6.** Fiducial polarimetric M87 images produced by five independent methods. The results from all imaging and posterior exploration pipelines are shown on the four M87 observation days for the low band data (the low- and high-band results are consistent, see Appendix D). Total intensity is shown in grayscale, polarization ticks indicate the EVPA, the tick length indicates linear polarization intensity magnitude (where a tick length of  $10 \mu\text{as}$  corresponds to  $\sim 30 \mu\text{Jy } \mu\text{as}^{-2}$  of polarized flux density), and color indicates fractional linear polarization. The tick length is scaled according to the polarized brightness without renormalization to the maximum for each image. The contours mark the linear polarized intensity. The solid, dashed, and dotted contour levels correspond to linearly polarized intensity of 20, 10, and  $5 \mu\text{Jy } \mu\text{as}^{-2}$ , respectively. Cuts were made to omit all regions in the images where Stokes  $I < 10\%$  of the peak brightness and  $\mathcal{P} < 20\%$  of the peak polarized brightness. The images are all displayed with a field of view of  $120 \mu\text{as}$ , and all images were brought to the same nominal resolution by convolution with the circular Gaussian kernel that maximized the cross-correlation of the blurred Stokes  $I$  image with the consensus Stokes  $I$  image of Paper IV.

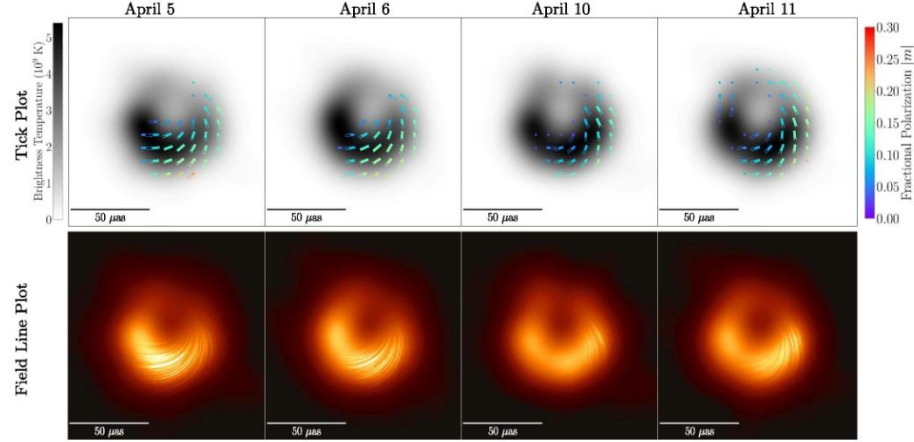


**Figure 7.** Fiducial M87 average images produced by averaging results from our five reconstruction methods (see Figure 6). Method-average images for all four M87 observation days are shown, from left to right. These images show the low-band results; for a comparison between these images and the high-band results, see Figure 28 in Appendix I. We employ here two visualization schemes (top and bottom rows) to display our four method-average images. The images are all displayed with a field of view of  $120 \mu\text{as}$ . Top row: total intensity, polarization fraction, and EVPA are plotted in the same manner as in Figure 6. Bottom row: polarization “field lines” plotted atop an underlying total intensity image. Treating the linear polarization as a vector field, the sweeping lines in the images represent streamlines of this field and thus trace the EVPA patterns in the image. To emphasize the regions with stronger polarization detections, we have scaled the length and opacity of these streamlines as the square of the polarized intensity. This visualization is inspired in part by Line Integral Convolution (Cabral & Leedom 1993) representations of vector fields, and it aims to highlight the newly added polarization information on top of the standard visualization for our previously published Stokes  $Z$  results (Papers I, IV).

angle around the ring). We consider these two days because they have the best  $(u, v)$  coverage and span the full observation window; these results will thus include any effects of intrinsic source evolution in the recovered parameters. From Figure 8, it is evident that the difference in  $\langle p \rangle$  between methods is larger than the widths of the  $\langle p \rangle$  histograms in each method. This means that effects related to the residual instrumental polarization, giving rise to the dispersion seen in the histograms, are smaller than artifacts related to the deconvolution algorithms. In other words, the  $\langle p \rangle$  images are limited by the image fidelity due to the sparse  $(u, v)$  coverage rather than by the D-terms.

Even though there are differences among methods in the  $p$  azimuthal distribution, some features are common to all our image reconstructions. The peak in the polarization brightness is located near the southwest on 2017 April 5 (at a position angle of  $199^\circ \pm 11^\circ$ , averaged among all methods) and close to the west on 2017 April 11 (position angle of  $244^\circ \pm 10^\circ$ ). That is, the polarization peak appears to rotate counter-clockwise between the two observing days (see the dotted lines in Figure 8). On both days, the region of high polarization brightness is relatively wide, covering a large fraction of the southern portion of the image (position angles from around  $100^\circ$ – $300^\circ$ ).

In the azimuthal distribution of  $\langle \chi \rangle$ , all methods produce very similar values in the part of the image with the highest polarized brightness (the southwest region, between position angles of  $180^\circ$  and  $270^\circ$ ). The EVPA varies almost linearly, from around  $\langle \chi \rangle = -80^\circ$  (in the south) up to around  $\langle \chi \rangle = 30^\circ$  (in the east). The EVPAs on 2017 April 11 are slightly higher

(i.e., rotated counter-clockwise) compared to those on 2017 April 5. This difference is clearly seen for `eht-imaging`, `polsolve`, and `THEMIS`, though the difference is smaller for `DMC` and `LPCAL`. We notice, though, that the differences in the EVPAs between days could also be affected by small shifts in the estimates of the image center on each day. Outside of the region with high polarization, the EVPA distributions for all methods start to depart from each other. There is a hint of a constant EVPA  $\langle \chi \rangle \sim 0^\circ$  in the northern region (i.e., position angles around  $0^\circ$ – $50^\circ$ ) in `polsolve` and `LPCAL` on both days, but the other methods show larger uncertainties in this region.

The discrepancies in EVPA among all methods only appear in the regions with low brightness (i.e., around the northern part of the ring). Therefore, polarization quantities defined from intensity-weighted image averages, discussed in the next sections, will be dominated by the regions with higher brightness, for which all methods produce similar results. Image-averaged quantities are somewhat more robust to differences in the calibration and image reconstruction algorithms, though they are not immune to systematic errors.

### 5.3. Image-averaged Quantities

In comparing polarimetric images of M87, we are most interested in identifying acceptable ranges of three image-averaged parameters that are used to distinguish between different accretion models in Paper VIII: the net linear polarization fraction of the image  $|m|_{\text{net}}$ , the average polarization fraction in the resolved image at  $20 \mu\text{as}$  resolution  $\langle |m| \rangle$ , and the  $m = 2$  coefficient of the azimuthal mode decomposition



## First M87 Event Horizon Telescope Results. VIII. Magnetic Field Structure near The Event Horizon

The Event Horizon Telescope Collaboration  
(See the end matter for the full list of authors.)

Received 2020 December 2; revised 2021 February 3; accepted 2021 February 8; published 2021 March 24

### Abstract

Event Horizon Telescope (EHT) observations at 230 GHz have now imaged polarized emission around the supermassive black hole in M87 on event-horizon scales. This polarized synchrotron radiation probes the structure of magnetic fields and the plasma properties near the black hole. Here we compare the resolved polarization structure observed by the EHT, along with simultaneous unresolved observations with the Atacama Large Millimeter/submillimeter Array, to expectations from theoretical models. The low fractional linear polarization in the resolved image suggests that the polarization is scrambled on scales smaller than the EHT beam, which we attribute to Faraday rotation internal to the emission region. We estimate the average density  $n_e \sim 10^{4-5} \text{ cm}^{-3}$ , magnetic field strength  $B \sim 1\text{--}30 \text{ G}$ , and electron temperature  $T_e \sim (1\text{--}12) \times 10^{10} \text{ K}$  of the radiating plasma in a simple one-zone emission model. We show that the net azimuthal linear polarization pattern may result from organized, poloidal magnetic fields in the emission region. In a quantitative comparison with a large library of simulated polarimetric images from general relativistic magnetohydrodynamic (GRMHD) simulations, we identify a subset of physical models that can explain critical features of the polarimetric EHT observations while producing a relativistic jet of sufficient power. The consistent GRMHD models are all of magnetically arrested accretion disks, where near-horizon magnetic fields are dynamically important. We use the models to infer a mass accretion rate onto the black hole in M87 of  $(3\text{--}20) \times 10^{-4} M_\odot \text{ yr}^{-1}$ .

*Unified Astronomy Thesaurus concepts:* Accretion (14); Black holes (162); Event horizons (479); Jets (870); Kerr black holes (886); Magnetic fields (994); Magnetohydrodynamics (1964); Plasma astrophysics (1261); Polarimetry (1278); Radiative transfer (1335); Radio jets (1347); Relativistic jets (1390)

### 1. Introduction

The Event Horizon Telescope (EHT) Collaboration has recently published total intensity images of event-horizon-scale emission around the supermassive black hole in the core of the M87 galaxy (M87\*; Event Horizon Telescope Collaboration et al. 2019a, 2019b, 2019c, 2019d, hereafter EHTC I, EHTC II, EHTC III, EHTC IV). The data reveal a  $42 \pm 3 \mu\text{s}$  diameter ring-like structure that is broadly consistent with the shadow of a black hole as predicted by Einstein’s Theory of General Relativity (Event Horizon Telescope Collaboration et al. 2019e, 2019f; hereafter EHTC V, EHTC VI). The brightness temperature of the ring at 230 GHz ( $\gtrsim 10^{10} \text{ K}$ ) is naturally explained by synchrotron emission from relativistic electrons gyrating around magnetic field lines. The ring brightness asymmetry results from light bending and Doppler beaming due to relativistic rotation of the matter around the black hole.

M87\* is best known for launching a kpc-scale FR-I type relativistic jet, whose kinetic power is estimated to be  $\sim 10^{42-44} \text{ erg s}^{-1}$  (e.g., Stawarz et al. 2006; de Gasperin et al. 2012). The structure of the relativistic jet has been resolved and

studied at radio to X-ray wavelengths (e.g., Di Matteo et al. 2003; Harris et al. 2009; Kim et al. 2018; Walker et al. 2018).

The published EHT image of M87\* together with multi-wavelength observations are consistent with the picture that the supermassive black hole in M87 is surrounded by a relativistically hot, magnetized plasma (Rees et al. 1982; Narayan & Yi 1995; Narayan et al. 1995; Yuan & Narayan 2014; Reynolds et al. 1996; Yuan et al. 2002; Di Matteo et al. 2003). However, it is not clear whether the compact ring emission is produced by plasma that is inflowing (in a thick accretion flow), outflowing (at the jet base or in a wind), or both. Furthermore, the total intensity EHT observations also could not constrain the structure of magnetic fields in the observed emission region. In order to find out which physical scenario is realized in M87\*, additional information is necessary.

Event Horizon Telescope Collaboration et al. (2021, hereafter EHTC VII) reports new results from the polarimetric EHT 2017 observations of M87\*. The polarimetric images of M87\* are reproduced in Figure 1. These images reveal that a significant fraction of the ring emission is linearly polarized, as expected for synchrotron radiation. The EHT polarimetric measurements are consistent with unresolved observations of the radio core at the same frequency with the Submillimeter Array (SMA; Kuo et al. 2014) and the Atacama Large Millimeter/submillimeter Array (ALMA; Goddi et al. 2021). They also provide a detailed view of the polarized emission region on event-horizon scales near the black hole. Polarized synchrotron radiation traces the underlying magnetic field

<sup>126</sup> NASA Hubble Fellowship Program, Einstein Fellow.

<sup>127</sup> EACOA Fellow.

<sup>128</sup> UKRI Stephen Hawking Fellow.

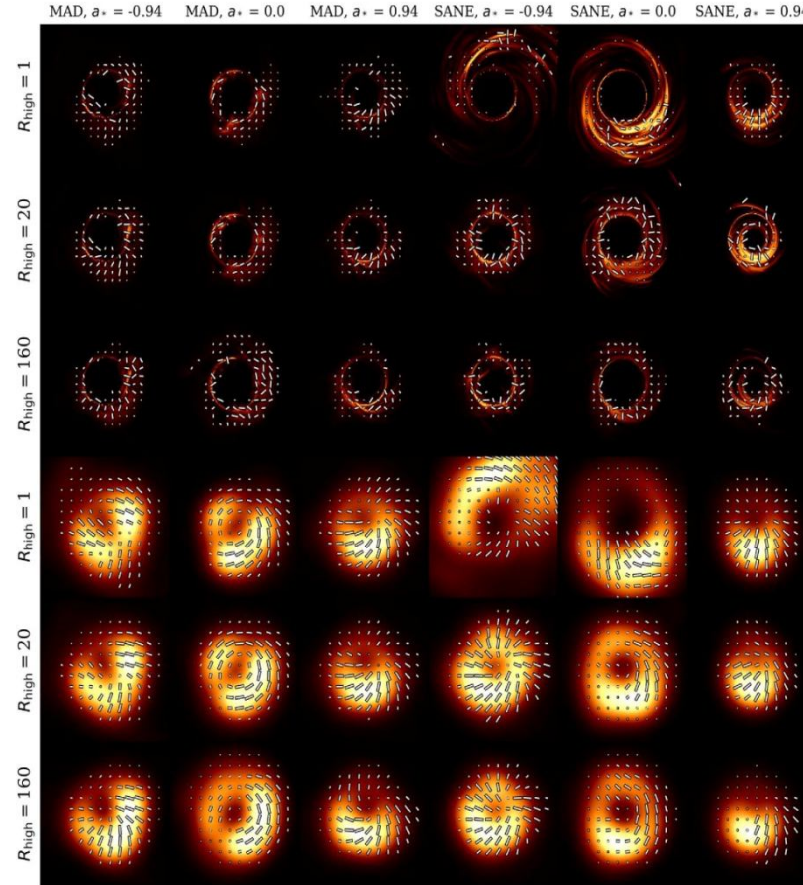


**Figure 4.** Sample snapshot false-color images and polarization maps for a subset of the models in the EHT M87\* simulation image library at their native resolution (top three rows) and blurred with a  $20 \mu\text{s}$  circular Gaussian beam (bottom three rows). The inclination angle for all images is either  $17 \text{ deg}$  (for negative  $a_*$  models) or  $163 \text{ deg}$  (for positive  $a_*$  model), with the black hole spin vector pointing to the left and away from the observer. The tick length is proportional to the polarized flux, saturated at 0.5 of the maximum value in each panel. Here models with  $R_{\text{low}} = 1$  are shown. In general, the EVPA pattern is predominantly azimuthal for MAD models (e.g., MAD  $a_* = 0$   $R_{\text{high}} = 1$ ) and radial for SANE models (e.g., SANE  $a_* = 0.94$   $R_{\text{high}} = 1$ ), although the SANE  $a_* = 0$  models in particular are exceptions to this trend. All models show scrambling in the polarization structure on small scales from internal Faraday rotation, with more pronounced scrambling in models with cooler electrons (larger  $R_{\text{high}}$  parameter).

Figure 7 (right panel) shows the resolved average polarization fraction  $\langle |m| \rangle$  as a function of their image-averaged Faraday rotation depth,  $\langle \tau_{\rho_e} \rangle$ . At small  $\langle \tau_{\rho_e} \rangle$ , the average polarization fraction is  $\langle |m| \rangle \simeq 20\% - 50\%$ . Intrinsic disorder in the magnetic field structure due to turbulence is generally insufficient to produce the low observed image-average polarization fraction in EHT 2017 M87\* data ( $5.7\% \leq \langle |m| \rangle \leq 10.7\%$ ). This is especially evident for the SANE models with

prograde black hole spin, which have the highest resolved polarization fractions. At large  $\langle \tau_{\rho_e} \rangle$ , strong scrambling from internal Faraday rotation typically results in small predicted polarization fractions of  $< 5\%$  at the scale of the EHT beam.

The clear exceptions to this trend are some SANE retrograde models ( $a_* = -0.9375$  for large  $R_{\text{high}}$ ), which show  $\langle |m| \rangle \simeq 10\% - 20\%$  despite their large  $\langle \tau_{\rho_e} \rangle \gtrsim 10^3$ . In these models, most of the observed polarized flux originates in the forward

# Sgr A\* & Shadow

- Another primary EHT source, Sgr A\*, has a precisely measured mass three orders of magnitude smaller than that of M87\*, with dynamical timescales of minutes instead of days. Observing the shadow of Sgr A\* will require accounting for this variability and mitigation of scattering effects caused by the interstellar medium (Johnson 2016; Lu et al. 2016; Bouman et al. 2018).

# • **Conclusions**

- GR predicted a structure of darkness, while in observations one sees a distribution of brightness.
- EHT team showed that shapes and sizes of shadow weakly depend on assumptions about accretion flows.
- AZ (2004-2019): VLBI systems in mm and sub-mm bands could detect mirages (“faces”) around supermassive black holes (for BH@ M87 and BH@GC in particular).
- VLBI systems in mm band detected a shadow around supermassive black hole for BH@ M87 .
- Shapes of images give an important information about BH parameters (including their charge).
- A significant tidal charge of the BH at GC is excluded by observations.
- We hope the EHT team will release a new image of the SMBH@GC shortly at 1.3 mm wavelength shortly.

- Thanks for your kind attention!
-